Fall 2015

Analytical and numerical studies of photo-injected charge transport in molecularly-doped polymers

Amrita Roy Chowdhury

Department: Physics

ANALYTICAL AND NUMERICAL STUDIES OF PHOTO-INJECTED CHARGE TRANSPORT IN MOLECULARLY-DOPED POLYMERS

by

AMRITA ROY CHOWDHURY

A DISSERTATION

Presented to the Faculty of the Graduate School of the

MISSOURI UNIVERSITY OF SCIENCE AND TECHNOLOGY

in Partial Fulfillment of the Requirements for the Degree

DOCTOR OF PHILOSOPHY

in

PHYSICS

2015

Dr. Paul E. Parris, Advisor
Dr. Jerry L. Peacher
Dr. Oran A. Pringle
Dr. Julia E. Medvedeva
Dr. David H. Dunlap

ABSTRACT

The mobility of photo-injected charge carriers in molecularly-doped polymers (MDPs) exhibits a commonly observed, and nearly universal Poole-Frenkel field dependence, $\mu \sim \exp\sqrt{\beta_0 E}$, that has been shown to arise from the correlated Gaussian energy distribution of transport sites encountered by charges undergoing hopping transport through the material. Analytical and numerical studies of photo-injected charge transport in these materials are presented here with an attempt to understand how specific features of the various models developed to describe these systems depend on the microscopic parameters that define them. Specifically, previously published time-of-flight mobility data for the molecularly doped polymer 30% DEH:PC (polycarbonate doped with 30 wt.% aromatic hydrazone DEH) is compared with direct analytical and numerical predictions of five disorder-based models, the Gaussian disorder model (GDM) of Bässler, and four correlated disorder models introduced by Novikov, et al., and by Parris, et al. In these numerical studies, disorder parameters describing each model were varied from reasonable starting conditions, in order to give the best overall fit. The uncorrelated GDM describes the Poole-Frenkel field dependence of the mobility only at very high fields, but fails for fields lower than about 64 V/μm. The correlated disorder models with small amounts of geometrical disorder do a good over-all job of reproducing a robust Poole-Frenkel field dependence, with correlated disorder theories that employ polaron transition rates showing qualitatively better agreement with experiment than those that employ Miller-Abrahams rates. In a separate study, the heuristic treatment of spatial or geometric disorder incorporated in existing theories is critiqued, and a randomly-diluted lattice gas model is developed to describe the spatial disorder of the transport sites in a more realistic way.

ACKNOWLEDGEMENTS

I would like to express my sincere gratitude to those people who helped and accompanied me on this journey of my life up till now.

First and foremost, I am grateful to my advisor Dr. Paul Parris for his guidance, support, kind advice, and encouragement throughout the project. I am really thankful to him for his intense enthusiasm for physics and personal generosity, that helped me for completing my graduate studies successfully.

I owe a debt of gratitude to Dr. Jerry Peacher, Dr. Oran Pringle, Dr. Julia Medvedeva and Dr. David Dunlap, my committee members, for their cooperation and for their valuable time allocation for my work.

I would like to thank Dr. George Waddill and Dr. Jerry Peacher especially for their enormous support to overcome hard times during graduate studies and providing me with a successful teaching assistantship during this time.

I am indebted to my father Mr. Anil Kumar Roy and my mother Mrs. Sumita (Uma) Roy for dedicating their whole lives for the benefit of my success till date. I would love to acknowledge my elder sister Ms. Arpita Roy for her intense love and support in every step of my life. My family will always be close to my heart even though we are often physically separated by great distances.

I owe a debt of gratitude to my loving, encouraging, and hard-working Husband Dr. Uttam Chowdhury who helped me to complete the graduate coursework and supported me to overcome the hard life during my graduate studies.

Last, but not the least I would like to thank all my friends and colleagues for their love and support, which have made the days here happy and enjoyable.

TABLE OF CONTENTS

LIST OF ILLUSTRATIONS

LIST OF TABLES

1. INTRODUCTION

Over the last three decades, there have been numerous experimental [1–9] and theoretical [10–18] studies of the transport of photo-injected charge carriers in the class of amorphous organic materials referred to as molecularly doped polymers (MDPs) [19–23]. Much of the motivation for these studies stems from the practical importance of MDP films, which are used as transport layers in many organic opto-electronic and electrophotographic devices [24, 25], and which are extensively used today as photoreceptors [26–32] and charge transport layers in laser printers and photo-copier machines [23]. The most important advantages that organic materials have in these applications over the amorphous inorganic semiconductors that they have long since replaced, are low production costs, mechanical flexibility, and the low weight of the materials. It is for this reason that they have played an increasingly consequential role in the advancement of many new technological devices [33–43], including organic photovoltaics [24, 44, 45] and organic light emitting diodes.

Molecularly doped polymers are formed by doping organic transport molecules into an insulating polymer matrix [23,46]. An important feature of these materials is that their properties can be systematically varied by changing the molecular structure, e.g., by changing the degree of conjugation in the polymer, or by introducing electronically active substituents. The most commonly used polymers for this purpose are the polycarbonates and polystyrenes, which form linear polymer chains formed from smaller molecular repeat units, called monomers. Thin films of these polymers can be created by evaporation from solution, a process which typically forms an amorphous structurally-disordered material containing many entangled polymer chains of different chain length. To form molecularly doped polymers, organic transport molecules are included in the solution prior to evaporation, and thus end up randomly em-

bedded in the polymer host matrix in concentrations (usually specified as a weight percentage) that can be systematically varied. One of the most commonly studied MDP material is formed by doping diphenylhydrazone (DEH) molecules at 30wt% into polycarbonate, creating the transport material referred to as 30% DEH:PC. The chemical structure of the dopant molecule DEH and the polycarbonate repeat unit are presented in Figure 1.1.

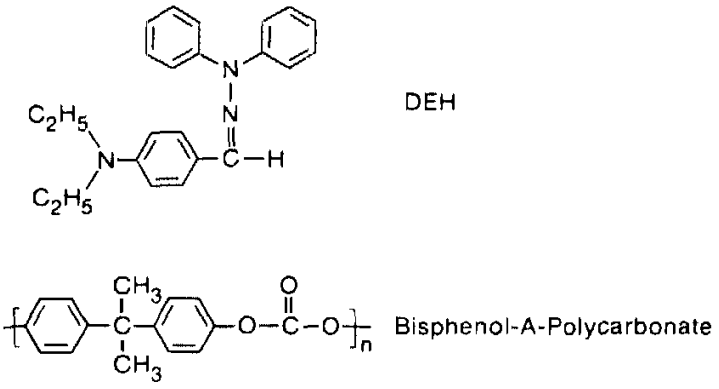

Figure 1.1. The structure of the DEH molecule and polycarbonate.

The dopant molecules in these materials do not directly add carriers to the system, as they would in typical p-type or n-type semiconductors. Indeed, even with significant concentrations of transport molecules molecularly doped polymers remain electrically insulating to very high fields. Rather, these smaller organic molecules are included simply to provide a connected network of *transport sites* for charge carriers *optically or electronically injected* into the materials. Once injected, charge carriers are then able to move between electronic states localized on neighboring transport molecules doped into the polymer host matrix. In these materials then, electron or hole transport occurs by charge transfer between localized states of adjacent donor or acceptor molecules, and occurs via a thermally-assisted hopping mechanism.

In this dissertation several features of charge transport in MDPs are theoretically studied and several new analytical and numerical results are presented. This introductory section of the dissertation provides a basic description of the underlying physics of photo-injected charge transport in molecularly-doped polymers, emphasizing the important role of *energetic and spatial disorder* in a proper description of the transport process. After a brief review of the electronic structure of MDPs and a discussion of how that structure gives rise to the hopping transport mechanism, an overview is presented of experimental observations that reveal a number of essentially universal features that have been seen in numerous transport studies of many MDP systems. After characterizing those observations, basic theoretical ideas and the theoretical models that have been developed to explain these materials are reviewed. In this review, it is noted that essentially all of the competing models differ from one another simply in the manner in which they incorporate three basic features of the underlying physics. The first of these features involves the way the models incorporate the energetic disorder associated with different hopping sites in the material. The second feature involves the different choices that these models make for the functional form of the microscopic transition rates that govern the hopping of charge carriers between different dopant molecules. Finally, the third way in which competing theoretical models differ is in the manner with which they treat geometrical or spatial disorder associated with the random locations and orientations of dopant molecules embedded in the polymer host.

Following this introductory section, the remaining four sections of the dissertation present a series of analytical and numerical calculations that are intended to compare and contrast predictions obtained by incorporating these different features, in an attempt to determine which of the various choices, for each of the features identified above, gives the best actual agreement with transport measurements on

the commonly-studied molecularly-doped polymer described above and depicted in Figure 1.1, namely, 30% DEH:PC.

1.1. ELECTRONIC STRUCTURE AND CHARGE TRANSPORT IN MOLECULARLY-DOPED POLYMERS

An extensive scientific literature exists in which different kinds of transport are studied, often using similar theoretical techniques, for a large variety of different condensed matter systems. In this large body of work, one finds theoretical descriptions of the transport of material particles, such as individual electrons and holes (as in MDPs), Cooper pairs, ionized atoms, impurities, and molecules. But it also includes studies of the transport of other physical quantities, such as spin, energy, momentum, etc. Quantized vibrational energy or the momentum transfer that accompanies it is described in terms of phonons, vibrons, or librons. Electronic energy transfer, in which no material particle actually moves, is described through the quasi-particle concept of excitons. These include the Wannier-Mott exciton, which has a large radius and extends over many lattice spacings, and the Frenkel exciton which is confined to a single molecule, and which is a commonly observed quasi-particle excitation of organic molecular solids [47, 48].

The transport of charge carriers, such as electrons in metals and other types of ordered solids (i.e., crystals) was first qualitatively explained in a simple model proposed by Drude in 1900 [49]. In the Drude model it was assumed that thermal electrons scatter off of the metal ions, and collisions between electrons are neglected. A quantitatively correct description of real materials remained unavailable, however, until the development of quantum theory, which described the behavior of ordered metals and semi-conductors (and the lack of transport through crystalline insulators) through the use of band theory. In the current picture, electrons in an ordered lattice move through the system in extended Bloch states whose energies form energy bands, and the electrons scatter, not off the ordered array of ions itself, but off of deviations

that occur, due to the presence of defects, impurities, and lattice vibrations, in the otherwise ordered structure of the crystal [48].

Unlike ordered crystalline materials, amorphous organic materials like MDPs do not have a well-defined translational symmetry, and, due to this lack of structure, the electronic coupling of charge carriers to the softer vibrational modes of typical organic materials becomes stronger than it would be in ordered inorganic materials. Both of these factors help to create localized, rather than extended states, and so charge carriers in these materials tend to travel by a hopping mechanism between localized electronic states on different molecules, instead of moving through states like free particles [23, 46].

Electronic states of MDPs are, therefore, to a good approximation, localized on the polymer or dopant molecules, and the low-lying molecular orbitals of each molecule are filled up to an energy level referred to as the highest occupied molecular orbital (or HOMO), which is separated by a significant energy from the states associated with lowest unoccupied molecular orbital (or LUMO). The localized HOMO and LUMO levels are randomly distributed throughout the material, and have different energy levels due to the interaction of each molecule with its particular random environment. The energy levels for both host and dopant molecules in MDPs are schematically depicted in Figure 1.2.

Thus, in the pure amorphous polymer film, the energy difference $\Delta_0 >> kT$ between the polymer HOMO and LUMO levels is sufficiently large that, at any reasonable temperature, intrinsic transport processes, in which an electron in a HOMO level is thermally promoted to a LUMO level, where it can migrate among the LUMO levels of adjacent molecules, is exponentially unlikely to occur over any time scale of experimental relevance. The filled valence band, the unfilled conduction band, and the large HOMO-LUMO gap thus conspire to make the polymer host strongly insulating.

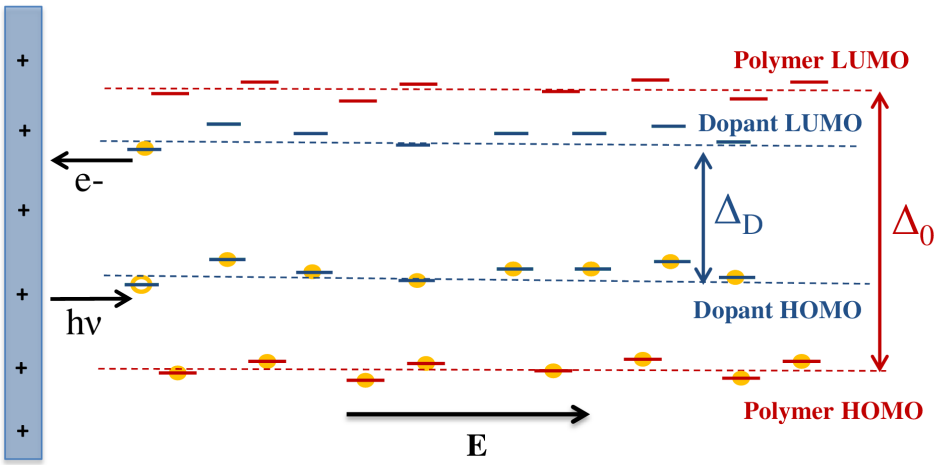

Figure 1.2. Energy structure of molecularly-doped polymer.

The energy difference Δ_D between the HOMO and LUMO levels of dopant molecules incorporated into the polymer is typically smaller than that of the host polymer, but it is still much larger than kT, so that even at significant doping levels, the system remains an excellent insulator.

Charge transport in this system becomes possible when, in the presence of a significant electric field, dopant molecules are excited energetically or optically by an external source. Consider, e.g., a dopant molecule located near a semi-transparent (positively charged) contact, that is photo-excited (e.g. with a laser tuned to a frequency for which $\Delta_0 > \hbar\omega > \Delta_D$) creating a Frenkel exciton (a particle-hole excitation localized on the dopant molecule), as shown in Figure 1.2. In the presence of a strong electric field, the exciton can undergo field-ionization, so that the photo-excited, field-dissasociated electron, which is attracted to the nearby positive contact, leaves the dopant molecule and neutralizes itself. But of course, this leaves a hole in the HOMO level of the dopant molecule, which can then make hopping transitions into the HOMO levels of other nearby dopant molecules.

The correctness of this picture of a hopping transport mechanism in molecularly doped polymers is confirmed by the well-documented [17, 23] exponentially decreasing dependence of the mobility μ on the mean inter-dopant spacing ρ, which is easily varied experimentally by changing the dopant concentration. This behavior reflects the fact that the hopping rate, i.e., the transition probability per unit time W_{mn} for a transition of the charge carrier from the localized state at site n to a state localized at site m, is exponentially dependent (Figure 1.3) upon the spatial separation $r_{mn} = |\vec{r}_m - \vec{r}_n|$ of the two sites, as a result of the exponential fall-off of the wave-functions of the two localized states involved.

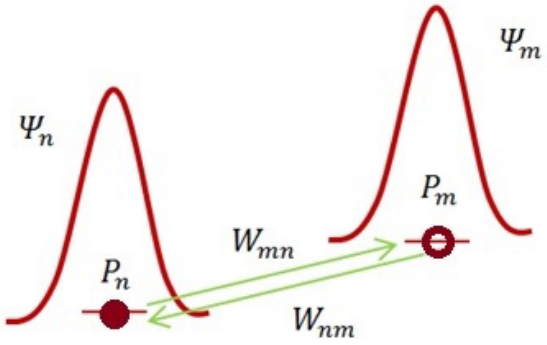

Figure 1.3. Hopping transition between two localized states separated by r_{nm}, with energies ε_n and ε_m .

As mentioned earlier, different dopant molecules have different energy levels due to their interaction with different local environments. Thus, the transition rate is also dependent on the energy difference $\varepsilon_{nm} = \varepsilon_m - \varepsilon_n$ between the two sites. The functional form of the energy dependence depends on the nature and the strength of the electron-phonon coupling, which allows for the absorption or emission of one or more phonons during a transition between states of different energies, so that the total energy of the entire system is conserved. After briefly describing key features of

experimental measurements of photo-injected charge transport in molecularly-doped polymers the different functional forms associated with these transition rates will be discussed, as this constitutes one of the key features that distinguishes the different theoretical models of charge transport in these materials.

1.2. EXPERIMENTAL OVERVIEW

Experimental studies [1–9, 19] of photo-injected charge transport in molecularly doped polymers have focused on determining the injected charge carrier mobility $\mu = v_d/E$, where v_d is the drift velocity that the carrier develops in the presence of an applied electric field E. Although there are a number of different experimental techniques [50] that have been developed to measure the mobility of charge carriers in these materials, by far the most common of these is the time-of-flight (TOF) approach first introduced by Haynes and Shockley [51].

The experimental setup associated with a time-of-flight measurement is schematically illustrated in Figure 1.4. In these experiments, the molecularly doped polymer of interest serves as a dielectric, filling the gap of a parallel plate capacitor, which is formed by depositing on opposite faces of a thin MDP film of thickness $L \sim 10-50\mu$m,

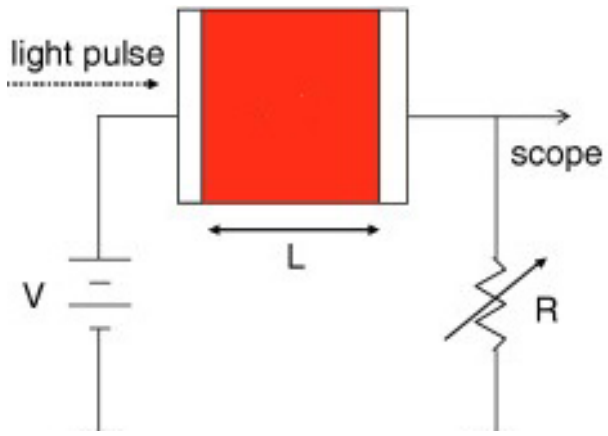

Figure 1.4. Schematical representation of the time-of-flight technique.

semi-transparent electrodes, usually of gold or aluminum. The MDP filled capacitor then forms an element of an RC circuit in which, in the fully charged configuration, a large potential bias V imposed across the capacitor generates a large static electric field $E = V/L$ inside the MDP transport layer. Using a laser pulse, centered at a frequency that is strongly absorbed by the MDP material, a sheet of charge carriers is then photo-injected in the immediate neighborhood of the positively charged contact, as described earlier. The transient drift current that subsequently flows through the sample, which is proportional to the instantaneous drift velocity and to the number of charge carriers in the sample, can be monitored by measuring the voltage across the external resistor. When charge carriers begin to reach the collecting electrode, the drift current starts to decrease, and a knee develops in the photo-current transient. If all the charge carriers in the sample moved at the same time with the same constant drift velocity v_d, the TOF current transient would look like the black dashed line as seen in Figure 1.5.

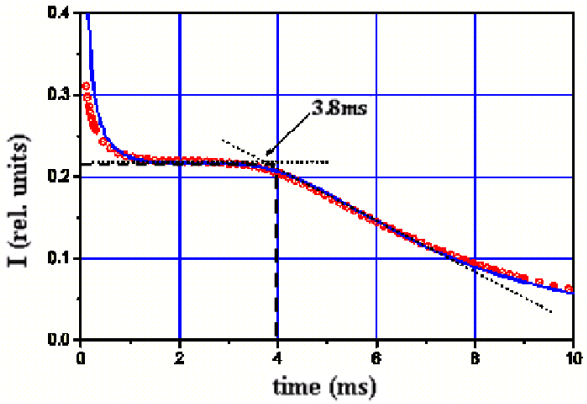

Figure 1.5. Idealized (dashed black line) and actual (blue line) TOF photo-current transient.

But this idealized picture is unrealistic because it fails to take into account the fact that the carrier packet spreads during its traversal of the film as a result

of diffusion, and because carriers move through different local environments with different drift velocities. Thus there is a distribution of arrival times, which rounds the sharp edge, as depicted by the blue line in Figure 1.5. Nonetheless, the mean travel time τ, identified with the location of the knee in the photo-current transient, is easily obtained, and can then be used to determine the drift velocity $v_d = L/\tau$ and thus the mobility

$$\mu = \frac{L^2}{V\tau}.$$

Numerous time of flight measurements on a large class of different molecularly doped polymers reveal a number of universal features associated with charge transport in these materials. The two universal features that form the focus of the theoretical studies presented in later sections of this dissertation are the temperature and electric field dependence of the time-of-flight mobility, which has been shown to be strongly activated with both temperature and electric field. The hopping mobility has an electric field dependence that follows a nearly universal Poole-Frenkel-like relation [52]

$$\mu \propto \exp\left(\beta\sqrt{E}\right) \tag{1}$$

over a wide range of (large) applied fields ($E \sim 10^4 - 10^6$) V/cm at fixed temperatures. Figure 1.6 shows experimental data for 30% DEH:PC at several different temperatures, as indicated, taken from the work of Mack, et al. [19]. These data, which lie on straight lines in this logarithmic plot of the mobility as a function of the square root of the electric field, clearly demonstrate a $\log(\mu) \propto E^{1/2}$ relation equivalent to (1).

The data taken at different temperatures also clearly demonstrate that the mobility in this material dramatically increases with temperature. At fixed electric field, the temperature dependence of the mobility has been characterized as having

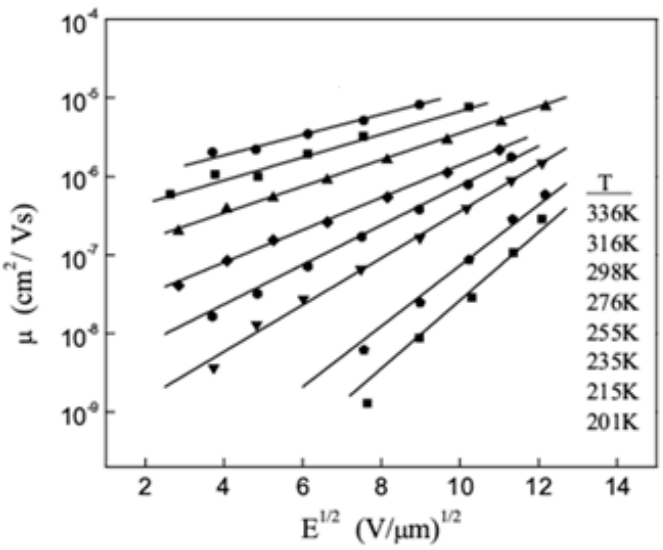

Figure 1.6. Mobility *vs.* Field for 30% DEH:PC.

either a linearly activated form

$$\mu \propto \exp\left[-\left(T_0/T\right)\right]$$

referred to as Arrhenius-like behavior, or a quadratically activated form, represented by the expression

$$\mu \propto \exp\left[-\left(T_0/T\right)^2\right]$$

Figure 1.7 shows a logarithmic plot of mobility data for PVK-TNF taken by Pfister [53], as a function of the inverse temperature (in the left panel), and as a function of the square of the inverse temperature (in the right panel). Although the quadratically activated version is more convincing, the fact that the data points in either of these two plots fail to lie exactly on straight lines, suggests either that it is activated with

some intermediate power of the inverse temperature, or that it has both linearly and quadratically activated components.

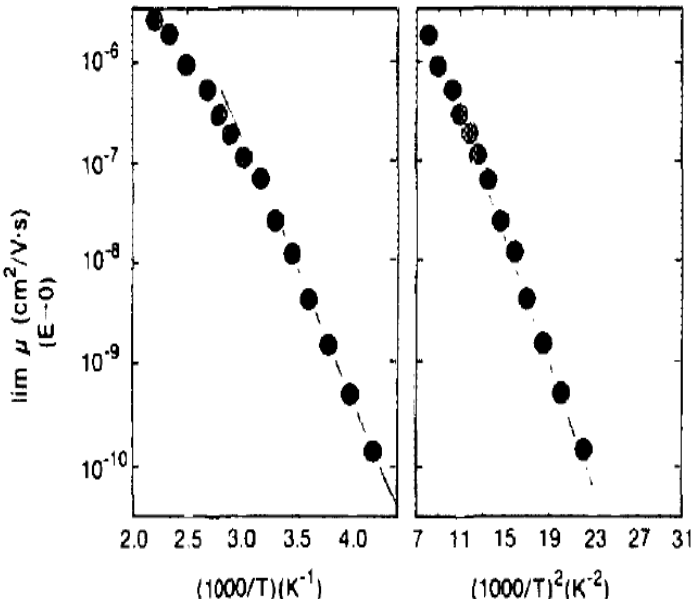

Figure 1.7. Arrhenius and non-Arrhenius type temperature dependence plots for PVK-TNF.

1.3. THEORETICAL MODELS DEVELOPED TO EXPLAIN EXPERIMENTAL OBSERVATIONS

A number of theoretical models have been proposed to explain the electric field and temperature dependence of the time-of-flight mobility measured in molecularly doped polymers. These models share some common features, but differ from one another in several important aspects.

In all of the theoretical models discussed in the work presented later in the dissertation, the moleculary doped polymer is treated as a more or less uniform spatial distribution of transport sites in number density $\rho = N/V$ determined by the experimental concentration. Each transport site n is associated with random site

energy ε_n, which determines the energy of a carrier when it is located at that site, and which is determined by an underlying probability distribution. In all cases, the marginal single site distribution $P(\varepsilon_n)$ function is the same for each site. For each pair of sites n and m in the system, there is a transition rate $W_{m,n}$ that determines the probability per unit time for a hopping transition to occur from site n to site m, for a particle initially located at site n. This transition rate is a function of the temperature, the electric field, the site energy difference $\varepsilon_{mn} = \varepsilon_m - \varepsilon_n$ and the displacement $\vec{r}_{mn} = \vec{r}_m - \vec{r}_n$ associated with the transition, which determines the field dependence in the way it modifies the site energies, i.e., $\varepsilon_m \rightarrow \varepsilon_m - e\vec{E}\cdot\vec{r}_m$, and which appears in the exponential decay

$$W_{mn} \propto \exp\left(-2\gamma r_{mn}\right)$$

with the distance r_{mn} between sites as a result of wave function overlap. In each model, the effect of spatial fluctuations can be treated through a modification of this exponential dependence, either due to actual fluctuations in inter-site distances, or through random variables that mimic this effect.

The various different theoretical models proposed to explain the temperature and field dependence *differ* from one another in the specific manner in which they implement these common features. As suggested earlier, the main differences between them involve (1) the nature of the underlying site energy distribution function, (2) the specific functional form of the transition rates W_{mn} on energy and (3) the manner in which spatial or geometric disorder is implemented.

The main differences associated with the underlying distribution of site energies involves the issue of *spatial correlations* in the random energy landscape through which the charge carriers move.

The earliest hopping model, the Gaussian disorder model, or GDM, introduced by Bässler and coworkers [17, 23] treats the MDP as an ordered cubic lattice of transport sites with a lattice spacing a equal to the average nearest neighbor distance of dopant molecules in the medium, and having random site energies ε_n *independently* drawn from an uncorrelated Gaussian distribution

$$P\left(\varepsilon_n\right) = \frac{\exp\left(-\varepsilon_n^2/2\sigma^2\right)}{\sqrt{2\pi\sigma^2}} \tag{2}$$

of energetic width σ. This distribution of site energies is assumed to arise from the interaction

$$\varepsilon_n = \sum_i \vec{p}_i \cdot \vec{E}_n = \sum_i \frac{e}{4\pi\varepsilon_0 r_i^2} \hat{r_i} \cdot \vec{p}_i \tag{3}$$

of charge carriers with the (unscreened) randomly oriented and randomly distributed dipole moments $\vec{p}_i$ of the polymer and dopant molecules in the medium. Due to the long-range nature of this interaction, the site energy is a sum of many random terms, and studies of this kind of dipolar disorder confirm that this produces a distribution of site energies that is approximately Gaussian [17]. Additional experiments on different materials confirm a correlation between the width σ of the site energy distribution function inferred from experiment, and the magnitude of the dipole moments of molecular constituents [23].

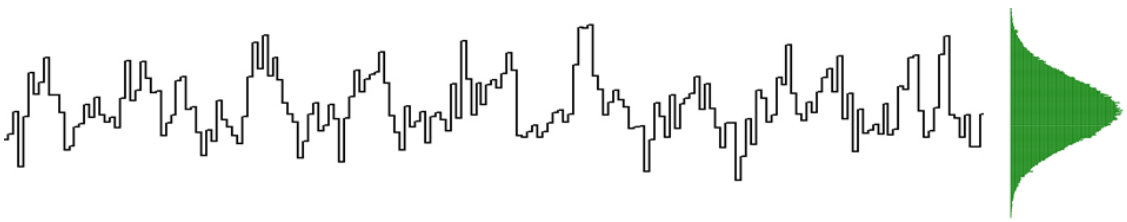

Figure 1.8. Gaussian density of transport site energies.

But later theoretical studies on this kind of dipolar disorder also revealed that the long range nature of the charge-dipole interactions leads to an energetic landscape that has strong *spatial correlations*, described by a site energy auto-correlation function [18, 54]

$$C_{nm} = \langle \varepsilon_n \varepsilon_m \rangle \sim \sigma^2 \frac{a_0}{r_{nm}} \tag{4}$$

that falls of very slowly, as the inverse first power of the distance between the sites. In this expression a_0 represents the closest distance of approach of two dopant molecules in the system. Thus, in this kind of spatially correlated potential energy landscape, the site energy difference between two dopant molecules is *not independent* of their spatial separation. With enhanced probability it is smaller if they are closer together than if they are far apart. As a result, deep energetic fluctuation cannot occur over short length scales. Indeed, there is a characteristic length scale over which potential energy fluctuations of a given magnitude need to develop. A graphical representation of the difference between a correlated and uncorrelated potential energy landscape is given in Figure 1.9.

These considerations led to the development of a number of *correlated disorder models*, (CDMs) [10–12, 16, 18, 54, 55] In these models, the site energies are not independent random variables, and have to be defined by a joint probability distribution function $P(\{\varepsilon_n\})$ that in principle depends on all of the site energies in the system. Thus, it actually gives a probability for a particular random energy landscape to occur. If $\vec{\varepsilon}$ denotes a vector with components ε_n, and Ω a matrix which is the inverse of the covariance matrix (4), this joint probability distribution can be written for Gaussian disorder in the form

$$P(\vec{\varepsilon}) = \frac{1}{\sqrt{(2\pi)^N \left|\Omega^{-1}\right|}} \exp\left(-\frac{1}{2}\vec{\varepsilon} \cdot \Omega \cdot \vec{\varepsilon}\right). \tag{5}$$

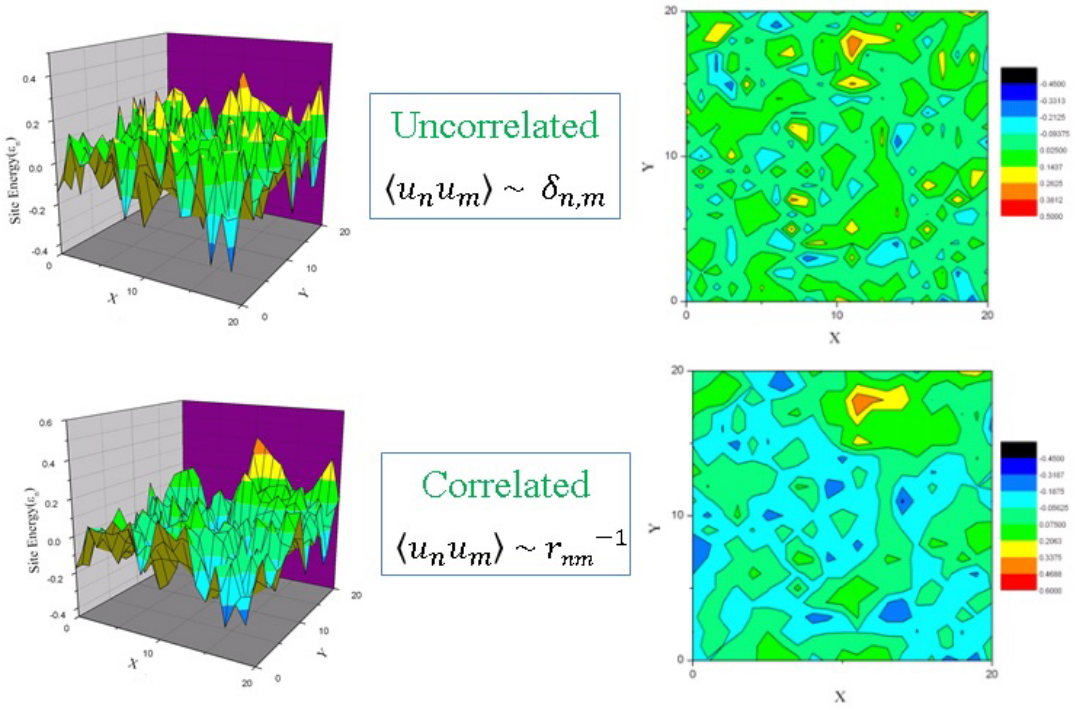

Figure 1.9. Uncorrelated and correlated Gaussian density of transport site energies.

Thus a key difference between proposed theoretical models is whether or not, or even how, spatial correlations are incorporated into the potential energy landscape.

A second main difference between the different models proposed to model charge transport in molecularly doped polymers is in the functional form of the transition rates W_{mn} that are used in transport calculations and simulations.

In the original uncorrelated Gaussian disorder model [17, 23], it was assumed that the disordered polymer has a broad spectrum of vibrational modes, so that there is always the possibility of absorbing or emitting a single phonon having the required energy $|\varepsilon_{mn}| \sim \hbar\omega_i$ needed for the transition. Hence, the hopping rate in the absence of applied electric field, between two sites can be expressed in the so-called

Miller-Abrahams [56] form

$$W_{mn} = \begin{cases} \nu_0 \exp(-2\gamma r_{mn}) \exp\left(-\varepsilon_{mn}/kT\right), & \varepsilon_{mn} > 0 \\ \nu_0 \exp(-2\gamma r_{mn}), & \varepsilon_{mn} < 0. \end{cases} \tag{6}$$

where ν_0 is a (constant) attempt frequency and γ is the wave-function overlap parameter. With this form of the transition rate, hops down in energy are independent of the temperature and the energy difference between sites, while hops up in energy are thermally suppressed by a Boltzmann factor $\exp\left[-\left(\varepsilon_{nm}\right)/k_B T\right]$. Like all transition rates, in the absence of an electric field, the system has to be able to approach thermal equilibrium. As a result, transition rates for forward and backward hops between any pair of sites in the system have to obey a detailed balance condition [57],

$$\frac{W_{nm}}{W_{mn}} = \frac{P_n}{P_m} = \exp\left(-\frac{\varepsilon_n - \varepsilon_m}{k_B T}\right)$$

in which P_n is the equilibrium probability of a carrier to be at site n at temperature T. This condition essentially states that in equilibrium, the number of transitions per unit time in one direction has to balance the number of transitions per unit time in the opposite direction.

The strong interaction between charge carriers and the vibrational modes of the molecular medium have led some workers to suggest that one-phonon thermally assisted rates of the Miller-Abrahams [56] form are inappropriate [55]. Indeed, electronic structure calculations show significant reorganization energy differences [46, 58, 59] between the ionized and neutral dopant molecule, which implies a molecular distortion that cannot be described by a one phonon process. Thus, some of the theories that have been developed assume that electron-phonon interactions make the charge carriers *polaronic*, i.e., that the carriers are accompanied by a local distortion of the medium and/or of the molecule on which it resides. The elastic energy associated with

this distortion partially contributes to the activation energy associated with hopping transitions. Thus, in polaronic models, the hopping rate between two sites separated in energy by an amount ε_{mn} is assumed to take a form

$$W_{mn} = \frac{J_0^2 e^{-2\gamma r_{mn}}}{\sqrt{2\hbar^2 E_B kT/\pi}} \exp\left[-\frac{E_B + \varepsilon_{mn}}{2kT} - \frac{\varepsilon_{mn}^2}{8E_B kT}\right], \tag{7}$$

that follows from the theory of the non-adiabatic small polaron [60, 61]. In this expression, $J_0 e^{-\gamma r}$ is the overlap integral for two sites separated by a distance r, the parameter γ again describes the exponential decay of the transition strength with increasing inter-site separation, and E_B is the polaron binding energy, a measure of the polaronic lowering of the carrier's energy due to relaxation of the molecular medium. This functional form for the transition rate is essentially the same as that which follows from Marcus's theory for the rate of electron transfer reactions [62], and is sometimes referred to as a "Marcus rate".

Thus another key difference between proposed theoretical models is whether they assume one-phonon thermally assisted rates of the Miller-Abrahams form (6), or polaronic rates, as described by (7).

Finally, the theoretical models that have been developed can differ from one another in the manner and the degree to which they incorporate the effects of spatial or geometrical disorder.

In the original Gaussian disorder model [17], and in many of the subsequent theoretical models developed later, transport sites are arranged on the sites of a filled cubic lattice, with a lattice spacing equivalent to the mean nearest-neighbor distance in the amorphous polymer. To treat the effects of spatial disorder arising from random molecular orientations and actual fluctuations in inter-site distances, the Gaussian disorder model allows for a modification of the exponential factors appearing in (6)

to a form

$$W_{n,m} = \begin{cases} \nu_0 e^{-2\gamma r_{nm}} \exp(-\Gamma_{nm} r_{nm}/a) \exp\left(-\varepsilon_{nm}/k_B T\right), & \varepsilon_{nm} > 0 \\ \nu_0 e^{-2\gamma r_{nm}} \exp(-\Gamma_{nm} r_{nm}/a), & \varepsilon_{nm} < 0. \end{cases} \tag{8}$$

in which $\Gamma_{nm} = \Gamma_n + \Gamma_m$ is the sum of independent random variables Γ_n distributed according to a common Gaussian distribution

$$P\left(\Gamma_n\right) = \frac{\exp\left(-\Gamma_n^2/\Sigma^2\right)}{\sqrt{\pi\Sigma^2}}$$

of zero mean and statistical width $\langle \delta\Gamma_n \rangle = \dfrac{\Sigma}{\sqrt{2}}$. The strength of the geometrical disorder in the GDM is traditionally characterized by the parameter $\Sigma = \sqrt{2}\langle \delta\Gamma_n \rangle = \langle \delta\Gamma_{nm} \rangle$. As suggested in Figure 1.10 this heuristic treatment is intended to mimic Gaussian fluctuations in inter-site distances.

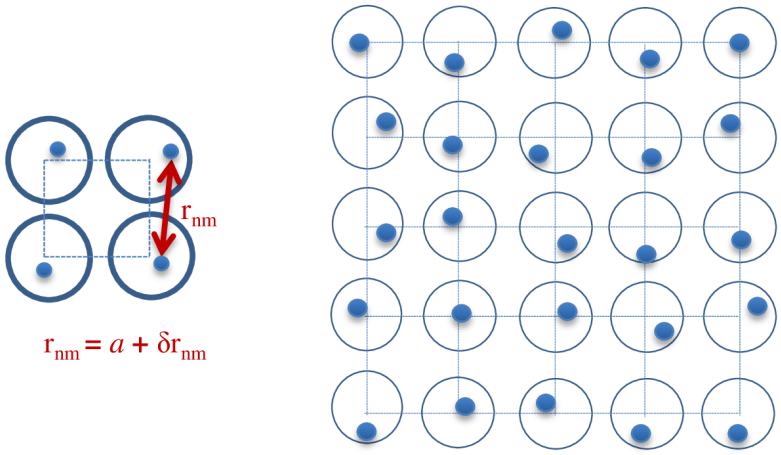

Figure 1.10. Gaussian distribution of geometrical disorder.

In reality, of course, dopant molecules are randomly distributed throughout a moleculary doped polymer, and fluctuations in nearest neighbor distances are not accurately described by a Gaussian distribution. As a consequence, a more realistic treatment of spatial disorder has been proposed that preserves the numerical advantages of working on a lattice, by treating the spatial distribution of dopant molecules as a *randomly-diluted lattice gas*.

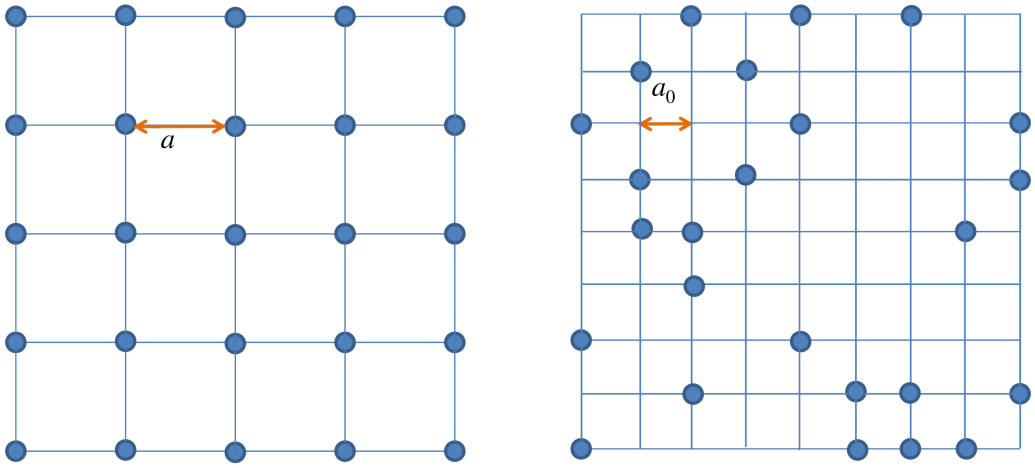

Figure 1.11. Distribution of transport sites on a filled lattice and with a partially filled lattice.

In such a model, the dopant molecules randomly occupy the sites of a cubic lattice in some fractional concentration c, with the lattice spacing adjusted to keep the number density ρ of transport sites constant as before. At $c = 1$, in which 100% of the lattice sites are occupied by transport sites, the system is completely ordered. As c decreases, fluctuations in the nearest-neighbor distances develop, and at very small concentrations, as the mean separation between sites becomes large compared to the lattice spacing, the spatial distribution of sites approaches a completely random spatial distribution. Thus, in this treatment of spatial disorder, the parameter

measuring the strength of the disorder is the quantity $1 - c$, rather than the disorder parameter Σ that appears in the GDM.

Thus, a final key difference in models of charge transport is the manner in which they do (or do not) treat geometrical or spatial disorder.

For a given model, which according to the features enumerated above, defines a specific procedure for (e.g., numerically or virtually) setting up a finite realization of the disordered material, i.e., of assigning site energies, and determining the appropriate transition rates W_{mn} that govern the motion of a particle between the different sites of the virtual sample, transport properties can then obtained in one of two different ways.

Historically the oldest approach taken was to perform Monte Carlo simulations [17], which use the assigned transition rates to generate a statistically correct ensemble of field-biased random walks for carriers moving among the the simulated array of transport sites. By statistical analysis one can then determine the average position of a walker as a function of time, and thus determine the drift velocity and the mobility.

An alternative, but equivalent approach [10], employed in the new work presented here, is to incorporate the transition rates W_{mn}, assigned according to the individual model, into an evolution equation

$$\frac{dP_n}{dt} = \sum_m \left(W_{nm} P_m - W_{mn} P_n \right) \tag{9}$$

for the probabilities $P_n(t)$ of finding a charge carrier at site n at time t. A solution of this equation in steady state allows the steady drift velocity and mobility to be obtained in a straightforward fashion, as described in more detail in later sections of this dissertation.

In the following subsections, the main theoretical models that have been introduced to explain the temperature and field dependence of the charge carrier mobility

in molecularly doped polymers are enumerated. For each model, some background is given regarding its development, and each one is characterized in terms of the way it incorporates the key features mentioned above.

Later sections of this dissertation present new analytical results, and numerical calculations that compare the predictions of these models, to each other, and more importantly, to experimental data obtained for real molecularly doped polymers.

1.3.1. The Gaussian Disorder Model (GDM). The first disorder based model developed to explain charge transport in MDPs was the Gaussian disorder model of Bässler [17]. In this model, transport sites are located on the sites of a filled cubic lattice, with site energies independently drawn from a Gaussian distribution of width σ, as described by Eq.(2), and one-phonon thermally assisted hopping rates are assumed of the Miller-Abrahams form (8), which allows for the inclusion of Gaussian spatial disorder, characterized by a spatial disorder parameter Σ.

In spite of the GDM's enormous footprint in the MDP literature, stemming from its emergence as the first disorder based theory in this field, there appear to be no studies in which a *direct* side-by-side comparison has been made between theoretical predictions of the GDM and experimentally measured mobilities for actual MDPs. Rather, the extensive "comparison" with experimental data often attributed to the GDM has been performed through an *indirect* procedure [23], summarized as follows: first, Monte Carlo simulations of the GDM at one fixed value of $2\gamma a = 10$, one lattice spacing $a = 6$Å, and one temperature $T = 295$K, were performed for different values of σ and Σ. Numerical results for the GDM (some of which are reproduced in Section 3) yield mobilities with a quadratically activated temperature dependence, but with a field dependence that does not agree well with the strictly linear dependence of $\log \mu$ on $\sqrt{E}$ at all fields. Despite this poor agreement of the GDM with the field dependence observed in MDPs, the Monte Carlo results were characterized (or fit)

over a limited range of *large electric fields* by the functional relation

$$\mu = \mu_0 \exp\left[-(A\hat{\sigma})^2\right] \exp(C(\hat{\sigma}^2 - \hat{\Sigma}^2)\sqrt{E}), \tag{10}$$

where $\hat{\sigma} = \sigma/kT$. The results were used to deduce optimal values for the independent constants $A = 0.67 \approx 2/3$ and $C = 2.9 \times 10^{-4}$ $(\mathrm{V/cm})^{-1/2}$. In addition, it was determined that at these high fields, the fitting parameter $\hat{\Sigma}$ is approximately constant ($\hat{\Sigma} = 1.5$) for small values of the geometrical disorder parameter ($\Sigma < 1.5$), and linear $\hat{\Sigma} \sim \Sigma$ for larger values ($\Sigma > 1.5$).

Although Eq. (10) is often purported as representing actual predictions of the GDM, the field dependence exhibited by (10) is *strictly* of the Poole-Frenkel type for all fields, and does not describe the actual field dependence of the GDM, which clearly deviates from a Poole-Frenkel law at low-to-moderate fields.

Nonetheless, as an *empirical formula*, with σ, $\hat{\Sigma}$, and μ_0 treated as empirical parameters unrelated to the GDM, Eq. (10) *can* characterize the behavior of actual MDPs, and has been extensively used in this way to extract empirical values for many different materials [23]. However, a comparison of experimental data with formula (10) is not the same as a direct comparison of that data with the predictions of the GDM itself.

1.3.2. The Correlated Gaussian Disorder Model (CGDM). As mentioned earlier, theoretical attempts to understand the inability of the GDM to produce the robust Poole-Frenkel field dependence observed in real MDPs led to extensive study of so-called *correlated disorder models*. The first Gaussian model to be developed that included the spatial correlations appropriate to the charge-dipole interactions thought to be the main source of energetic disorder in these materials will be referred to here as the correlated Gaussian disorder model (CGDM), although variations of it in the literature are sometimes referred to simply as the correlated

disorder model, or the dipolar glass model [11, 54, 63, 64]. The CGDM differs from the original Gaussian disorder model only in that it incorporates a correlated energy landscape, as described by the joint site energy distribution function (5). The model retains the use of Miller-Abrahams rates (8) employed in the GDM, which therefore allow for the incorporation of Gaussian spatial disorder as described by the GDM spatial disorder parameter Σ.

Analytical calculations [10, 12, 16, 18] in 1D and numerical simulations [10, 11, 55] obtained for the CGDM with $\Sigma = 0$ show that dipole-like spatial correlations can generate a field dependence in agreement with the Poole- Frenkel law over a large range of applied fields, in contrast to the small range of agreement displayed by the GDM. Empirical formulae similar to (10) have been devised [10,11] that, as with the GDM, purport to characterize the CDM, with $\Sigma = 0$, over the (now more extended) regions of the electric field where they actually exhibit Poole-Frenkel behavior, but as with the GDM, there does not appear to be in the MDP literature any instances in which a direct side-by-side comparison has been made between the predictions of the CGDM and actual experimental results for any MDP at all temperatures and electric fields for which data have been taken [63].

1.3.3. Polaron Correlated Disorder Models (PCDM, PCDM-Σ and PCDM-c). In this dissertation, in addition to the GDM and CGDM, two versions of the polaron correlated disorder Model (PCDM) introduced in Ref. [10] were considered. In the PCDM, transport also takes place on a filled cubic lattice with *correlated* Gaussian site energies. The key difference between the CGDM and the PCDM is that the latter incorporates polaronic rates of the form (7), which take account of the molecular reorganization that occurs when a charge carrier occupies a given transport site.

As originally introduced [10], the PCDM did not include any contributions due to geometrical disorder, and it is this version that is denoted by the acronym

PCDM. As with the models described above, direct comparisons of the predictions of the PCDM with experimental data have not appeared in the literature.

At the expense of introducing an additional independent parameter, it is also possible to consider a natural extension of the PCDM that includes geometric disorder in a manner identical to that implemented in the GDM of Bässler, et al. This is done by making, in (7), the substitution

$$\exp(-2\gamma r_{mn}) \rightarrow \exp(-2\gamma r_{mn}) \exp(-\Gamma_{mn} r_{mn}/a),$$

which introduces the same Gaussian disorder parameters $\Gamma_{mn} = \Gamma_m + \Gamma_n$ of zero mean that appear in the GDM. This modification of the PCDM, which is denoted by PCDM-Σ, reduces to the original PCDM as the statistical width Σ of the geometrical disorder parameters Γ_{mn} approaches zero.

A final correlated model considered separately in the final section of this dissertation is a variant of the PCDM in which spatial disorder is incorporated using the diluted lattice gas approach described above. In this model, which incorporates a correlated Gaussian landscape, and polaron rates, there is no Gaussian component of the spatial disorder, i.e., in this model $\Sigma = 0$, but it includes the effects of increasing disorder by randomly diluting the lattice, while keeping the mean inter-particle spacing and the number density of sites fixed. This variant of the PCDM will be referred to as PCDM-c, in which c refers to the concentration of filled sites in the associated lattice gas.

1.3.4. Uncorrelated Polaron Disorder Models (PGDM). A final model not yet discussed is a polaronic version of the original uncorrelated Gaussian disorder model. Thus here what is referred to as the polaron Gaussian disorder model (PGDM) is introduced in which the energy landscape is drawn from an uncorrelated Gaussian distribution, spatial disorder is treated through Gaussian fluctuations char-

acterized by disorder parameter Σ, but the hopping rates are taken to be of the polaronic form (7). Since polaronic disorder-based theories emerged during and after recognition of the importance of spatial energy correlations, this particular variation does not seem to have been studied as extensively as some of the other models. This omission is partially corrected here, through analytical and numerical calculations. The numerical calculations presented in Section 4 appear to show that the use of polaronic rates by themselves, without spatial energy correlations, does a much better job of describing the Poole-Frenkel field dependence than the use of the Miller-Abraham rates, except at very low fields.

1.4. OVERVIEW OF NEW RESULTS

As suggested above, while there have been many studies of disorder based models focused on *qualitatively* explaining the electric field and temperature dependence of experimentally measured mobility data in MDPs, there appears to be no actual side-by-side comparison of experimentally measured mobility data with *quantitative* predictions of *any* of the disorder based theories described above. This is not altogether surprising. While the models themselves are fairly easy to describe theoretically, their predictions are not so easily obtained. It takes considerable computing power and time to generate the mobility data for any of these models at any fixed temperature as a function of the applied field.

The main goals of the research presented in this dissertation is to obtain a better understanding of the qualitative and quantitative differences that arise in the predictions of the different disorder-based models enumerated above, and to understand how the different features incorporated into the models manifest in different temperature and field dependences.

In the second section of this dissertation, a number of new analytical calculations on one-dimensional versions of the models discussed above are presented. These

results are exact for hopping motion on a one-dimensional chain in which hopping takes place only between nearest neighbor hopping. Specifically, an exact calculation of the mobility for 1D version of the GDM, CGDM, PCDM-Σ, and PGDM will be presented. Previous 1D calculations of this sort have appeared for the CGDM, but only within a certain approximation in which a three point correlation function appearing in the calculation was approximated as a two-point correlation function, and in which no geometrical disorder was assumed. The present work avoids that approximation, includes in a simple way the effects of Gaussian geometric disorder, and extends the calculation to other transport models that include Gaussian disorder. Although differences are expected to arise between one-dimensional and three-dimensional transport models, one might hope that the exact one-dimensional results can provide a qualitative guide to the differences that arise in bulk three dimensional samples.

The third section discusses the numerical approach that is used in section 4 of this dissertation to compute the mobility for three dimensional systems, and provides a comparison of that numerical method, which is based on a steady-state solution to the master equation (9), with the results of Monte Carlo calculations previously reported for the GDM.

In section 4, a detailed comparison of the predictions of the models discussed above are presented as they apply to the model compound 30% DEH:PC, using the experimental data of Mack, et al. [19], previously shown in Figure 1.6. These comparisons were obtained as a result of extensive numerical calculations in which the basic disorder parameters for each model were varied in an attempt to optimize the agreement between theory and experiment and represent several years worth of computational effort. In comparing published mobility data with the results of the different disorder models described above, experimentally reported or experimentally deducible values of the basic system parameters (a, γ, T, E) are used. With these

parameters considered to be fixed by experiment, a fitting of the GDM and the CGDM to experimental data requires a determination of three independent material parameters (ν_0, σ, Σ), where ν_0 is the attempt frequency, σ is the strength of the energetic disorder and Σ is the strength of the geometrical disorder. In the polaronic PCDM and PCDM-Σ, on the other hand, the relevant material parameters include the strength J_0 of the overlap integral, the energetic disorder σ, and the polaron binding energy E_B. For the original PCDM this gives three adjustable parameters (J_0, σ, E_B), the same number required by the GDM and the CGDM. By introducing geometrical disorder, PCDM-Σ becomes a four parameter model $(J_0, \sigma, E_B, \Sigma)$. As might be expected, this extra degree of freedom enhances the quality of the fit, and allows this model to do the best job of reproducing the experimental results. Comparing the parameters in the non-polaron and the polaron models, it has been noted that ν_0 and J_0^2 serve similar roles as purely multiplicative constants that set the overall scale of the mobility, but do not affect the temperature or field dependence. The energetic width σ associated with energetic disorder and the width Σ associated with geometric disorder do affect the mobility in a non-trivial way; they have essentially the same meaning in all the theories considered here, although the values deduced for them differ from one model to the next. The key difference between the polaronic and non-polaronic theories, therefore, is the presence or absence of the polaron binding energy E_B, which has *a priori*, the potential to introduce a different field and temperature dependence than that which arises with Miller-Abraham rates [56].

The fifth section of dissertation presents a numerical study of the differences that arise with different models of spatial disorder. Specifically, the predictions of the two versions of the polaron correlated disorder model that treat the disorder through Gaussian fluctuations, i.e., PCDM-Σ, and the version PCDM-c, which incorporates the disorder by treating the array of hopping sites as a randomly diluted lattice gas are compared. Interestingly, it has been found that the surprising GDM prediction that

the mobility increases with increasing disorder, is reversed at high fields in the lattice gas model, which makes the intuitively reasonable prediction that with increasing disorder, particularly at high electric fields, the mobility decreases with increased spatial disorder.

2. ANALYTICAL CALCULATIONS IN ONE-DIMENSION

In this section, exact analytical calculations of the charge carrier mobility at high fields in one-dimensional (1D), nearest-neighbor versions of the disorder-based hopping models described in the introduction are presented. The assumption of high electric fields is important here as it implies that the longitudinal motion in the direction of the applied electric field is much larger than the diffusional spreading transverse to it. Hence the transport path for the charge carriers through the material can be well-approximated by a quasi-one dimensional path through the material. While there are expected to be quantitative differences between charge transport in 1D and 3D disordered systems, it is to be hoped that the results obtained in this section might provide insight into the way the different features described in the introduction ultimately manifest themselves in the field and temperature dependence of the mobility.

For each model considered in this section, the starting point of the calculation is the master equation (9) describing the evolution of the site occupation probabilities $P_n(t)$, which is modified in this section to include only nearest-neighbor hops along the 1D chain, i.e.,

$$\frac{dP_n}{dt} = W_{n,n+1}P_{n+1} - W_{n+1,n}P_n + W_{n,n-1}P_{n+1} - W_{n-1,n}P_n. \tag{11}$$

For equations of this form, an exact solution for the steady-state drift velocity and diffusion constant has been obtained by Derrida [65]. In that calculation, Derrida considers a periodically repeated chain of N sites, and calculates the steady-state drift velocity

$$v = \lim_{t\to\infty} \frac{d\langle x\rangle}{dt} = \lim_{t\to\infty} \frac{d}{dt} \sum_n P_n(t)\, na \tag{12}$$

obtaining the result $v = a\langle r\rangle^{-1}$, which implies the following expression for the mobility

$$\mu = \frac{v}{E} = \frac{ea^2}{F}\langle r\rangle^{-1} \tag{13}$$

where $F = eEa$, and the quantity

$$\langle r\rangle = \langle r_n\rangle = \frac{1}{N}\sum_{n=1}^{N} r_n \tag{14}$$

can be explicitly expressed in terms of transition rates on the chain though the expression

$$\begin{aligned}\langle r_n\rangle &= \left\langle \frac{1}{W_{n+1,n}} + \frac{W_{n,n+1}}{W_{n+1,n}}\frac{1}{W_{n+2,n+1}} + \frac{W_{n,n+1}}{W_{n+1,n}}\frac{W_{n+1,n+2}}{W_{n+2,n+1}}\frac{1}{W_{n+3,n+2}} + \dots \right\rangle \\ &= \sum_m \langle r_n^{(m)}\rangle\end{aligned}$$

in which, for $m = 0$,

$$r_n^{(0)} = \frac{1}{W_{n+1,n}} \tag{15}$$

and for $m > 0$

$$r_n^{(m)} = \left(\prod_{\ell=0}^{m-1} \frac{W_{n+\ell,n+\ell+1}}{W_{n+\ell+1,n+\ell}}\right) \frac{1}{W_{n+m+1,n+m}}. \tag{16}$$

In the limit $N \to \infty$, the averages appearing in these expressions can be evaluated for specific models using the functional form of the transition rates that appear in them, and the corresponding probability distributions governing the spatial and energetic disorder.

In what follows such a calculation is explicitly performed for the GDM, the CGDM, the PCDM-Σ, and the PGDM.

2.1. CALCULATION OF THE MOBILITY FOR THE 1D GAUSSIAN DISORDER MODEL

In the GDM the site energies ε_n for transport sites along the chain are independently drawn from a Gaussian distribution

$$P(\varepsilon_n) = \frac{1}{\sqrt{2\pi\sigma^2}} \exp\left(-\frac{\varepsilon_n^2}{2\sigma^2}\right) \tag{17}$$

of energetic width σ, and hopping rates are of the Miller-Abraham type (8). The hopping rates $W_{n,n+1}$ from site $n+1$ to site n, and $W_{n+1,n}$ from site n to site $n+1$ in the presence of an electric field E, assumed to be directed to the right, can be written

$$W_{n,n+1} = \nu_0 e^{-(\Gamma_n+\Gamma_{n+1})} \exp\left(-\frac{\beta}{2}\left[(\varepsilon_n - \varepsilon_{n+1} + F) + |\varepsilon_n - \varepsilon_{n+1} + F|\right]\right) \tag{18}$$

$$W_{n+1,n} = \nu_0 e^{-(\Gamma_n+\Gamma_{n+1})} \exp\left(-\frac{\beta}{2}\left[(\varepsilon_{n+1} - \varepsilon_n - F) + |\varepsilon_{n+1} - \varepsilon_n - F|\right]\right) \tag{19}$$

where $F = eEa$ is the potential energy change induced across two sites by the field, $\beta = (kT)^{-1}$ is the inverse thermal energy, and the average wave function overlap factor $e^{-2\gamma a}$ has been incorporated in the definition of ν_0. The quantities Γ_n, which then describe Gaussian fluctuations in the wave function overlap factors, due, e.g., orientational disorder, and are thus distributed according to

$$P\left(\Gamma_n\right) = \frac{\exp\left(-\Gamma_n^2/\Sigma^2\right)}{\sqrt{\pi\Sigma^2}}. \tag{20}$$

The form written above for the hopping rate, which involves the absolute value of site energy differences, is equivalent to (8), in which hops up in energy depend on the energy difference, while hops down in energy do not. In the presence of the field the

detailed balance condition associated with neighboring sites takes the form

$$\frac{W_{n,n+1}}{W_{n+1,n}} = \exp\left(-\beta\left[(\varepsilon_n - \varepsilon_{n+1} + F)\right]\right). \tag{21}$$

With these assumptions the average of $r_n^{(0)}$ given in (15) can be written as

$$\begin{aligned}\langle r_n^{(0)}\rangle &= \left\langle \frac{1}{W_{n+1,n}} \right\rangle = \nu_0^{-1}\langle e^{\Gamma_n}\rangle^2 \left\langle \exp\left(\frac{\beta}{2}\left[(\varepsilon_{n+1} - \varepsilon_n - F) + |\varepsilon_{n+1} - \varepsilon_n - F|\right]\right)\right\rangle \\ &= \nu_0^{-1}\langle e^{\Gamma_n}\rangle^2 \hat{G}\end{aligned} \tag{22}$$

where in this last equation the average

$$\langle e^{\Gamma_n}\rangle^2 = \exp\left(\frac{1}{2}\Sigma^2\right)$$

over the Gaussian distribution (20) is easily computed to obtain

$$\begin{aligned}\hat{G} &= \left\langle \exp\left(\frac{\beta}{2}\left[(\varepsilon_{n+1} - \varepsilon_n - F) + |\varepsilon_{n+1} - \varepsilon_n - F|\right]\right)\right\rangle \\ &= \frac{1}{2\pi\sigma^2}\int_{-\infty}^{\infty} du\; e^{-u^2/2\sigma^2}\int_{-\infty}^{\infty} d\varepsilon\; e^{-\varepsilon^2/2\sigma^2}\exp\left(\frac{\beta}{2}\left[(u - \varepsilon - F) + |u - \varepsilon - F|\right]\right) \\ &= \hat{G}_1 + \hat{G}_2\end{aligned} \tag{23}$$

in which $u = \varepsilon_{n+1}$, and $\varepsilon = \varepsilon_n$, and in which are defined

$$\begin{aligned}\hat{G}_1 &= \frac{1}{\sqrt{2\pi\sigma^2}}\int_{-\infty}^{\infty} du\; e^{-u^2/(2\sigma^2)}\;\frac{1}{\sqrt{2\pi\sigma^2}}\int_{u-F}^{\infty} e^{-\varepsilon^2/\left(2\sigma^2\right)} d\varepsilon \\ &= \frac{1}{2}\frac{1}{\sqrt{2\pi\sigma^2}}\int_{-\infty}^{\infty} du\; e^{-u^2/(2\sigma^2)}\;\left(1 - \operatorname{erf}\left(\frac{u-F}{\sqrt{2\sigma^2}}\right)\right) \\ &= \frac{1}{2}\left(1 + \operatorname{erf}\left(\frac{F}{2\sigma}\right)\right)\end{aligned} \tag{24}$$

and

$$\begin{aligned}\hat{G}_2 &= \frac{1}{\sqrt{2\pi\sigma^2}}\int_{-\infty}^{\infty} du\; e^{-u^2/(2\sigma^2)}\; \frac{1}{\sqrt{2\pi\sigma^2}}\int_{-\infty}^{u-F}\; e^{-\varepsilon^2/\left(2\sigma^2\right)} \exp\left(\beta\left(u-\varepsilon-F\right)\right)\; d\varepsilon \\ &= \frac{1}{2}e^{-\beta F}e^{\frac{1}{2}\beta^2\sigma^2}\frac{1}{\sqrt{2\pi\sigma^2}}\int_{-\infty}^{\infty} du\; e^{-u^2/(2\sigma^2)}\; e^{\beta u}\left(1+\operatorname{erf}\left(\frac{u-F+\beta\sigma^2}{\sqrt{2\sigma^2}}\right)\right) du \\ &= \frac{1}{2}e^{-\beta F}e^{\beta^2\sigma^2}\left(1+\operatorname{erf}\left(\beta\sigma-\frac{F}{2\sigma}\right)\right). \end{aligned} \tag{25}$$

Combining the above equations it is found for $m = 0$ that

$$\langle r_n^{(0)}\rangle = \frac{1}{2}\nu_0^{-1}\langle e^{\Gamma}\rangle^2\left[\left(1+\operatorname{erf}\left(\frac{F}{2\sigma}\right)\right)+\; e^{-\beta F}e^{\beta^2\sigma^2}\left(1+\operatorname{erf}\left(\beta\sigma-\frac{F}{2\sigma}\right)\right)\right]. \tag{26}$$

For $m > 0$, the average of the quantity appearing in Eq.(16) can be evaluated in a similar fashion. By detailed balance, the product in parentheses can be written as

$$\begin{aligned}\prod_{\ell=0}^{m-1}\frac{W_{n+\ell,n+\ell+1}}{W_{n+\ell+1,n+\ell}} &= \prod_{\ell=0}^{m-1}\exp\left(-\beta\left[\left(\varepsilon_{n+\ell}-\varepsilon_{n+\ell+1}+F\right)\right]\right) \\ &= \exp\left(-\beta\sum_{\ell=0}^{m-1}\left[\left(\varepsilon_{n+\ell}-\varepsilon_{n+\ell+1}+F\right)\right]\right) \\ &= e^{-m\beta F}\exp\left(-\beta\left[\varepsilon_n-\varepsilon_{n+m}\right]\right). \end{aligned} \tag{27}$$

Thus, it can be written as

$$\begin{aligned}\langle r_n^{(m)}\rangle &= \nu_0^{-1}\langle e^{\Gamma}\rangle^2\; e^{-m\beta F}\Big\langle \exp-\left(\beta\left[\varepsilon_n-\varepsilon_{n+m}\right]\right) \\ &\qquad\times\exp\left(\frac{\beta}{2}\left[\left(\varepsilon_{n+m+1}-\varepsilon_{n+m}-F\right)+\left|\varepsilon_{n+m+1}-\varepsilon_{n+m}-F\right|\right]\right)\Big\rangle \\ &= \nu_0^{-1}\langle e^{\Gamma}\rangle^2\; e^{-m\beta F}\left\langle\exp\left(-\beta\varepsilon_n\right)\right\rangle\Big\langle \exp\left(\beta\varepsilon_{n+m}\right) \\ &\qquad\times\exp\left(\frac{\beta}{2}\left[\left(\varepsilon_{n+m+1}-\varepsilon_{n+m}-F\right)+\left|\varepsilon_{n+m+1}-\varepsilon_{n+m}-F\right|\right]\right)\Big\rangle \\ &= \nu_0^{-1}\langle e^{\Gamma}\rangle^2\; e^{-m\beta F}H_0H \end{aligned} \tag{28}$$

where

$$H_0 = \langle \exp(-\beta\varepsilon_n) \rangle = \frac{1}{\sqrt{2\pi\sigma^2}} \int_{-\infty}^{\infty} e^{-\beta u} e^{-u^2/(2\sigma^2)} du = e^{\frac{1}{2}\beta^2\sigma^2} \tag{29}$$

and

$$\begin{aligned} H &= \left\langle \exp(\beta\varepsilon_{n+m}) \exp\left(\frac{\beta}{2}\left[(\varepsilon_{n+m+1} - \varepsilon_{n+m} - F) + |\varepsilon_{n+m+1} - \varepsilon_{n+m} - F|\right]\right)\right\rangle \\ &= \frac{1}{2\pi\sigma^2} \int_{-\infty}^{\infty} du\, e^{-u^2/2\sigma^2} \int_{-\infty}^{\infty} d\varepsilon\, e^{-\varepsilon^2/2\sigma^2} e^{\beta\varepsilon} e^{\frac{1}{2}\beta[(u-\varepsilon-F)+|u-\varepsilon-F|]} \\ &= H_1 + H_2 \end{aligned} \tag{30}$$

where

$$\begin{aligned} H_1 &= \frac{1}{\sqrt{2\pi\sigma^2}} \int_{-\infty}^{\infty} du\, e^{-u^2/\left(2\sigma^2\right)} \frac{1}{\sqrt{2\pi\sigma^2}} \int_{u-F}^{\infty} e^{-\varepsilon^2/\left(2\sigma^2\right)} e^{\beta\varepsilon}\, d\varepsilon \\ &= \frac{1}{2} e^{\frac{1}{2}\beta^2\sigma^2} \frac{1}{\sqrt{2\pi\sigma^2}} \int_{-\infty}^{\infty} du\, e^{-u^2/\left(2\sigma^2\right)} \left(1 - \operatorname{erf}\left(\frac{u - F - \beta\sigma^2}{\sqrt{2\sigma^2}}\right)\right) \\ &= \frac{1}{2} e^{\frac{1}{2}\beta^2\sigma^2} \left[1 + \operatorname{erf}\left(\frac{1}{2}\left(\beta\sigma + \frac{F}{\sigma}\right)\right)\right], \end{aligned} \tag{31}$$

and

$$\begin{aligned} H_2 &= \frac{1}{\sqrt{2\pi\sigma^2}} \int_{-\infty}^{\infty} du\, e^{-u^2/(2\sigma^2)} \frac{1}{\sqrt{2\pi\sigma^2}} \int_{-\infty}^{u-F} e^{-\varepsilon^2/(2\sigma^2)} e^{\beta\varepsilon} e^{\beta(u-\varepsilon-F)}\, d\varepsilon \\ &= \frac{1}{2} e^{-\beta F} \frac{1}{\sqrt{2\pi\sigma^2}} \int_{-\infty}^{\infty} du\, e^{-u^2/(2\sigma^2)+\beta u} \left(1 + \operatorname{erf}\left(\frac{(u-F)}{\sqrt{2\sigma^2}}\right)\right) \\ &= \frac{1}{2} e^{-\beta F} e^{\frac{1}{2}\beta^2\sigma^2} \left(1 - \operatorname{erf}\left(\frac{F}{2\sigma}\right)\right). \end{aligned} \tag{32}$$

Thus, it is found that

$$H = \frac{1}{2} e^{\frac{1}{2}\beta^2\sigma^2} \left[\left(1 + \operatorname{erf}\left[\frac{1}{2}\left(\beta\sigma + \frac{F}{\sigma}\right)\right]\right) + e^{-\beta F}\left(1 - \operatorname{erf}\left(\frac{F}{2\sigma}\right)\right)\right]$$

and so

$$\begin{aligned}\langle r_n^{(m)}\rangle &= \nu_0^{-1}\langle e^{\Gamma}\rangle^2\, e^{-m\beta F} H_0 H \\ &= \frac{1}{2}\nu_0^{-1}\langle e^{\Gamma}\rangle^2\, e^{\beta^2\sigma^2}\, e^{-m\beta F}\Bigg[\left(1+\operatorname{erf}\left[\frac{1}{2}\left(\beta\sigma+\frac{F}{\sigma}\right)\right]\right) \\ &\qquad + e^{-\beta F}\left(1-\operatorname{erf}\left(\frac{F}{2\sigma}\right)\right)\Bigg]. \end{aligned} \tag{33}$$

With these results $\langle r\rangle$ can be then computed as

$$\langle r\rangle = \sum_{m=0}^{\infty}\langle r_n^{(m)}\rangle = \nu_0^{-1}\langle e^{\Gamma}\rangle^2\langle R\rangle \tag{34}$$

where

$$\begin{aligned}\langle R\rangle &= \frac{1}{2}\left(1+\operatorname{erf}\left(\frac{F}{2\sigma}\right)\right) + \; e^{-\beta F}e^{\beta^2\sigma^2}\left(1+\operatorname{erf}\left(\beta\sigma-\frac{F}{2\sigma}\right)\right) \\ &\quad + \frac{1}{2}e^{\beta^2\sigma^2}\;\left[\left(1+\operatorname{erf}\left[\frac{1}{2}\left(\beta\sigma+\frac{F}{\sigma}\right)\right]\right)+e^{-\beta F}\left(1-\operatorname{erf}\left(\frac{F}{2\sigma}\right)\right)\right]\sum_{m=1}^{\infty}e^{-m\beta F} \\ &= \frac{1}{2}\left(1+\operatorname{erf}\left(\frac{F}{2\sigma}\right)\right) + \; e^{-\beta F}e^{\beta^2\sigma^2}\left(1+\operatorname{erf}\left(\beta\sigma-\frac{F}{2\sigma}\right)\right) \\ &\quad + \frac{1}{2}e^{\beta^2\sigma^2}\;\left[\left(1+\operatorname{erf}\left[\frac{1}{2}\left(\beta\sigma+\frac{F}{\sigma}\right)\right]\right)+e^{-\beta F}\left(1-\operatorname{erf}\left(\frac{F}{2\sigma}\right)\right)\right]\frac{e^{-\beta F}}{1-e^{-\beta F}}. \end{aligned} \tag{35}$$

Thus, the mobility for the 1D version of the GDM can be written in the form, from (13), (34), as

$$\mu = \frac{e\nu_0 a^2}{F}\frac{1}{\langle R\rangle}\exp\left(-\frac{\Sigma^2}{2}\right) = \frac{\mu_0}{F\langle R\rangle} \tag{36}$$

with

$$\mu_0 = e\nu_0 a^2\exp\left(-\frac{\Sigma^2}{2}\right) \tag{37}$$

and $\langle R \rangle$ given by Eq.(35).

Figure 2.1 shows predictions for the scaled mobility μ/μ_0 of the 1D version of the GDM, as a function of the square root of the electric field, expressed in terms of the quantity $F/\sigma = eEa/\sigma$, for a system in which the energetic disorder parameter has a value $\sigma = 0.1\,\mathrm{eV}$ and $\Sigma = 0$, which is typical of those measured in MDPs. Curves are shown for different temperatures, ranging from 250K to 325K. As suggested in the Introduction, rather than lying on straight lines, the field dependence of the mobility of this one-dimensional version of the GDM shows significant curvature at intermediate fields, becoming very flat at low electric fields, in disagreement with most experimental results.

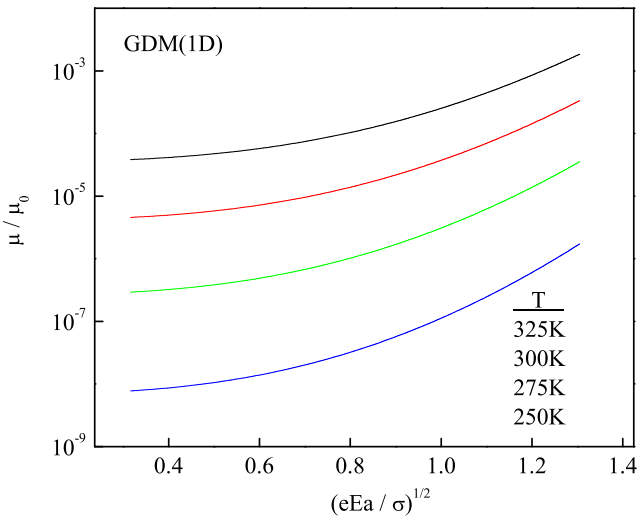

Figure 2.1. Normalized mobility of the GDM as a function of $\sqrt{eEa/\sigma}$ with $\sigma = 0.1$eV, for different temperatures as indicated.

It is noted also from this expression that in this 1D version of the GDM, the mobility decreases exponentially with the square of the magnitude of the geometrical

disorder parameter Σ. The theoretical results at a nonzero values of Σ (as seen in Figure 2.2 with $\sigma = 0.1\,\mathrm{eV}$ and $T = 300\,\mathrm{K}$, show that each curve on this logarithmic plot has the same shape as the corresponding curve in Figure 2.1, but that they are each displaced vertically downward by an amount that depends on the value of Σ.

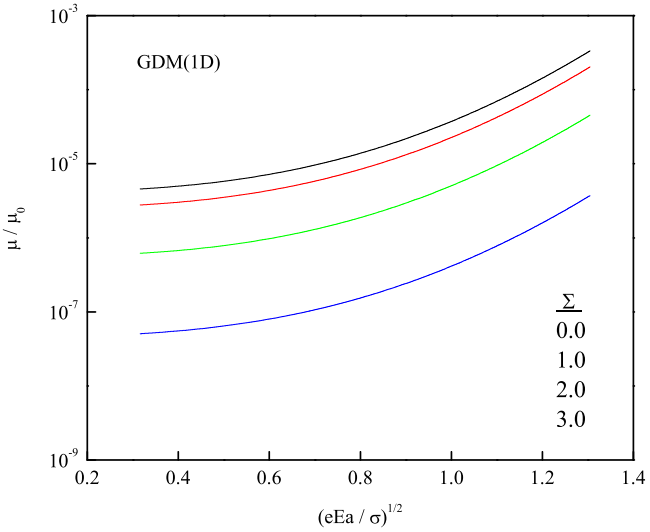

Figure 2.2. Normalized mobility of the GDM as a function of $\sqrt{eEa/\sigma}$ with $\sigma = 0.1$ eV and $T = 300$ K for different Σ as indicated.

2.2. CALCULATION OF THE MOBILITY FOR THE 1D CGDM

The CGDM uses the same Miller-Abraham hopping rates (18) and (19) as the GDM of the last subsection, but assumes a correlated Gaussian energy landscape as described by (5). Following Derrida's general development, the quantity $\langle r_n^{(m)} \rangle$ appearing in Eq.(16) can then be calculated. In the present model this can be formally

written in the same form as for the GDM, i.e.,

$$\begin{aligned}\langle r_n^{(m)}\rangle &= \nu_0^{-1}\left\langle e^{\Gamma}\right\rangle^2\ e^{-m\beta F}\Bigg\langle \exp\left(-\beta\left[\varepsilon_n-\varepsilon_{n+m}\right]\right)\\ &\qquad\times\exp\left(\frac{\beta}{2}\left[(\varepsilon_{n+m+1}-\varepsilon_{n+m}-F)+|\varepsilon_{n+m+1}-\varepsilon_{n+m}-F|\right]\right)\Bigg\rangle\\ &= \nu_0^{-1}\left\langle e^{\Gamma}\right\rangle^2\ e^{-m\beta F}M_m\end{aligned} \tag{38}$$

where

$$\begin{aligned}M_m = \Bigg\langle &\exp\left(-\beta\left[\varepsilon_n-\varepsilon_{n+m}\right]\right)\\ &\times\exp\left(\frac{\beta}{2}\left[(\varepsilon_{n+m+1}-\varepsilon_{n+m}-F)+|\varepsilon_{n+m+1}-\varepsilon_{n+m}-F|\right]\right)\Bigg\rangle.\end{aligned} \tag{39}$$

For $m=0$, this average now involves two correlated random variables ε_n and ε_{n+1}, while, for $m>0$, it also involves a third correlated random variable, ε_{n+m+1}. It is again necessary, therefore, to treat the two cases, $m=0$ and $m>0$, separately. For $m=0$, the general expression (39) reduces to

$$M_0 = \left\langle \exp\left(\frac{\beta}{2}\left[(\varepsilon_{n+1}-\varepsilon_n-F)+|\varepsilon_{n+1}-\varepsilon_n-F|\right]\right)\right\rangle. \tag{40}$$

To compute this average, which depends on two correlated energies, a 2×2 covariance matrix $C=C_0$ is defined with elements $C_{ij}=\langle u_i u_j\rangle$ where

$$u_1=\varepsilon_n \qquad \text{and} \qquad u_2=\varepsilon_{n+1}.$$

For dipolar disorder, as described by (4),

$$\langle \varepsilon_n\varepsilon_{n+k}\rangle = \frac{\sigma^2}{(|k|+1)} \tag{41}$$

so for $m = 0$ the covariance matrix and its inverse are symmetric

$$C = \frac{1}{2}\sigma^2 \begin{pmatrix} 2 & 1 \\ 1 & 2 \end{pmatrix} \qquad \Omega = \frac{2}{3\sigma^2} \begin{pmatrix} 2 & -1 \\ -1 & 2 \end{pmatrix} \tag{42}$$

and have determinants given by

$$|C| = \frac{3}{4}\sigma^4 \qquad |\Omega| = \frac{4}{3\sigma^4}. \tag{43}$$

In terms of these quantities, the joint probability distribution for the correlated Gaussian variables u_1 and u_2 can be expressed as

$$P(u_1, u_2) = \frac{1}{\sqrt{(2\pi)\,|C|}} \exp\left(-\frac{1}{2}\left(\Omega_{11}u_1^2 + 2\Omega_{12}u_1u_2 + \Omega_{22}u_2^2\right)\right) \tag{44}$$

and the mean value of interest as

$$\begin{aligned} M_0 &= \int_{-\infty}^{\infty} du_1 \int_{-\infty}^{\infty} du_2 \; P(u_1, u_2) \exp\left(\frac{\beta}{2}\left(u_2 - u_1 - F + |u_2 - u_1 - F|\right)\right) \\ &= \frac{1}{\sqrt{2\pi\,|C|}} \int_{-\infty}^{\infty} du_1 \; G(u_1) \end{aligned} \tag{45}$$

where

$$\begin{aligned} G(u_1) = \frac{1}{\sqrt{2\pi}} \int_{-\infty}^{\infty} du_2 \exp\left(-\frac{1}{2}\left(\Omega_{11}u_1^2 + 2\Omega_{12}u_1u_2 + \Omega_{22}u_2^2\right)\right) \\ \times \exp\left(\frac{\beta}{2}\left(u_2 - u_1 - F + |u_2 - u_1 - F|\right)\right). \end{aligned} \tag{46}$$

To treat the absolute value in the exponent, this last integral is broken into two parts, writing

$$G\left(u_1\right) = G_1\left(u_1\right) + G_2\left(u_1\right) \tag{47}$$

where

$$\begin{aligned} G_1\left(u_1\right) &= \frac{1}{\sqrt{2\pi}} \int_{-\infty}^{u_1+F} du_2 \exp\left(-\frac{1}{2}\left(\Omega_{11}u_1^2 + 2\Omega_{12}u_1u_2 + \Omega_{22}u_2^2\right)\right) \\ G_2\left(u_1\right) &= \frac{1}{\sqrt{2\pi}} \int_{u_1+F}^{\infty} du_2 \exp\left(-\frac{1}{2}\left(\Omega_{11}u_1^2 + 2\Omega_{12}u_1u_2 + \Omega_{22}u_2^2\right)\right) \\ &\qquad \times \exp\left(\beta\left(u_2 - u_1 - F\right)\right). \end{aligned}$$

Defining

$$\begin{aligned} a &= \frac{1}{2}\Omega_{22} & b &= \Omega_{12}u_1 \\ c &= \Omega_{12}u_1 - \beta = b - \beta & d &= u_1 + F \end{aligned} \tag{48}$$

it is found that

$$\begin{aligned} G_1\left(u_1\right) &= \frac{\exp\left(-\frac{1}{2}\Omega_{11}u_1^2\right)}{\sqrt{2\pi}} \int_{-\infty}^{d} \exp\left(-au_2^2 - bu_2\right) du_2 \\ &= \frac{1}{2} e^{-\frac{1}{2}\Omega_{11}u_1^2} \frac{1}{\sqrt{2a}} \exp\left(\frac{b^2}{4a}\right)\left(1 + \operatorname{erf}\left(\frac{b+2ad}{2\sqrt{a}}\right)\right) \\ &= \frac{1}{2}\frac{1}{\sqrt{\Omega_{22}}} \exp\left(-\lambda_0 u_1^2\right)\left(1 + \operatorname{erf}\left(r_0u_1 + t_{01}\right)\right) \\ &= G_{11}\left(u_1\right) + G_{12}\left(u_1\right) \end{aligned} \tag{49}$$

where

$$\begin{aligned}\lambda_0 &= \frac{1}{2}\frac{\Omega_{11}\Omega_{22}-\Omega_{12}^2}{\Omega_{22}} = \frac{1}{2}\frac{|\Omega|}{\Omega_{22}}\\ r_0 &= \frac{\Omega_{12}+\Omega_{22}}{\sqrt{2\Omega_{22}}}\\ t_{01} &= \frac{F\Omega_{22}}{\sqrt{2\Omega_{22}}}\end{aligned} \tag{50}$$

and

$$\begin{aligned}G_{11}(u_1) &= \frac{1}{2}\frac{1}{\sqrt{\Omega_{22}}}\exp\left(-\lambda_0 u_1^2\right)\\ G_{12}(u_1) &= G_{11}(u_1)\operatorname{erf}(r_0u_1+t_{01}).\end{aligned} \tag{51}$$

Similarly, $G_2(u_1)$ can be evaluated:

$$\begin{aligned}G_2(u_1) &= e^{-\frac{1}{2}\Omega_{11}u_1^2-\beta u_1-\beta F}\frac{1}{\sqrt{2\pi}}\int_d^\infty \exp\left(-au_2^2-cu_2\right)du_2\\ &= \frac{1}{2}e^{-\frac{1}{2}\Omega_{11}u_1^2-\beta u_1-\beta F}\frac{1}{\sqrt{2a}}\exp\left(\frac{c^2}{4a}\right)\left(1-\operatorname{erf}\left(\frac{c+2ad}{2\sqrt{a}}\right)\right)\\ &= \frac{1}{2}\frac{1}{\sqrt{\Omega_{22}}}\exp\left(-\lambda_0u_1^2-\nu_0u_1-\eta_0\right)\left(1-\operatorname{erf}(r_0u_1+t_{02})\right)\\ &= G_{21}(u_1)+G_{22}(u_1)\end{aligned} \tag{52}$$

in which

$$\begin{aligned}\nu_0 &= \beta\frac{\Omega_{22}+\Omega_{12}}{\Omega_{22}}\\ \eta_0 &= F\beta-\frac{\beta^2}{2\Omega_{22}}\\ t_{02} &= \frac{F\Omega_{22}-\beta}{\sqrt{2\Omega_{22}}}\end{aligned} \tag{53}$$

and

$$G_{21}(u_1) = \frac{1}{2}\frac{1}{\sqrt{\Omega_{22}}}\exp\left(-\lambda_0 u_1^2 - \nu_0 u_1 - \eta_0\right)$$
$$G_{22}(u_1) = -G_{21}(u_1)\,\mathrm{erf}\left(r_0 u_1 + t_{02}\right). \tag{54}$$

The mean value of interest for $m = 0$ can now be computed as the sum $M_0 = \sum_{\alpha,\beta} M_{\alpha,\beta}$ of four contributions, where

$$M_{\alpha,\beta} = \frac{1}{\sqrt{2\pi\,|C|}}\int_{-\infty}^{\infty} du_1\; G_{\alpha,\beta}(u_1). \tag{55}$$

More specifically, after some work it is found that

$$\begin{aligned} M_{11} &= \frac{1}{2}\frac{1}{\sqrt{\Omega_{22}\,|C|}}\frac{1}{\sqrt{2\pi}}\int_{-\infty}^{\infty}\exp\left(-\lambda_0 u_1^2\right)\; du_1 \\ &= \frac{1}{2}\frac{1}{\sqrt{\Omega_{22}\,|C|}}\frac{1}{\sqrt{2\lambda_0}} \\ &= \frac{1}{2}\frac{1}{\sqrt{|\Omega|\,|C|}} = \frac{1}{2}, \end{aligned} \tag{56}$$

$$\begin{aligned} M_{12} &= \frac{1}{2}\frac{1}{\sqrt{\Omega_{22}\,|C|}}\frac{1}{\sqrt{2\pi}}\int_{-\infty}^{\infty}\exp\left(-\lambda_0 u_1^2\right)\;\mathrm{erf}\left(r_0 u_1 + t_{01}\right)\; du_1 \\ &= \frac{1}{2}\frac{1}{\sqrt{\Omega_{22}\,|C|}}\frac{1}{\sqrt{2\lambda_0}}\,\mathrm{erf}\left(\frac{t_{01}}{\sqrt{1 + 2r_0^2/\left(2\lambda_0\right)}}\right) \\ &= \frac{1}{2}\,\mathrm{erf}\left(\frac{F/\sigma}{\sqrt{2}}\right), \end{aligned} \tag{57}$$

$$M_{21} = \frac{1}{2}\frac{1}{\sqrt{\Omega_{22}\,|C|}}\frac{1}{\sqrt{2\pi}}\int_{-\infty}^{\infty}\exp\left(-\lambda_0 u_1^2 - \nu_0 u_1 - \eta_0\right)\,du_1$$
$$= \frac{1}{2}\frac{1}{\sqrt{\Omega_{22}\,|C|}}\frac{1}{\sqrt{2\lambda_0}}e^{-\eta_0}\exp\left(\frac{\nu_0^2}{4\lambda_0}\right)$$
$$= \frac{1}{2}\exp\left(-F\beta\right)\exp\left(\frac{1}{2}\sigma^2\beta^2\right), \tag{58}$$

and

$$M_{22} = -\frac{1}{2}\frac{1}{\sqrt{\Omega_{22}\,|C|}}\frac{1}{\sqrt{2\pi}}\int_{-\infty}^{\infty}\exp\left(-\lambda_0 u_1^2 - \nu_0 u_1 - \eta_0\right)\mathrm{erf}\left(r_0 u_1 + t_{01}\right)\,du_1$$
$$= -\frac{1}{2}\frac{1}{\sqrt{\Omega_{22}\,|C|}}\frac{1}{\sqrt{2\lambda_0}}e^{-\eta_0}\exp\left(\frac{\nu_0^2}{4\lambda_0}\right)\mathrm{erf}\left(\frac{t_{02} - r_0\nu_0/\left(2\lambda_0\right)}{\sqrt{1 + 2r_0^2/\left(2\lambda_0\right)}}\right)$$
$$= -\frac{1}{2}\exp\left(-F\beta\right)\exp\left(\frac{1}{2}\sigma^2\beta^2\right)\mathrm{erf}\left(\frac{F/\sigma - \beta\sigma}{\sqrt{2}}\right). \tag{59}$$

Adding these four contributions, an explicit expression is obtained for the mean value

$$M_0 = \frac{1}{2}\left(1 + \mathrm{erf}\left(\frac{F/\sigma}{\sqrt{2}}\right)\right) + \frac{1}{2}\exp\left(-\beta F\right)\exp\left(\frac{1}{2}\beta^2\sigma^2\right)\left(1 - \mathrm{erf}\left(\frac{F/\sigma - \beta\sigma}{\sqrt{2}}\right)\right). \tag{60}$$

For $m > 0$, the mean value of interest depends on three correlated energies, $C = C_m$ is redefined as a 3×3 covariance matrix C, again with elements

$$C_{ij} = \langle u_i u_j \rangle \tag{61}$$

where now it is to be understood that for $m > 0$

$u_1 = \varepsilon_n,$

$u_2 = \varepsilon_{n+m}$

$u_3 = \varepsilon_{n+m+1}.$

For dipolar disorder described by (41), the covariance matrix takes the form

$$C = \sigma^2 \begin{pmatrix} 1 & \frac{1}{m+1} & \frac{1}{m+2} \\ \frac{1}{m+1} & 1 & \frac{1}{2} \\ \frac{1}{m+2} & \frac{1}{2} & 1 \end{pmatrix}. \tag{62}$$

The inverse of the covariance matrix is given by the relation

$$\Omega = C^{-1} = \kappa \begin{pmatrix} \frac{3(m+2)(m+1)}{2m(m+3)} & -\frac{1}{m} & -\frac{1}{(m+3)} \\ -\frac{1}{m} & \frac{2(m+1)^2}{m(m+2)} & -1 \\ -\frac{1}{(m+3)} & -1 & \frac{2(m+2)^2}{(m+3)(m+1)} \end{pmatrix} \tag{63}$$

where

$$\kappa = \frac{2(m+1)(m+2)}{(3m^2+9m+8)} \frac{1}{\sigma^2}. \tag{64}$$

The determinant of the covariant matrix is

$$|C| = \frac{m(m+3)(3m^2+9m+8)}{4(m+1)^2(m+2)^2} \sigma^6. \tag{65}$$

In the analysis that follows, the matrix elements, the determinant, and certain minors or cofactors of the matrix Ω appear. Since the matrix Ω is symmetric, it is found that

$$|\Omega| = |C|^{-1} = \Omega_{11}\Omega_{22}\Omega_{33} - \Omega_{33}\Omega_{12}^2 + 2\Omega_{12}\Omega_{13}\Omega_{23} - \Omega_{22}\Omega_{13}^2 - \Omega_{11}\Omega_{23}^2 \tag{66}$$

$$= \frac{4(m+1)^2(m+2)^2}{m(m+3)(3m^2+9m+8)} \sigma^{-6}. \tag{67}$$

In addition, the explicit form taken by the following cofactors $|\Omega|_{ij}$ of the 2×2 matrices $[\Omega]_{ij}$ is obtained from Ω by striking out the i th column and jth row:

$$
\begin{aligned}
|\Omega|_{11} &= \Omega_{22}\Omega_{33} - \Omega_{23}^2 \\
|\Omega|_{22} &= \Omega_{11}\Omega_{33} - \Omega_{13}^2 \\
|\Omega|_{12} &= \Omega_{12}\Omega_{33} - \Omega_{13}\Omega_{23} \\
|\Omega|_{13} &= \Omega_{12}\Omega_{23} - \Omega_{13}\Omega_{22}.
\end{aligned} \tag{68}
$$

The joint probability distribution for the three correlated Gaussian variables u_1, u_2, and u_3 can then be written as

$$
P(u_1, u_2, u_3) = \frac{1}{\sqrt{(2\pi)^3 |C|}} \exp\left(-\frac{1}{2} \sum_{\alpha=1}^{3} \sum_{\beta=1}^{3} u_\alpha \Omega_{\alpha\beta} u_\beta \right). \tag{69}
$$

As stated in the preliminary remarks, it is interesting to calculate the mean value of M_m, redefining Eq.(39) as

$$
M_m = \left\langle \exp\left(-\beta\left[u_1 - u_2\right]\right) \exp\left(\frac{\beta}{2} \left[(u_3 - u_2 - F) + |u_3 - u_2 - F| \right] \right) \right\rangle \tag{70}
$$

which can be written

$$
\begin{aligned}
M_m &= \int_{-\infty}^{\infty} du_1 \int_{-\infty}^{\infty} du_2 \int_{-\infty}^{\infty} du_3 \; P(u_1, u_2, u_3) \exp\left(-\beta\left(u_1 - u_2\right)\right) \\
&\qquad \times \exp\left(\frac{\beta}{2} \left(u_3 - u_2 - F + |u_3 - u_2 - F| \right) \right) \\
&= \frac{1}{\sqrt{(2\pi)^2 |C|}} \int_{-\infty}^{\infty} du_1 \int_{-\infty}^{\infty} du_2 \; F(u_1, u_2)\, G(u_1, u_2) \\
&= \frac{1}{\sqrt{2\pi\, |C|}} \int_{-\infty}^{\infty} du_1 \; H(u_1)
\end{aligned} \tag{71}
$$

in which

$$H(u_1) = \frac{1}{\sqrt{2\pi}} \int_{-\infty}^{\infty} du_2 \; F(u_1, u_2)\, G(u_1, u_2)\,, \tag{72}$$

while

$$F(u_1, u_2) = \exp(-\beta(u_1 - u_2)) \exp\left(-\frac{1}{2}\left(\Omega_{11}u_1^2 + \Omega_{22}u_2^2 + 2u_1\Omega_{12}u_2\right)\right), \tag{73}$$

and

$$G(u_1, u_2) = \frac{1}{\sqrt{2\pi}} \int_{-\infty}^{\infty} du_3 \exp\left(-\frac{1}{2}\left(\Omega_{33}u_3^2 + 2u_2\Omega_{23}u_3 + 2u_1\Omega_{13}u_3\right)\right) \times \exp\left(\frac{\beta}{2}\left[u_3 - u_2 - F + |u_3 - u_2 - F|\right]\right). \tag{74}$$

As with the calculation of M_0, to treat the absolute value, this last integral is broken into two parts, writing

$$G(u_1, u_2) = G_1(u_1, u_2) + G_2(u_1, u_2) \tag{75}$$

where

$$G_1(u_1, u_2) = \frac{1}{\sqrt{2\pi}} \int_{-\infty}^{u_2+F} du_3 \exp\left(-\frac{1}{2}\left(\Omega_{33}u_3^2 + 2u_2\Omega_{23}u_3 + 2u_1\Omega_{13}u_3\right)\right) \tag{76}$$

$$G_2(u_1, u_2) = \frac{1}{\sqrt{2\pi}} \int_{u_2+F}^{\infty} du_3 \exp\left(-\frac{1}{2}\left(\Omega_{33}u_3^2 + 2u_2\Omega_{23}u_3 + 2u_1\Omega_{13}u_3\right)\right) \times \exp(\beta(u_3 - u_2 - F))\,. \tag{77}$$

Defining

$$a = \frac{1}{2}\Omega_{33} \qquad b = u_2\Omega_{23} + u_1\Omega_{13}$$
$$c = b - \beta = u_2\Omega_{23} + u_1\Omega_{13} - \beta \qquad d = u_2 + F \tag{78}$$

one can write

$$\begin{aligned} G_1(u_1, u_2) &= \frac{1}{\sqrt{2\pi}} \int_{-\infty}^{d} e^{-au_3^2 - bu_3} du_3 \\ &= \frac{1}{2}\frac{1}{\sqrt{2a}} \exp\left(\frac{b^2}{4a}\right)\left(1 + \operatorname{erf}\left(\frac{b + 2ad}{2\sqrt{a}}\right)\right) \\ &= \frac{1}{2}\frac{1}{\sqrt{\Omega_{33}}} \exp\left(\frac{(u_2\Omega_{23} + u_1\Omega_{13})^2}{2\Omega_{33}}\right) \\ &\qquad \times \left(1 + \operatorname{erf}\left(\frac{u_2\Omega_{23} + u_1\Omega_{13} + \Omega_{33}(u_2 + F)}{\sqrt{2\Omega_{33}}}\right)\right) \\ &= G_{11}(u_1, u_2) + G_{12}(u_1, u_2) \end{aligned} \tag{79}$$

in which

$$\begin{aligned} G_{11}(u_1, u_2) &= \frac{1}{2}\frac{1}{\sqrt{\Omega_{33}}} \exp\left(\frac{(u_2\Omega_{23} + u_1\Omega_{13})^2}{2\Omega_{33}}\right) \\ G_{12}(u_1, u_2) &= G_{11}(u_1, u_2)\ \operatorname{erf}\left(\frac{u_2\Omega_{23} + u_1\Omega_{13} + \Omega_{33}(u_2 + F)}{\sqrt{2\Omega_{33}}}\right), \end{aligned} \tag{80}$$

and

$$\begin{aligned} G_2(u_1,u_2) &= e^{-\beta(u_2+F)}\frac{1}{\sqrt{2\pi}}\int_d^\infty e^{-au_3^2-cu_3}\,du_3 \\ &= \frac{1}{2}\frac{1}{\sqrt{2a}}e^{-\beta(u_2+F)}\exp\left(\frac{c^2}{4a}\right)\left(1-\operatorname{erf}\left(\frac{c+2ad}{2\sqrt{a}}\right)\right) \\ &= \frac{1}{2}\frac{1}{\sqrt{\Omega_{33}}}e^{-\beta(u_2+F)}\exp\left(\frac{\left(u_2\Omega_{23}+u_1\Omega_{13}-\beta\right)^2}{2\Omega_{33}}\right) \\ &\quad\times\left(1-\operatorname{erf}\left(\frac{u_2\Omega_{23}+u_1\Omega_{13}-\beta+\Omega_{33}(u_2+F)}{\sqrt{2\Omega_{33}}}\right)\right) \\ &= G_{21}(u_1,u_2)+G_{22}(u_1,u_2) \end{aligned} \tag{81}$$

in which

$$\begin{aligned} G_{21}(u_1,u_2) &= \frac{1}{2}\frac{1}{\sqrt{\Omega_{33}}}e^{-\beta(u_2+F)}\exp\left(\frac{\left(u_2\Omega_{23}+u_1\Omega_{13}-\beta\right)^2}{2\Omega_{33}}\right) \\ G_{22}(u_1,u_2) &= -G_{21}(u_1,u_2)\operatorname{erf}\left(\frac{u_2\Omega_{23}+u_1\Omega_{13}-\beta+\Omega_{33}(u_2+F)}{\sqrt{2\Omega_{33}}}\right). \end{aligned} \tag{82}$$

With these intermediate results in hand it is now possible to consider the integral

$$\begin{aligned} H(u_1) &= \frac{1}{\sqrt{2\pi}}\int_{-\infty}^\infty du_2 F(u_1,u_2)\,G(u_1,u_2) \\ &= H_{11}(u_1)+H_{12}(u_1)+H_{21}(u_1)+H_{22}(u_1) \end{aligned} \tag{83}$$

in which

$$H_{\alpha\beta}(u_1) = \frac{1}{\sqrt{2\pi}}\int_{-\infty}^\infty du_2 \;\; F(u_1,u_2)\;\; G_{\alpha\beta}(u_1,u_2) \qquad\qquad \alpha,\beta\in\{1,2\} \tag{84}$$

or, more specifically,

$$H_{11}(u_1) = \frac{1}{2}\frac{1}{\sqrt{\Omega_{33}}}\frac{1}{\sqrt{2\pi}}\int_{-\infty}^{\infty} du_2 \exp\left(-\beta\left(u_1-u_2\right)\right)\exp\left(\frac{\left(u_2\Omega_{23}+u_1\Omega_{13}\right)^2}{2\Omega_{33}}\right) \times \exp\left(-\frac{1}{2}\left(\Omega_{11}u_1^2+\Omega_{22}u_2^2+2u_1\Omega_{12}u_2\right)\right) \tag{85}$$

$$H_{12}(u_1) = \frac{1}{2}\frac{1}{\sqrt{\Omega_{33}}}\frac{1}{\sqrt{2\pi}}\int_{-\infty}^{\infty} du_2 \ \exp\left(-\beta\left(u_1-u_2\right)\right) \ \exp\left(\frac{\left(u_2\Omega_{23}+u_1\Omega_{13}\right)^2}{2\Omega_{33}}\right) \times \exp\left(-\frac{1}{2}\left(\Omega_{11}u_1^2+\Omega_{22}u_2^2+2u_1\Omega_{12}u_2\right)\right) \times \operatorname{erf}\left(\frac{u_2\Omega_{23}+u_1\Omega_{13}+\Omega_{33}\left(u_2+F\right)}{\sqrt{2\Omega_{33}}}\right) \tag{86}$$

$$\begin{aligned} H_{21}(u_1) &= \frac{1}{2}\frac{1}{\sqrt{\Omega_{33}}}\frac{1}{\sqrt{2\pi}}\int_{-\infty}^{\infty} du_2 \ \exp\left(-\beta\left(u_1-u_2\right)\right)\exp\left(\frac{\left(u_2\Omega_{23}+u_1\Omega_{13}-\beta\right)^2}{2\Omega_{33}}\right) \\ &\quad \times \exp\left(-\beta\left(u_2+F\right)\right)\exp\left(-\frac{1}{2}\left(\Omega_{11}u_1^2+\Omega_{22}u_2^2+2u_1\Omega_{12}u_2\right)\right) \\ &= \frac{1}{2}\frac{\exp\left(-\beta F\right)}{\sqrt{\Omega_{33}}}\frac{1}{\sqrt{2\pi}}\int_{-\infty}^{\infty} du_2 \ \exp\left(-\beta u_1\right)\exp\left(\frac{\left(u_2\Omega_{23}+u_1\Omega_{13}-\beta\right)^2}{2\Omega_{33}}\right) \\ &\quad \times \exp\left(-\frac{1}{2}\left(\Omega_{11}u_1^2+\Omega_{22}u_2^2+2u_1\Omega_{12}u_2\right)\right) \end{aligned} \tag{87}$$

$$H_{22}(u_1) = -\frac{1}{2}\frac{\exp\left(-\beta F\right)}{\sqrt{\Omega_{33}}}\frac{1}{\sqrt{2\pi}}\int_{-\infty}^{\infty} du_2 \ \exp\left(-\beta u_1\right)\exp\left(\frac{\left(u_2\Omega_{23}+u_1\Omega_{13}-\beta\right)^2}{2\Omega_{33}}\right) \times \exp\left(-\frac{1}{2}\left(\Omega_{11}u_1^2+\Omega_{22}u_2^2+2u_1\Omega_{12}u_2\right)\right) \times \operatorname{erf}\left(\frac{u_2\Omega_{23}+u_1\Omega_{13}-\beta+\Omega_{33}\left(u_2+F\right)}{\sqrt{2\Omega_{33}}}\right). \tag{88}$$

Starting with $H_{11}(u_1)$, combining the exponential factors appearing in the definition of the function $H_{11}(u_1)$, and expanding the combined argument in powers of u_1 it is found that

$$\begin{aligned}
H_{11}(u_1) &= \frac{1}{2}\frac{1}{\sqrt{\Omega_{33}}}\frac{1}{\sqrt{2\pi}}\int_{-\infty}^{\infty} e^{-\alpha_1 u_2^2+\gamma_1 u_2-\delta_1}\, du_2 \\
&= \frac{1}{2}\frac{\exp(-\delta_1)}{\sqrt{\Omega_{33}}}\frac{1}{\sqrt{2\alpha_1}}\exp\left(\frac{\gamma_1^2}{4\alpha_1}\right) \\
&= \frac{1}{2}\frac{1}{\sqrt{|\Omega|_{11}}}\exp\left(-\left(\beta u_1+\frac{1}{2}\left(\frac{\Omega_{11}\Omega_{33}-\Omega_{13}^2}{\Omega_{33}}\right)u_1^2\right)\right) \\
&\qquad\qquad \times\exp\left(\frac{\left(\beta\Omega_{33}+(\Omega_{13}\Omega_{23}-\Omega_{12}\Omega_{33})\,u_1\right)^2}{2\,|\Omega|_{11}}\right) \\
&= \frac{1}{2}\frac{1}{\sqrt{|\Omega|_{11}}}e^{-\lambda_1 u_1^2-\nu_1 u_1+\eta_1}
\end{aligned} \tag{89}$$

where

$$\begin{aligned}
\alpha_1 &= \frac{1}{2}\frac{\Omega_{22}\Omega_{33}-\Omega_{23}^2}{\Omega_{33}} = \frac{1}{2}\frac{|\Omega|_{11}}{\Omega_{33}}, \\
\gamma_1 &= -\beta+u_1\frac{\Omega_{12}\Omega_{33}-\Omega_{13}\Omega_{23}}{\Omega_{33}}, \text{ and} \\
\delta_1 &= \beta u_1+\frac{1}{2}\frac{\Omega_{11}\Omega_{33}-\Omega_{13}^2}{\Omega_{33}}u_1^2 = \beta u_1+\frac{1}{2}\frac{|\Omega|_{22}}{\Omega_{33}}u_1^2
\end{aligned} \tag{90}$$

and where in the integrated form

$$\begin{aligned}
\lambda_1 &= \frac{\Omega_{11}\Omega_{22}\Omega_{33}-\Omega_{33}\Omega_{12}^2+2\Omega_{12}\Omega_{13}\Omega-\Omega_{22}\Omega_{13}^2-\Omega_{11}\Omega_{23}^2}{2\left(\Omega_{22}\Omega_{33}-\Omega_{23}^2\right)} = \frac{|\Omega|}{2\,|\Omega|_{11}} \\
\nu_1 &= \beta\frac{(\Omega_{22}\Omega_{33}-\Omega_{23}^2)+(\Omega_{12}\Omega_{33}-\Omega_{13}\Omega_{23})}{\Omega_{22}\Omega_{33}-\Omega_{23}^2} = \beta\frac{|\Omega|_{11}+|\Omega|_{12}}{|\Omega|_{11}} \\
\eta_1 &= \frac{\beta^2}{2}\frac{\Omega_{33}}{|\Omega|_{11}}.
\end{aligned} \tag{91}$$

The corresponding contribution to the mean value $M_m = \sum M_{\alpha\beta}$ can be identified as

$$\begin{aligned} M_{11} &= \frac{1}{\sqrt{2\pi\,|C|}} \int_{-\infty}^{\infty} du_1\ H_{12}\,(u_1) \\ &= \frac{1}{2} \frac{1}{\sqrt{2\pi\,|C|}} \frac{1}{\sqrt{|\Omega|_{11}}} \int_{-\infty}^{\infty} e^{-\lambda_1 u_1^2 - \nu_1 u_1 + \eta_1}\ du_1 \\ &= \frac{1}{2} \frac{1}{\sqrt{2\pi\,|C|}} \frac{1}{\sqrt{|\Omega|_{11}}} \frac{\sqrt{\pi}}{\sqrt{\lambda_1}} \exp\left(\frac{\nu_1^2}{4\lambda_1} + \eta_1\right) \\ &= \frac{1}{2} \frac{1}{\sqrt{|C|}} \frac{1}{\sqrt{|\Omega|}} \exp\left(\frac{\nu_1^2}{4\lambda_1} + \eta_1\right) \\ &= \frac{1}{2} \exp\left(\frac{\nu_1^2}{4\lambda_1} + \eta_1\right). \end{aligned} \tag{92}$$

The numerical prefactor has reduced to the single factor of $1/2$, but it seems the rest of this expression is best left in terms of the quantities ν_1, η_1, and λ_1 explicitly defined in (91) above in terms of the matrix elements and cofactors of the matrix Ω.

In a similar way, the function $H_{12}\,(u_1)$ can be written

$$H_{12}\,(u_1) = \frac{1}{2} \frac{1}{\sqrt{\Omega_{33}}} \frac{1}{\sqrt{2\pi}} \int_{-\infty}^{\infty} e^{-\alpha_1 u_2^2 - \gamma_1 u_2 - \delta_1}\ \operatorname{erf}\left(\rho_1 u_2 + \tau_1\right)\ du_2 \tag{93}$$

in which, the exponential parts are exactly the same as for H_{11}, and where the coefficients in the argument of the error function are

$$\begin{aligned} \rho_1 &= \frac{\Omega_{23} + \Omega_{33}}{\sqrt{2\Omega_{33}}} \\ \tau_1 &= \frac{F\Omega_{33} + \Omega_{13} u_1}{\sqrt{2\Omega_{33}}}. \end{aligned} \tag{94}$$

The integral can be performed using the identity

$$\frac{1}{\sqrt{2\pi}} \int_{-\infty}^{\infty} dx\ e^{-\alpha x^2 \pm \gamma x}\ \operatorname{erf}\left(\rho x + \tau\right) = \frac{1}{\sqrt{2\alpha}} \exp\left(\frac{\gamma^2}{4\alpha}\right) \operatorname{erf}\left(\frac{\tau \pm \rho\gamma/\left(2\alpha\right)}{\sqrt{1 + 2\rho^2/\left(2\alpha\right)}}\right) \tag{95}$$

from which one finds that

$$\begin{aligned} H_{12}(u_1) &= \frac{1}{2}\frac{1}{\sqrt{\Omega_{33}}}\frac{1}{\sqrt{2\pi}}\int_{-\infty}^{\infty} e^{-\alpha_1 u_2^2-\gamma_1 u_2-\delta_1}\,\mathrm{erf}\left(\rho_1 u_2+\tau_1\right)\,du_2 \\ &= \frac{1}{2}\frac{1}{\sqrt{\Omega_{33}}}\frac{1}{\sqrt{2\alpha_1}}\exp\left(-\delta_1\right)\exp\left(\frac{\gamma_1^2}{4\alpha_1}\right)\mathrm{erf}\left(\frac{\tau_1-\rho_1\gamma_1/(2\alpha_1)}{\sqrt{1+\rho_1^2/\alpha_1}}\right) \\ &= H_{11}(u_1)\,\mathrm{erf}\left(\frac{\tau_1-\rho_1\gamma_1/(2\alpha_1)}{\sqrt{1+\rho_1^2/\alpha_1}}\right) \\ &= \frac{1}{2}\frac{1}{\sqrt{|\Omega|_{11}}}e^{-\lambda_1 u_1^2-\nu_1 u_1+\eta_1}\,\mathrm{erf}\left(r_1 u_1+t_1\right) \end{aligned} \tag{96}$$

where use has been made of the fact that the exponential coefficients in H_{11} and H_{12} are the same, so that the exponential coefficients in the last line are also the same, and the argument of the error function in the last line has been expanded in terms of the quantities

$$\begin{aligned} r_1 &= \frac{\left(\Omega_{13}\left(\Omega_{22}+\Omega_{23}\right)-\Omega_{12}\left(\Omega_{23}+\Omega_{33}\right)\right)}{\sqrt{2\left(\Omega_{22}\Omega_{33}-\Omega_{23}^2\right)\left(\Omega_{22}+2\Omega_{23}+\Omega_{33}\right)}} \\ &= -\frac{\left(|\Omega|_{13}+|\Omega|_{12}\right)}{\sqrt{2\,|\Omega|_{11}\left(\Omega_{22}+2\Omega_{23}+\Omega_{33}\right)}} \\ t_1 &= \frac{\left(F\,|\Omega|_{11}+\beta\left(\Omega_{23}+\Omega_{33}\right)\right)}{\sqrt{2\,|\Omega|_{11}\left(\Omega_{22}+2\Omega_{23}+\Omega_{33}\right)}}. \end{aligned} \tag{97}$$

The sign of the coefficients depends on the fact that the quantity $|\Omega|_{11}=\left(\Omega_{22}\Omega_{33}-\Omega_{23}^2\right)$ is itself positive, as is readily verified from the explicit values for the matrix elements given in (63). The corresponding contribution to the mean value M can be identified

as

$$
\begin{aligned}
M_{12} &= \frac{1}{\sqrt{2\pi\,|C|}} \int_{-\infty}^{\infty} du_1\ H_{12}\left(u_1\right) \\
&= \frac{1}{2}\frac{\exp\left(\eta_1\right)}{\sqrt{|\Omega|_{11}}}\frac{1}{\sqrt{|C|}}\frac{1}{\sqrt{2\pi}} \int_{-\infty}^{\infty} \exp\left(-\lambda_1 u_1^2 - \nu_1 u_1\right) \operatorname{erf}\left(r_1 u_1 + t_1\right)\ du_1 \\
&= \frac{1}{2}\frac{\exp\left(\eta_1\right)}{\sqrt{|\Omega|_{11}}}\frac{1}{\sqrt{|C|}}\frac{1}{\sqrt{2\lambda_1}} \exp\left(\frac{\nu_1^2}{4\lambda_1}\right) \operatorname{erf}\left(\frac{t_1 - r_1\nu_1/\left(2\lambda_1\right)}{\sqrt{1 + r_1^2/\lambda_1}}\right) \\
&= \frac{1}{2}\exp\left(\frac{\nu_1^2}{4\lambda_1} + \eta_1\right) \operatorname{erf}\left(\frac{t_1 - r_1\nu_1/\left(2\lambda_1\right)}{\sqrt{1 + r_1^2/\lambda_1}}\right) \\
&= M_{11} \operatorname{erf}\left(\frac{t_1 - r_1\nu_1/\left(2\lambda_1\right)}{\sqrt{1 + r_1^2/\lambda_1}}\right)
\end{aligned} \tag{98}
$$

which, again at this point is probably best left in terms of the reduced variables defined above.

In a similar fashion, the function $H_{21}\left(u_1\right)$ can be written

$$
\begin{aligned}
H_{21}(u_1) &= \frac{1}{2}\frac{1}{\sqrt{\Omega_{33}}}\frac{1}{\sqrt{2\pi}} \int_{-\infty}^{\infty} e^{-\alpha_2 u_2^2 - \gamma_2 u_2 - \delta_2}\ du_2 \\
&= \frac{1}{2}\frac{1}{\sqrt{\Omega_{33}}}\exp\left(-\delta_2\right)\frac{1}{\sqrt{2\alpha_2}}\exp\left(\frac{\gamma_2^2}{4\alpha_2}\right) \\
&= \frac{1}{2}\frac{1}{\sqrt{|\Omega|_{11}}}\exp\left(-\delta_2\right)\exp\left(\frac{\gamma_2^2}{4\alpha_2}\right) \\
&= \frac{1}{2}\frac{1}{\sqrt{|\Omega|_{11}}} e^{-\lambda_2 u_1^2 - \nu_2 u_1 + \eta_2}
\end{aligned} \tag{99}
$$

where

$$
\begin{aligned}
\alpha_2 &= \frac{1}{2}\left(\frac{\Omega_{22}\Omega_{33} - \Omega_{23}^2}{\Omega_{33}}\right) = \frac{1}{2}\frac{|\Omega|_{11}}{\Omega_{33}} = \alpha_1 \equiv \alpha \\
\gamma_2 &= \left(\beta\frac{\Omega_{23}}{\Omega_{33}} + \left(\frac{\Omega_{12}\Omega_{33} - \Omega_{23}\Omega_{13}}{\Omega_{33}}\right)u_1\right) \\
\delta_2 &= \left(\beta\left(u_1 + F\right) - \frac{1}{2\Omega_{33}}\left(\beta - \Omega_{13}u_1\right)^2 + \frac{1}{2}\Omega_{11}u_1^2\right)
\end{aligned} \tag{100}
$$

and

$$\begin{aligned}
\lambda_2 &= \frac{|\Omega|}{2\,|\Omega|_{11}} = \lambda_1 \equiv \lambda, \\
\nu_2 &= \frac{\beta\left(|\Omega|_{11} + |\Omega|_{12}\right)}{|\Omega|_{11}} = \nu_1 \equiv \nu, \\
\eta_2 &= \frac{\beta^2 \Omega_{22}}{2\,|\Omega|_{11}} - \beta F.
\end{aligned} \tag{101}$$

The corresponding contribution M_{21} to the mean value M is

$$\begin{aligned}
M_{21} &= \frac{1}{\sqrt{2\pi\,|C|}} \int_{-\infty}^{\infty} du_1\ H_{21}\left(u_1\right) \\
&= \frac{1}{2} \frac{\exp\left(\eta_2\right)}{\sqrt{2\pi\,|C|}} \frac{1}{\sqrt{|\Omega|_{11}}} \int_{-\infty}^{\infty} e^{-\lambda_2 u_1^2 - \nu_2 u_1} du \\
&= \frac{1}{2} \frac{\exp\left(\eta_2\right)}{\sqrt{2\pi\,|C|}} \frac{1}{\sqrt{|\Omega|_{11}}} \frac{\sqrt{\pi}}{\sqrt{\lambda_2}} \exp\left(\frac{\nu_2^2}{4\lambda_2}\right) \\
&= \frac{1}{2} \frac{1}{\sqrt{|C|}} \frac{1}{\sqrt{|\Omega|}} \exp\left(\frac{\nu_2^2}{4\lambda_2} - \eta_2\right) \\
&= \frac{1}{2} \exp\left(\frac{\nu_2^2}{4\lambda_2} - \eta_2\right).
\end{aligned} \tag{102}$$

Finally, the function $H_{22}\left(u_1\right)$ can be written

$$H_{22}\left(u_1\right) = -\frac{1}{2} \frac{1}{\sqrt{\Omega_{33}}} \frac{1}{\sqrt{2\pi}} \int_{-\infty}^{\infty} e^{-\alpha_2 u_2^2 - \gamma_2 u_2 - \delta_2}\ \operatorname{erf}\left(\rho_2 u_2 + \tau_2\right)\ du_2 \tag{103}$$

in which, again, the exponential parts in the integrand of H_{21} and H_{22} are the same, and where the coefficients in the argument of the error function in the integrand are

$$\begin{aligned}
\rho_2 &= \frac{\left(\Omega_{23} + \Omega_{33}\right)}{\sqrt{2\Omega_{33}}} \\
\tau_2 &= \frac{\left(F\Omega_{33} + \Omega_{13} u_1 - \beta\right)}{\sqrt{2\Omega_{33}}}.
\end{aligned} \tag{104}$$

Integrating Eq.(103) it is found that

$$\begin{aligned} H_{22}(u_1) &= -\frac{1}{2}\frac{1}{\sqrt{\Omega_{33}}}\frac{\exp(-\delta_2)}{\sqrt{2\alpha_2}}\exp\left(\frac{\gamma_2^2}{4\alpha_2}\right)\operatorname{erf}\left(\frac{\tau_2-\rho_2\gamma_2/(2\alpha_2)}{\sqrt{1+2\rho_2^2/(2\alpha_2)}}\right) \\ &= -H_{21}\operatorname{erf}\left(\frac{\tau_2-\rho_2\gamma_2/(2\alpha_2)}{\sqrt{1+2\rho_2^2/(2\alpha_2)}}\right) \\ &= -\frac{1}{2}\frac{1}{\sqrt{|\Omega|_{11}}}\exp\left(-\lambda_2 u_1^2-\nu_2 u_1+\eta_2\right)\operatorname{erf}(r_{22}u_1+t_{22}) \end{aligned} \tag{105}$$

where in the last line the coefficients in the argument of the error function reduce to

$$\begin{aligned} r_2 &= -\frac{(|\Omega|_{13}+|\Omega|_{12})}{\sqrt{2\,|\Omega|_{11}(\Omega_{22}+2\Omega_{23}+\Omega_{33})}} = r_1 \equiv r \\ t_2 &= \frac{F\,|\Omega|_{11}-\beta(\Omega_{23}+\Omega_{22})}{\sqrt{2\,|\Omega|_{11}(\Omega_{22}+2\Omega_{23}+\Omega_{33})}}. \end{aligned} \tag{106}$$

The corresponding contribution to the mean value M_m is

$$\begin{aligned} M_{22} &= \frac{1}{\sqrt{2\pi\,|C|}}\int_{-\infty}^{\infty} du_1\; H_{22}(u_1) \\ &= -\frac{1}{2}\frac{\exp(\eta_2)}{\sqrt{|\Omega|_{11}}}\frac{1}{\sqrt{|C|}}\frac{1}{\sqrt{2\pi}}\int_{-\infty}^{\infty}\exp\left(-\lambda_2 u_1^2-\nu_2 u_1\right)\operatorname{erf}(r_2u_1+t_2)\;\; du_1 \\ &= -\frac{1}{2}\frac{\exp(\eta_2)}{\sqrt{|\Omega|_{11}}}\frac{1}{\sqrt{|C|}}\frac{1}{\sqrt{2\lambda_2}}\exp\left(\frac{\nu_2^2}{4\lambda_2}\right)\operatorname{erf}\left(\frac{t_2-r_2\nu_2/(2\lambda_2)}{\sqrt{1+r_2^2/\lambda_2}}\right) \\ &= -M_{21}\operatorname{erf}\left(\frac{t_2-r_2\nu_2/(2\lambda_2)}{\sqrt{1+r_2^2/\lambda_2}}\right). \end{aligned} \tag{107}$$

Combining the four terms (92),(98),(102), and (107) and identifying common coefficients in each of the four expressions, it is found that

$$\begin{aligned} M_m = \frac{1}{2}\exp\left(\frac{\nu^2}{4\lambda}\right)\Bigg[e^{\eta_1}\left(1+\operatorname{erf}\left(\frac{t_1-r\nu/(2\lambda)}{\sqrt{1+r^2/\lambda}}\right)\right) \\ +e^{\eta_2}\left(1-\operatorname{erf}\left(\frac{t_2-r\nu/(2\lambda)}{\sqrt{1+r^2/\lambda}}\right)\right)\Bigg] \end{aligned} \tag{108}$$

where

$$\lambda = \frac{|\Omega|}{2\,|\Omega|_{11}} \qquad \nu = \beta\frac{|\Omega|_{11} + |\Omega|_{12}}{|\Omega|_{11}}$$
$$\eta_1 = \frac{\beta^2}{2}\frac{\Omega_{33}}{|\Omega|_{11}} \qquad \eta_2 = \frac{\beta^2}{2}\frac{\Omega_{22}}{|\Omega|_{11}} - \beta F$$

and

$$\begin{aligned} r &= -\frac{(|\Omega|_{13} + |\Omega|_{12})}{\sqrt{2\,|\Omega|_{11}\,(\Omega_{22} + 2\Omega_{23} + \Omega_{33})}} \\ t_1 &= \frac{F\,|\Omega|_{11} + \beta\,(\Omega_{23} + \Omega_{33})}{\sqrt{2\,|\Omega|_{11}\,(\Omega_{22} + 2\Omega_{23} + \Omega_{33})}} \\ t_2 &= \frac{F\,|\Omega|_{11} + \beta\,(\Omega_{23} + \Omega_{22})}{\sqrt{2\,|\Omega|_{11}\,(\Omega_{22} + 2\Omega_{23} + \Omega_{33})}}. \end{aligned} \tag{109}$$

The form written above for $m > 0$ can also be made to apply when $m = 0$, i.e.,

$$\begin{aligned} M_0 &= \frac{1}{2}\left[1 + \operatorname{erf}\left(\frac{F/\sigma}{\sqrt{2}}\right]\right) + \frac{1}{2}\exp\left(-\beta F\right)\exp\left(\frac{1}{2}\beta^2\sigma^2\right)\left[1 - \operatorname{erf}\left(\frac{F/\sigma - \beta\sigma}{\sqrt{2}}\right)\right] \\ &= \frac{1}{2}\exp\left(\frac{\nu_0^2}{4\lambda_0}\right)\left(e^{\eta_{10}}\left[1 + \operatorname{erf}\left(\frac{t_{10} - r_0\nu_0/\left(2\lambda_0\right)}{\sqrt{1 + r_0^2/\lambda_0}}\right]\right)\right. \\ &\qquad \left. + e^{\eta_{20}}\left[1 - \operatorname{erf}\left(\frac{t_{20} - r_0\nu_0/\left(2\lambda_0\right)}{\sqrt{1 + r_0^2/\lambda_0}}\right]\right)\right) \end{aligned}$$

with the re-definitions

$$\begin{aligned} \lambda_0 &= 1 & \nu_0 &= 0 \\ \eta_{10} &= 0 & \eta_{20} &= \frac{1}{2}\beta^2\sigma^2 - \beta F \\ r_0 &= 0 & & \\ t_{10} &= \frac{F/\sigma}{\sqrt{2}} & t_{20} &= \frac{F/\sigma - \beta\sigma}{\sqrt{2}}. \end{aligned} \tag{110}$$

Thus, the final expression for the mobility can be written in the form

$$\mu = \frac{e\nu_0 a^2}{F} \frac{1}{\langle R \rangle} \exp\left(-\frac{\Sigma^2}{2}\right) = \frac{\mu_0}{F\langle R \rangle}$$

where μ_0 is defined as in (37) for the GDM, and

$$\langle R \rangle = \sum_m e^{-m\beta F} M_m \tag{111}$$

in which M_m is given explicitly in Eq. (108) with the terms given in that expression given by (110) and (109), with the terms in the latter set of quantities expressed in terms of the explicit matrix elements of the matrix Ω given in (63). The individual terms in (111) are therefore straightforward to compute, and the sum is easily performed numerically.

Figure 2.3 shows predictions for the scaled mobility μ/μ_0 of the 1D version of the CGDM, as a function of the square root of the electric field, expressed in terms of the quantity $F/\sigma = eEa/\sigma$, for a system in which the energetic disorder parameter has a value $\sigma = 0.1\,\text{eV}$ which is typical of those measured in MDPs and $\Sigma = 0$.

Curves are shown for different temperatures, ranging from 250K to 325K. The field dependence of the mobility of this one-dimensional version of the CGDM shows reasonable Poole-Frenkel-like behavior (Figure 2.3), but unlike what occurs in real MDPs, the slopes of the approximate lines that characterize the mobility in this model are very insensitive to the temperature. As in the 1D version of the GDM, the mobility decreases exponentially with the square of the magnitude of the geometrical disorder parameter Σ, and therefore exhibits similar scaling behavior (Figure 2.4).

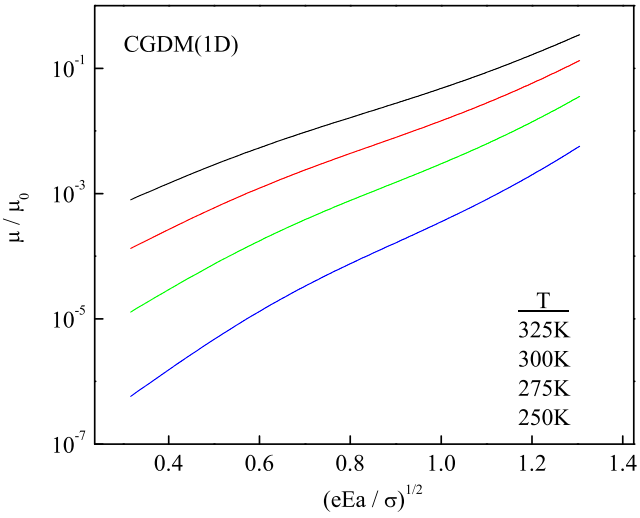

Figure 2.3. Normalized mobility of the CGDM as a function of $\sqrt{eEa/\sigma}$ with $\sigma =$ 0.1 eV and $\Sigma = 0$ for different temperatures as indicated.

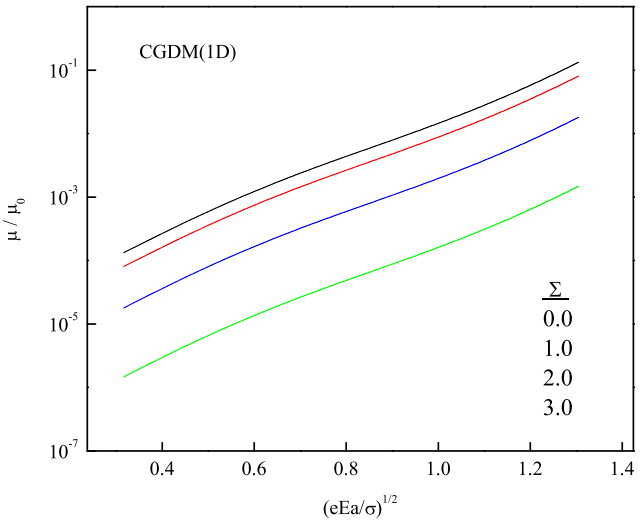

Figure 2.4. Normalized mobility of the CGDM as a function of $\sqrt{eEa/\sigma}$ for different Σ as indicated.

2.3. CALCULATION OF THE MOBILITY FOR THE 1D PCDM-Σ

In the PCDM-Σ, the Gaussian energetic landscape is assumed to be correlated, as described by (5), but the hopping rates are of the small polaron, or Marcus type, as in (7). Including Gaussian geometric disorder as in the last two models, the small polaron hopping rate between nearest neighbors in the presence of a field can be written

$$W_{n,n+1} = \nu_0 e^{-(\Gamma_n+\Gamma_{n+1})} \exp\left(-\frac{\beta}{2}\left(\varepsilon_n - \varepsilon_{n+1} + F\right)\right) \times \exp\left(-\frac{\beta}{8E_B}\left(\left(\varepsilon_n - \varepsilon_{n+1} + F\right)^2\right)\right) \tag{112}$$

$$W_{n+1,n} = \nu_0 e^{-(\Gamma_n+\Gamma_{n+1})} \exp\left(-\frac{\beta}{2}\left(\varepsilon_{n+1} - \varepsilon_n - F\right)\right) \times \exp\left(-\frac{\beta}{8E_B}\left(\left(\varepsilon_{n+1} - \varepsilon_n - F\right)^2\right)\right) \tag{113}$$

where $F = eEa$ is defined as in the last two sections, the fluctuating quantities Γ_n are independently drawn from (20), but where now

$$\nu_0 = \frac{J^2 e^{-2\gamma a}}{\hbar}\sqrt{\frac{\beta\pi}{2E_B}} e^{-\frac{1}{2}\beta E_B} \tag{114}$$

in which $Je^{2\gamma a}$ is the average nearest neighbor transfer integral, E_B the molecular reorganization energy, and β the inverse thermal energy. As it must, this functional form satisfies the detailed balance relation

$$\frac{W_{n,n+1}}{W_{n+1,n}} = \exp\left(-\beta\left(\varepsilon_n - \varepsilon_{n+1} + F\right)\right). \tag{115}$$

Again following Derrida's general development as described by (13)-(14), the average of $r_n^{(0)}$ can be written

$$\langle r_n^{(0)} \rangle = \left\langle \frac{1}{W_{n+1,n}} \right\rangle = \nu_0^{-1} \left\langle e^{\Gamma} \right\rangle^2 e^{-\frac{1}{2}\beta F} M_0 \tag{116}$$

where,

$$M_0 = \left\langle \exp\left(\frac{\beta}{2}\left(\varepsilon_{n+1} - \varepsilon_n\right)\right) \exp\left(\frac{\beta}{8E_B}\left(\varepsilon_{n+1} - \varepsilon_n - F\right)^2\right) \right\rangle \tag{117}$$

depends on two correlated energies while for $m > 0$, the mean value of Eq.(16) can be obtained in a similar but more detailed fashion. By detailed balance the product in parentheses in Eq.(16) can be written as

$$\begin{aligned} \prod_{\ell=0}^{m-1} \frac{W_{n+\ell,n+\ell+1}}{W_{n+\ell+1,n+\ell}} &= \prod_{\ell=0}^{m-1} \exp\left(-\beta\left[\left(\varepsilon_{n+\ell} - \varepsilon_{n+\ell+1} + F\right)\right]\right) \\ &= \exp\left(-\beta \sum_{\ell=0}^{m-1} \left[\left(\varepsilon_{n+\ell} - \varepsilon_{n+\ell+1} + F\right)\right]\right) \\ &= e^{-m\beta F} \exp\left(-\beta\left[\varepsilon_n - \varepsilon_{n+m}\right]\right). \end{aligned}$$

Thus, the mean value of $r_n^{(m)}$ from Eq.(16) can be written as

$$\langle r_n^{(m)} \rangle = \nu_0^{-1} e^{-\left(m+\frac{1}{2}\right)\beta F} M_m \tag{118}$$

where

$$\begin{aligned} M_m = \Bigg\langle \exp\left(-\beta\left[\varepsilon_n - \varepsilon_{n+m}\right]\right) \exp\left(\frac{\beta}{2}\left(\varepsilon_{n+m+1} - \varepsilon_{n+m}\right)\right) \\ \times \exp\left(\frac{\beta}{8E_B}\left(\varepsilon_{n+m+1} - \varepsilon_{n+m} - F\right)^2\right) \Bigg\rangle \end{aligned} \tag{119}$$

depends on three correlated energies, $\varepsilon_n, \varepsilon_{n+m}$, and ε_{n+m+1}.

The calculation begins with M_0 given by Eq.(117). To compute this average, which depends on two correlated energies, a 2×2 covariance matrix $C = C_0$ is defined with elements $C_{ij} = \langle u_i u_j \rangle$ where

$$u_1 = \varepsilon_n, \qquad u_2 = \varepsilon_{n+1}.$$

For dipolar disorder from Eq.(41),

$$\langle \varepsilon_n \varepsilon_{n+m} \rangle = \frac{\sigma^2}{(|m|+1)}$$

so for $m = 0$ the covariance matrix and its inverse are symmetric and the same as (42)

$$C = \frac{1}{2}\sigma^2 \begin{pmatrix} 2 & 1 \\ 1 & 2 \end{pmatrix} \qquad \Omega = \frac{2}{3\sigma^2} \begin{pmatrix} 2 & -1 \\ -1 & 2 \end{pmatrix}$$

and have determinants the same as (43)

$$|C| = \frac{3}{4}\sigma^4 \qquad |\Omega| = \frac{4}{3\sigma^4}.$$

Specifically,

$$\begin{aligned} \Omega_{11} &= \frac{4}{3\sigma^2} \\ \Omega_{12} &= -\frac{2}{3\sigma^2} = \Omega_{21} \\ \Omega_{22} &= \frac{4}{3\sigma^2}. \end{aligned} \tag{120}$$

In terms of these quantities, the joint probability distribution for the correlated Gaussian variables u_1 and u_2 can be expressed as

$$P(u_1,u_2) = \frac{1}{\sqrt{(2\pi)^2\,|C|}} \exp\left(-\frac{1}{2}\left(\Omega_{11}u_1^2 + 2\Omega_{12}u_1u_2 + \Omega_{22}u_2^2\right)\right)$$
$$= \frac{1}{\sqrt{(2\pi)^2\,|C|}} \exp\left(-\frac{2}{3\sigma^2}\left(u_1^2 - u_1u_2 + u_2^2\right)\right). \tag{121}$$

Thus, the mean value (117) of interest for $m = 0$ can be computed as

$$M_0 = \int_{-\infty}^{\infty} du_1 \int_{-\infty}^{\infty} du_2\; P(u_1,u_2) \exp\left(\frac{\beta}{2}(u_2-u_1)\right) \exp\left(\frac{\beta}{8E_B}(u_2-u_1-F)^2\right)$$
$$= \frac{1}{\sqrt{2\pi\,|C|}} \int_{-\infty}^{\infty} du_1\; G(u_1) \tag{122}$$

where

$$G(u_1) = \frac{1}{\sqrt{2\pi}} \int_{-\infty}^{\infty} du_2 \exp\left(-\frac{2}{3\sigma^2}\left(u_1^2 - u_1u_2 + u_2^2\right)\right)$$
$$\times \exp\left(\frac{\beta}{2}(u_2-u_1)\right) \exp\left(\frac{\beta}{8E_B}\left((u_2-u_1-F)^2\right)\right). \tag{123}$$

After some work, the exponentials in this last expression can be combined, and the exponents expanded in powers of u_2. This results in a well known Gaussian integral, allowing $G(u_1)$ to be evaluated in the form

$$G(u_1) = \frac{1}{\sqrt{2\pi}} \int_{-\infty}^{\infty} e^{-\alpha_0 u_2^2 + \gamma_0 u_2 + \delta_0} du_2 = \frac{1}{\sqrt{2\alpha_0}} e^{\delta_0} \exp\left(\frac{\gamma_0^2}{4\alpha_0}\right) \tag{124}$$

in which

$$\alpha_0 = \frac{2}{3\sigma^2} - \frac{\beta}{8E_B} \tag{125}$$

$$\gamma_0 = \frac{\beta}{2}\left(1 - \frac{F}{2E_B}\right) + \left(\frac{2}{3\sigma^2} - \frac{\beta}{4E_B}\right) u_1 = \gamma_{00} + \gamma_{01} u_1 \tag{126}$$

$$\begin{aligned} \delta_0 &= \frac{\beta F^2}{8E_B} - \frac{\beta}{2}\left(1 - \frac{F}{2E_B}\right) u_1 - \left(\frac{2}{3\sigma^2} - \frac{\beta}{8E_B}\right) u_1^2 \\ &= \delta_{00} - \delta_{01} u_1 - \delta_{02} u_1^2 \end{aligned} \tag{127}$$

where

$$\gamma_{00} = \frac{\beta}{2}\left(1 - \frac{F}{2E_B}\right) \tag{128}$$

$$\gamma_{01} = \left(\frac{2}{3\sigma^2} - \frac{\beta}{4E_B}\right) \tag{129}$$

$$\tag{130}$$

and

$$\delta_{00} = \frac{\beta F^2}{8E_B} \tag{131}$$

$$\delta_{01} = \frac{\beta}{2}\left(1 - \frac{F}{2E_B}\right) \tag{132}$$

$$\delta_{02} = \left(\frac{2}{3\sigma^2} - \frac{\beta}{8E_B}\right). \tag{133}$$

Substituting these definitions into (124) the expression for $G(u_1)$ can be written as

$$G(u_1) \ = \frac{1}{\sqrt{2\alpha_0}} e^{-\alpha_1 u_1^2 - \gamma_1 u_1 + \delta 1} \tag{134}$$

where

$$\alpha_1 = \delta_{02} - \frac{1}{4\alpha_0}\gamma_{01}^2 \tag{135}$$

$$\gamma_1 = \delta_{01} - \frac{1}{2\alpha_0}\gamma_{00}\gamma_{01} \tag{136}$$

$$\delta_1 = \delta_{00} + \frac{1}{4\alpha_0}\gamma_{00}^2. \tag{137}$$

Thus, the integral in (122) also reduces to a Gaussian integral

$$M_0 = \frac{1}{\sqrt{2\pi\,|C|}} \int_{-\infty}^{\infty} du_1\; G\left(u_1\right) = \frac{1}{\sqrt{2\pi\,|C|}} \frac{1}{\sqrt{2\alpha_0}} \int_{-\infty}^{\infty} du_1\; e^{-\alpha_1 u_1^2 - \gamma_1 u_1 + \delta_0} \tag{138}$$

which can be evaluated as

$$M_0 = \frac{e^{\delta_1}}{\sqrt{4\alpha_0\alpha_1\,|C|}} \exp\left(\frac{\gamma_1^2}{4\alpha_1}\right) \tag{139}$$

with the various terms appearing in that expression given explicitly by (43),(125), (135)-(137), and (128)-(133).

To now calculate M_m given by Eq.(119), $C = C_m$ is re-defined as a 3×3 covariance matrix C with elements

$$C_{ij} = \langle u_i u_j \rangle$$

where now it is to be understood that for $m > 0$

$$u_1 = \varepsilon_n,$$

$$u_2 = \varepsilon_{n+m}$$

$$u_3 = \varepsilon_{n+m+1}$$

in terms of which (119) can be written as

$$M_m = \left\langle \exp\left(-\beta\left(u_1 - u_2\right)\right) \exp\left(\frac{\beta}{2}\left(u_3 - u_2\right) + \frac{\beta}{8E_B}\left(u_3 - u_2 - F\right)^2\right)\right\rangle$$
$$= \left\langle \exp\left(\frac{\beta}{2}\left(u_2 - 2u_1 + u_3\right) + \frac{\beta}{8E_B}\left(u_3 - u_2 - F\right)^2\right)\right\rangle. \quad (140)$$

For dipolar disorder described by (41), the covariance matrix takes the symmetric form

$$C = \sigma^2 \begin{pmatrix} 1 & \frac{1}{m+1} & \frac{1}{m+2} \\ \frac{1}{m+1} & 1 & \frac{1}{2} \\ \frac{1}{m+2} & \frac{1}{2} & 1 \end{pmatrix},$$

the inverse of which is same as (63)

$$\Omega = C^{-1} = \kappa \begin{pmatrix} \frac{3\left(m+2\right)\left(m+1\right)}{2m\left(m+3\right)} & -\frac{1}{m} & -\frac{1}{\left(m+3\right)} \\ -\frac{1}{m} & \frac{2\left(m+1\right)^2}{m\left(m+2\right)} & -1 \\ -\frac{1}{\left(m+3\right)} & -1 & \frac{2\left(m+2\right)^2}{\left(m+3\right)\left(m+1\right)} \end{pmatrix}$$

where

$$\kappa = \frac{2\left(m+1\right)\left(m+2\right)}{\left(3m^2+9m+8\right)}\frac{1}{\sigma^2}.$$

The determinant of covariant matrix (65) is

$$|C| = \frac{m\left(m+3\right)\left(3m^2+9m+8\right)}{4\left(m+1\right)^2\left(m+2\right)^2}\sigma^6.$$

In the analysis that follows, the matrix elements, the determinant, and certain minors or cofactors of the matrix Ω appear. Since the matrix Ω is symmetric,

$$\begin{aligned}|\Omega| = |C|^{-1} &= \Omega_{11}\Omega_{22}\Omega_{33} - \Omega_{33}\Omega_{12}^2 + 2\Omega_{12}\Omega_{13}\Omega_{23} - \Omega_{22}\Omega_{13}^2 - \Omega_{11}\Omega_{23}^2 \\ &= \frac{4\left(m+1\right)^2\left(m+2\right)^2}{m\left(m+3\right)\left(3m^2+9m+8\right)}\sigma^{-6}.\end{aligned}$$

The joint probability distribution for the 3 correlated Gaussian variables u_1, u_2, and u_3 can then be written

$$\begin{aligned}P\left(u_1,u_2,u_3\right) &= \frac{1}{\sqrt{\left(2\pi\right)^3|C|}}\exp\left(-\frac{1}{2}\sum_{\alpha=1}^{3}\sum_{\beta=1}^{3}u_\alpha\Omega_{\alpha\beta}u_\beta\right) \\ &= \frac{1}{\sqrt{\left(2\pi\right)^3|C|}}P_{12}\left(u_1,u_2\right)P_3\left(u_1,u_2,u_3\right) \qquad (141)\end{aligned}$$

where the part

$$P_{12}\left(u_1,u_2\right) = \exp\left(-\frac{1}{2}\left(u_1^2\Omega_{11} + 2u_1\Omega_{12}u_2 + \frac{1}{2}u_2^2\Omega_{22}\right)\right)$$

that depends only on u_1 and u_2 have been separated out from the parts

$$P_3\left(u_1,u_2,u_3\right) = \exp\left(-\frac{1}{2}\left(u_3^2\Omega_{33} + 2\left(\Omega_{13}u_1 + \Omega_{23}u_2\right)u_3\right)\right)$$

that have a dependence on u_3. In terms of this probability distribution, the average (140) is

$$\begin{aligned}M_m = \int_{-\infty}^{\infty}du_1\int_{-\infty}^{\infty}du_2\int_{-\infty}^{\infty}du_3\; P\left(u_1,u_2,u_3\right)\exp\left(\frac{\beta}{2}\left(u_2-2u_1+u_3\right)\right) \\ \times\exp\left(\frac{\beta}{8E_B}\left(u_3-u_2-F\right)^2\right) \qquad (142)\end{aligned}$$

which can be written as

$$M_m = \frac{1}{\sqrt{(2\pi)^2 |C|}} \int_{-\infty}^{\infty} du_1 \int_{-\infty}^{\infty} du_2 \; F(u_1, u_2)\, G(u_1, u_2) \tag{143}$$

in which

$$\begin{aligned} F(u_1, u_2) &= P_{12}(u_1, u_2) \exp\left(\frac{\beta}{2}(u_2 - 2u_1)\right) \exp\left(\left(\frac{\beta}{8E_B}(u_2 + F)^2\right)\right) \\ &= \exp\left(-\frac{1}{2}\left(u_1^2\Omega_{11} + 2u_1\Omega_{12}u_2 + \frac{1}{2}u_2^2\Omega_{22}\right)\right) \exp\left(\frac{\beta}{2}(u_2 - 2u_1)\right) \\ &\qquad \times \exp\left(\frac{\beta}{8E_B}(u_2 + F)^2\right) \end{aligned} \tag{144}$$

and in which was redefined the quantity

$$\begin{aligned} G(u_1, u_2) &= \frac{1}{\sqrt{2\pi}} \int_{-\infty}^{\infty} du_3 \; P_3(u_1, u_2, u_3) \\ &\qquad \times \exp\left(\left(\frac{\beta}{2} - \frac{\beta}{8E_B}(2F + 2u_2)\right) u_3 + \frac{\beta}{8E_B}u_3^2\right) \\ &= \frac{1}{\sqrt{2\pi}} \int_{-\infty}^{\infty} du_3 \; \exp\left(-\frac{1}{2}\left(u_3^2\Omega_{33} + 2(\Omega_{13}u_1 + \Omega_{23}u_2)\, u_3\right)\right) \\ &\qquad \times \exp\left(\left(\frac{\beta}{2} - \frac{\beta}{8E_B}(2F + 2u_2)\right) u_3 + \frac{\beta}{8E_B}u_3^2\right). \end{aligned} \tag{145}$$

Combining the exponents and expanding in powers of u_3 this last function can be evaluated in the form

$$G(u_1, u_2) = \frac{1}{\sqrt{2\pi}} \int_{-\infty}^{\infty} du_3 \; e^{-\alpha_2 u_3^2 - \gamma_2 u_3} = \frac{1}{\sqrt{2\alpha_2}} \exp\left(\frac{\gamma_2^2}{4\alpha_2}\right) \tag{146}$$

in which

$$\alpha_2 = \frac{1}{2}\left(\Omega_{33} - \frac{\beta}{4E_B}\right) \tag{147}$$

$$\gamma_2 = \left(\Omega_{13}u_1 + \Omega_{23}u_2 - \frac{\beta}{2} + \frac{\beta}{4E_B}\left(F + u_2\right)\right). \tag{148}$$

Combining (146) and (144) into the product $F\left(u_1, u_2\right) G\left(u_1, u_2\right)$, combining the exponentials, and expanding in powers of u_2, the integral

$$\begin{aligned} H\left(u_1\right) &= \frac{1}{\sqrt{2\pi}} \int_{-\infty}^{\infty} du_2 \; F\left(u_1, u_2\right) G\left(u_1, u_2\right) \\ &= \frac{1}{\sqrt{2\alpha_2}} \frac{1}{\sqrt{2\pi}} \int_{-\infty}^{\infty} du_2 \; e^{-\alpha_3 u_2^2 + \gamma_3 u_2 + \delta_3} \\ &= \frac{1}{\sqrt{2\alpha_2}} \frac{1}{\sqrt{2\alpha_3}} e^{\delta_3} \exp\left(\frac{\gamma_3^2}{4\alpha_3}\right), \end{aligned} \tag{149}$$

is introduced in which

$$\alpha_3 = -\left(\frac{1}{4\alpha_2}\left(\Omega_{23} + \frac{\beta}{4E_B}\right)^2 - \frac{1}{4}\Omega_{22} + \frac{\beta}{8E_B}\right) \tag{150}$$

$$\gamma_3 = \gamma_{30} - \gamma_{31}u_1 \tag{151}$$

$$\delta_3 = \delta_{30} - \delta_{31}u_1 - \delta_{32}u_1^2 \tag{152}$$

where

$$\gamma_{30} = \frac{\beta}{2}\left(1 + \frac{F}{2E_B}\right) - \frac{\beta}{4\alpha_2}\left(\Omega_{23} + \frac{\beta}{4E_B}\right)\left(1 - \frac{F}{2E_B}\right) \tag{153}$$

$$\gamma_{31} = \Omega_{12} - \frac{1}{2\alpha_2}\Omega_{13}\left(\Omega_{23} + \frac{\beta}{4E_B}\right) \tag{154}$$

$$\delta_{30} = \left(\frac{\beta^2}{16\alpha_2}\left(1 - \frac{F}{2E_B}\right)^2 + \frac{\beta F^2}{8E_B}\right) \tag{155}$$

$$\delta_{31} = \beta + \frac{\beta}{4\alpha_2}\Omega_{13}\left(1 - \frac{F}{2E_B}\right) \tag{156}$$

$$\delta_{32} = \frac{1}{2}\left(\Omega_{11} - \frac{1}{2\alpha_2}\Omega_{13}^2\right). \tag{157}$$

Thus, the integral (143) can be evaluated as

$$\begin{aligned} M_m &= \frac{1}{\sqrt{2\pi\,|C|}} \int_{-\infty}^{\infty} du_1\; H(u_1) \\ &= \frac{1}{\sqrt{2\pi\,|C|}} \frac{1}{\sqrt{2\alpha_2}} \frac{1}{\sqrt{2\alpha_3}} \int_{-\infty}^{\infty} du_1\; e^{-\alpha_4 u_1^2 - \gamma_4 u_1 + \delta_4} \end{aligned} \tag{158}$$

where

$$\alpha_4 = \delta_{32} - \frac{1}{4\alpha_3}\gamma_{31}^2 \tag{159}$$

$$\gamma_4 = \delta_{31} + \frac{1}{2\alpha_3}\gamma_{30}\gamma_{31} \tag{160}$$

$$\delta_4 = \delta_{30} + \frac{1}{4\alpha_3}\gamma_{30}^2. \tag{161}$$

Evaluating this last Gaussian integral, it is found that

$$M_m = \frac{e^{\delta_4}}{\sqrt{8\alpha_2\alpha_3\alpha_4\,|C|}} \exp\left(\frac{\gamma_4^2}{4\alpha_4}\right) \tag{162}$$

where the different quantities appearing in these expressions are given as follows: α_2 appears explicitly in (147), α_3 is given explicitly in (150), α_4 is given in (159), in

terms of quantities defined in (150),(154), and (157), γ_4 is given in (160) in terms of quantites defined in (150),(153), and (154), δ_4 is given in (161), in terms of quantities defined in (150),(153), and (155).

With these results $\langle r \rangle$ can then be computed as

$$\langle r \rangle = \sum_{m=0}^{\infty} \langle r_n^{(m)} \rangle = \nu_0^{-1} \langle e^{\Gamma} \rangle^2 \langle R \rangle \tag{163}$$

where

$$\langle R \rangle = \sum_{m=0}^{\infty} e^{-\left(m+\frac{1}{2}\right)\beta F} M_m \tag{164}$$

with M_m given by (139) for $m = 0$, and by (162) for $m > 0$, where the quantities appearing in those expressions are given after each of the respective equations. In terms of this sum, which is straightforwardly computed from the given definitions above the mobility is found in the form

$$\mu = \frac{e\nu_0 a^2}{F} \frac{1}{\langle R \rangle} \exp\left(-\frac{\Sigma^2}{2}\right) = \frac{\mu_0 \mu_1}{F \langle R \rangle}$$

where

$$\mu_0 = \frac{J^2 e^{-2\gamma a}}{\hbar} \sqrt{\frac{\pi}{2E_B}} \exp\left(-\frac{\Sigma^2}{2}\right)$$

is field and temperature independent and

$$\mu_1 = \sqrt{\beta} e^{-\frac{1}{2}\beta E_B}.$$

Figure 2.5 shows predictions for the scaled mobility μ/μ_0 of this 1D version of the PCDM, as a function of the square root of the electric field, expressed in terms of the quantity $F/\sigma = eEa/\sigma$, for a system in which the energetic disorder parameter

has a value $\sigma = 0.1\,\text{eV}$, which is typical of those measured in MDPs. Curves are shown for several different temperatures, ranging from 250K to 325K.

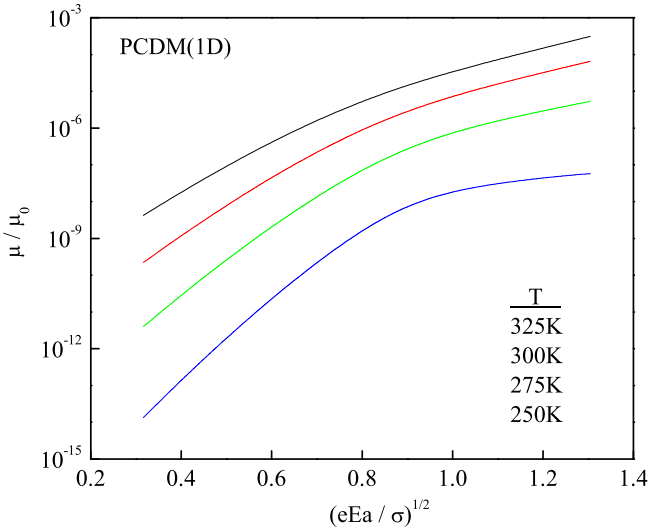

Figure 2.5. Normalized mobility of the PCDM as a function of $\sqrt{eEa/\sigma}$ with $E_B = 0.3$ eV, $\sigma = 0.1$ eV and $\Sigma = 0$ for different temperatures as indicated.

The field dependence of the mobility of this one-dimensional version of the PCDM shows reasonable Poole-Frenkel-like behavior at low fields, but exhibits a turnover at higher fields due to the functional form of the small polaron hopping rates. As in the 1D version of the GDM and CGDM, the mobility decreases exponentially with the square of the magnitude of the geometrical disorder parameter Σ, and therefore exhibits similar scaling behavior (Figure 2.6).

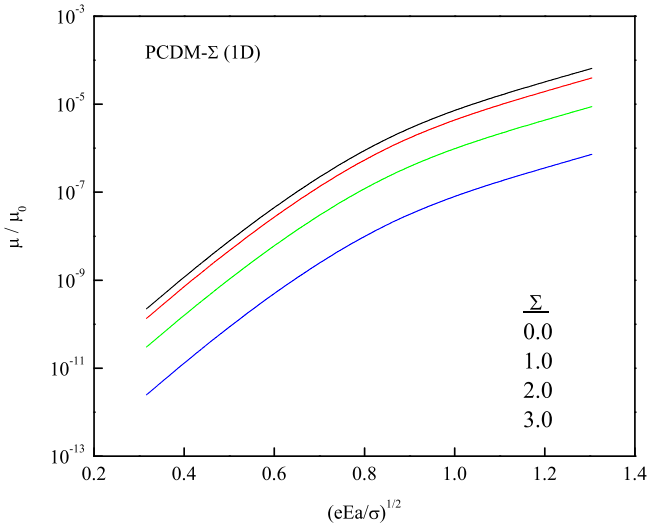

Figure 2.6. Normalized mobility of the PCDM as a function of $\sqrt{eEa/\sigma}$ with $\sigma =$ 0.1eV and T=300K for different Σ.

2.4. CALCULATION OF THE MOBILITY FOR THE 1D PGDM

As a final example, the 1D version of the uncorrelated polaron disorder model is considered. In the PGDM, hopping occurs via small polaron, or Marcus hopping rates (7) through an uncorrelated Gaussian distribution of site energies. The small polaron hopping rate between nearest neighbors in the presence of a field is as given in (112) and (113) for the PCDM, where the quantities appearing in those equations are as defined immediately thereafter. Again one is interested in the quantities

$$\langle r_n^{(m)} \rangle = \langle \frac{1}{W_{n+1,n}} \rangle = \nu_0^{-1} e^{-\left(m+\frac{1}{2}\right)\beta F} M_m \tag{165}$$

which are formally the same as in the corresponding expressions (117) and (119) as for the PCDM. The difference is that the energies appearing in those expressions are

uncorrelated. Thus the calculation focuses first on

$$M_0 = \left\langle \exp\left(\frac{\beta}{2}\left(\varepsilon_{n+1} - \varepsilon_n\right)\right) \exp\left(\frac{\beta}{8E_B}\left(\varepsilon_{n+1} - \varepsilon_n - F\right)^2\right)\right\rangle \tag{166}$$

in which two uncorrelated energies,

$$u_1 = \varepsilon_n, \qquad u_2 = \varepsilon_{n+1}$$

are introduced. The joint probability distribution for the uncorrelated Gaussian variables u_1 and u_2 can be expressed as

$$P\left(u_1, u_2\right) = \frac{1}{2\pi\sigma^2} \exp\left(-\frac{u_1^2}{2\sigma^2}\right) \exp\left(-\frac{u_2^2}{2\sigma^2}\right). \tag{167}$$

Thus, the mean value (117) of interest for $m = 0$ can be computed as

$$\begin{aligned} M_0 &= \int_{-\infty}^{\infty} du_1 \int_{-\infty}^{\infty} du_2 \; P\left(u_1, u_2\right) \exp\left(\frac{\beta}{2}\left(u_2 - u_1\right)\right) \exp\left(\frac{\beta}{8E_B}\left(u_2 - u_1 - F\right)^2\right) \\ &= \frac{1}{\sqrt{2\pi\sigma^2}} \int_{-\infty}^{\infty} du_1 \; G\left(u_1\right) \end{aligned} \tag{168}$$

where

$$\begin{aligned} G\left(u_1\right) = \frac{1}{\sqrt{2\pi\sigma^2}} \int_{-\infty}^{\infty} du_2 \exp\left(-\frac{u_1^2}{2\sigma^2}\right) \exp\left(-\frac{u_2^2}{2\sigma^2}\right) \exp\left(\frac{\beta}{2}\left(u_2 - u_1\right)\right) \\ \times \exp\left(\frac{\beta}{8E_B}\left(\left(u_2 - u_1 - F\right)^2\right)\right). \end{aligned} \tag{169}$$

After some work, the exponentials in this last expression can be combined, and the exponents expanded in powers of u_2. This results in a well known Gaussian

integral, allowing an evaluation $G(u_1)$ in the form

$$G(u_1) = \frac{1}{\sqrt{2\pi\sigma^2}} \int_{-\infty}^{\infty} e^{-\alpha_0 u_2^2 + \gamma_0 u_2 + \delta_0} du_2 = \frac{1}{\sqrt{2\alpha_0\sigma^2}} e^{\delta_0} \exp\left(\frac{\gamma_0^2}{4\alpha_0}\right) \tag{170}$$

in which

$$\alpha_0 = \frac{1}{2\sigma^2} - \frac{\beta}{8E_B} \tag{171}$$

$$\gamma_0 = \frac{\beta}{2}\left(1 - \frac{F}{2E_B}\right) - \frac{\beta}{4E_B} u_1 = \gamma_{00} - \gamma_{01} u_1 \tag{172}$$

$$\begin{aligned} \delta_0 &= \frac{1}{8}\frac{\beta}{E_B}(F + u_1)^2 - \frac{1}{2}\beta u_1 - \frac{1}{2\sigma^2} u_1^2 \\ &= \frac{\beta F^2}{8E_B} - \frac{\beta}{2}\left(1 - \frac{F}{2E_B}\right) u_1 + \left(\frac{\beta}{8E_B} - \frac{1}{2\sigma^2}\right) u_1^2 \\ &= \delta_{00} - \delta_{01} u_1 + \delta_{02} u_1^2 \end{aligned} \tag{173}$$

where

$$\gamma_{00} = \frac{\beta}{2}\left(1 - \frac{F}{2E_B}\right) \tag{174}$$

$$\gamma_{01} = \frac{\beta}{4E_B} \tag{175}$$

$$\delta_{00} = \frac{\beta F^2}{8E_B} \tag{176}$$

$$\delta_{01} = \frac{\beta}{2}\left(1 - \frac{F}{2E_B}\right) \tag{177}$$

$$\delta_{02} = \frac{\beta}{8E_B} - \frac{1}{2\sigma^2}. \tag{178}$$

Substituting these definitions into (170) the expression for $G(u_1)$ can be written as

$$G(u_1) = \frac{1}{\sqrt{2\alpha_0\sigma^2}} e^{-\alpha_1 u_1^2 - \gamma_1 u_1 + \delta_1}$$

where

$$\alpha_1 = -\delta_{02} - \frac{1}{4\alpha_0}\gamma_{01}^2 \tag{179}$$

$$\gamma_1 = \delta_{01} + \frac{1}{2\alpha_0}\gamma_{00}\gamma_{01} \tag{180}$$

$$\delta_1 = \delta_{00} + \frac{1}{4\alpha_0}\gamma_{00}^2. \tag{181}$$

Thus, the integral in (168) also reduces to a Gaussian integral and it is found that

$$M_0 = \frac{1}{\sqrt{2\pi\sigma^2}} \int_{-\infty}^{\infty} du_1 \; G(u_1) = \frac{1}{\sqrt{2\pi\sigma^2}} \frac{1}{\sqrt{2\alpha_0\sigma^2}} \int_{-\infty}^{\infty} du_1 \; e^{-\alpha_1 u_1^2 - \gamma_1 u_1 + \delta_1} \tag{182}$$

which can be evaluated as

$$M_0 = \frac{e^{\delta_1}}{\sqrt{4\alpha_0\alpha_1\sigma^4}} \exp\left(\frac{\gamma_1^2}{4\alpha_1}\right) \tag{183}$$

with the various terms appearing in that expression given explicitly by (179)-(181), which are themselves given in terms of (171), and (174)-(178).

For $m > 0$, the mean value (119) can be re-written

$$\begin{aligned} M_m &= \left\langle \exp\left(-\beta\left[\varepsilon_n - \varepsilon_{n+m}\right]\right) \exp\left(\frac{\beta}{2}\left(\varepsilon_{n+m+1} - \varepsilon_{n+m}\right)\right) \right. \\ &\qquad \left. \exp\left(\frac{\beta}{8E_B}\left(\left(\varepsilon_{n+m+1} - \varepsilon_{n+m} - F\right)^2\right)\right) \right\rangle \\ &= \left\langle \exp\left(-\beta\varepsilon_n\right)\right\rangle \left\langle \exp\left(\frac{\beta}{2}\left(\varepsilon_{n+m} + \varepsilon_{n+m+1}\right)\right) \right. \\ &\qquad \left. \exp\left(\frac{\beta}{8E_B}\left(\left(\varepsilon_{n+m+1} - \varepsilon_{n+m} - F\right)^2\right)\right) \right\rangle \end{aligned} \tag{184}$$

and depends on three uncorrelated energies, $\varepsilon_n, \varepsilon_{n+m}$, and ε_{n+m+1}. Introducing

$$u_1 = \varepsilon_n,$$

$$u_2 = \varepsilon_{n+m}$$

$$u_3 = \varepsilon_{n+m+1},$$

Eq.(119) can be re-written as

$$M_m = \langle \exp(-\beta u_1) \rangle \left\langle \exp\left(\frac{\beta}{2}(u_2 + u_3) + \frac{\beta}{8E_B}(u_3 - u_2 - F)^2 \right) \right\rangle. \tag{185}$$

The joint probability distribution for the 3 uncorrelated Gaussian variables u_1, u_2, and u_3 can then be written

$$P(u_1, u_2, u_3) = \frac{1}{\sqrt{(2\pi\sigma^2)^3}}\, e^{-u_1^2/(2\sigma^2)}\, e^{-u_2^2/(2\sigma^2)}\, e^{-u_3^2/(2\sigma^2)}. \tag{186}$$

In terms of this probability distribution, the average (185) is

$$M_m = \int_{-\infty}^{\infty} du_1 \int_{-\infty}^{\infty} du_2 \int_{-\infty}^{\infty} du_3\; P(u_1, u_2, u_3) \exp(-\beta u_1) \exp\left(\frac{\beta}{2}(u_2 + u_3) + \frac{\beta}{8E_B}(u_3 - u_2 - F)^2 \right) \tag{187}$$

Now, the first factor in $M_m = H_1 H_{23}$ is readily computed as

$$H_1 = \langle \exp(-\beta \varepsilon_n) \rangle = \frac{1}{\sqrt{2\pi\sigma^2}} \int_{-\infty}^{\infty} e^{-\beta u_1} e^{-u_1^2/(2\sigma^2)} du = e^{\frac{1}{2}\beta^2\sigma^2} \tag{188}$$

while

$$H_{23} = \left\langle \exp\left(\frac{\beta}{2}(u_2+u_3) + \frac{\beta}{8E_B}(u_3-u_2-F)^2\right)\right\rangle$$
$$= \frac{1}{\sqrt{(2\pi\sigma^2)^2}} \int_{-\infty}^{\infty} du_2 \int_{-\infty}^{\infty} du_3 \; e^{-u_3^2/(2\sigma^2)}$$
$$\times \exp\left(\frac{\beta}{2}(u_2+u_3) + \frac{\beta}{8E_B}(u_3-u_2-F)^2\right)$$
$$= \frac{1}{\sqrt{2\pi\sigma^2}} \int_{-\infty}^{\infty} du_2 G(u_2) \tag{189}$$

in which

$$G(u_2) = \frac{1}{\sqrt{2\pi\sigma^2}} \int_{-\infty}^{\infty} du_3 \; e^{-u_2^2/(2\sigma^2)} e^{-u_3^2/(2\sigma^2)}$$
$$\times \exp\left(\frac{\beta}{2}(u_2+u_3) + \frac{\beta}{8E_B}(u_3-u_2-F)^2\right). \tag{190}$$

Combining the exponents in (191) and expanding in powers of u_3 this last function can be evaluated in the form

$$G(u_2) = \frac{1}{\sqrt{2\pi\sigma^2}} \int_{-\infty}^{\infty} du_3 \; e^{-\alpha_2 u_3^2 + \gamma_2 u_3 + \delta_2} = \frac{1}{\sqrt{2\alpha_2\sigma^2}} e^{\delta_2} \exp\left(\frac{\gamma_2^2}{4\alpha_2}\right) \tag{191}$$

in which

$$\alpha_2 = \left(\frac{1}{2\sigma^2} - \frac{\beta}{8E_B}\right) = \alpha_0 \tag{192}$$
$$\gamma_2 = \frac{\beta}{2}\left(1 - \frac{F}{2E_B}\right) - \frac{\beta}{4E_B}u_2 = \gamma_{20} - \gamma_{21}u_2 \tag{193}$$
$$\delta_2 = \frac{\beta F^2}{8E_B} + \frac{\beta}{2}\left(1 + \frac{F}{2E_B}\right)u_2 + \left(\frac{\beta}{8E_B} - \frac{1}{2\sigma^2}\right)u_2^2$$
$$= \delta_{20} + \delta_{21}u_2 + \delta_{22}u_2^2 \tag{194}$$

where

$$\gamma_{20} = \frac{\beta}{2}\left(1 - \frac{F}{2E_B}\right) = \gamma_{00} \tag{195}$$

$$\gamma_{21} = \frac{\beta}{4E_B} = -\gamma_{01} \tag{196}$$

$$\delta_{20} = \frac{\beta F^2}{8E_B} = \delta_{00} \tag{197}$$

$$\delta_{21} = \frac{\beta}{2}\left(1 + \frac{F}{2E_B}\right) \tag{198}$$

$$\delta_{22} = \left(\frac{\beta}{8E_B} - \frac{1}{2\sigma^2}\right) = \delta_{02}. \tag{199}$$

Combining the exponentials in the right-hand side of (191) and expanding in powers of u_2 the integral (200) can be written

$$H_{23} = \frac{1}{\sqrt{2\pi\sigma^2}}\frac{1}{\sqrt{2\alpha_2\sigma^2}}\int_{-\infty}^{\infty} du_2 \quad \exp\left(\delta_2 + \frac{\gamma_2^2}{4\alpha_2}\right)$$

$$H_{23} = \frac{1}{\sqrt{2\pi\sigma^2}}\frac{1}{\sqrt{2\alpha_2\sigma^2}}\int_{-\infty}^{\infty} du_2 \; e^{-\alpha_3 u_2^2 + \gamma_3 u_2 + \delta_3} = \frac{1}{\sqrt{4\alpha_2\alpha_3\sigma^4}} e^{\delta_3} \exp\left(\frac{\gamma_3^2}{4\alpha_3}\right) \tag{200}$$

where

$$\alpha_3 = -\delta_{22} - \frac{1}{4\alpha_2}\gamma_{21}^2 \tag{201}$$

$$\gamma_3 = \delta_{21} - \frac{1}{2\alpha_2}\gamma_{20}\gamma_{21} \tag{202}$$

$$\delta_3 = \delta_{20} + \frac{1}{4\alpha_2}\gamma_{20}^2. \tag{203}$$

Thus, from (188) and (200),

$$M_m = H_1 H_{23} = \frac{e^{\frac{1}{2}\beta^2\sigma^2 + \delta_3}}{\sqrt{4\alpha_2\alpha_3\sigma^4}} \exp\left(\frac{\gamma_3^2}{4\alpha_3}\right) \tag{204}$$

$$= \frac{e^{\frac{1}{2}\beta^2\sigma^2} e^{\delta_3}}{\sqrt{4\alpha_2\alpha_3\sigma^4}} \exp\left(\frac{\gamma_3^2}{4\alpha_3}\right)$$

where the different quantities appearing in these expressions are given as follows: α_2 appears explicitly in (192), α_3 is given explicitly in (201), in terms of quantities defined in (192),(196), and (199), γ_3 is given in (202) in terms of quantites defined in (192),(195), and (196), δ_3 is given in (203), in terms of quantities defined in (192),(195), and (197).

Comparing M_0 and M_m it is clear that they are of similar form,

$$M_0 = \frac{e^{\delta_1}}{\sqrt{4\alpha_0\alpha_1\sigma^4}} \exp\left(\frac{\gamma_1^2}{4\alpha_1}\right)$$

$$M_m = \frac{e^{\frac{1}{2}\beta^2\sigma^2}e^{\delta_3}}{\sqrt{4\alpha_0\alpha_3\sigma^4}} \exp\left(\frac{\gamma_3^2}{4\alpha_3}\right)$$

but involve different parameters. The average of $r_n^{(0)}$ can be written

$$\begin{aligned}\langle r_n^{(0)}\rangle &= \nu_0^{-1}e^{-\frac{1}{2}\beta F}M_0 \\ &= \nu_0^{-1}e^{-\frac{1}{2}\beta F}\frac{e^{\delta_1}}{\sqrt{4\alpha_0\alpha_1\sigma^4}} \exp\left(\frac{\gamma_1^2}{4\alpha_1}\right) \qquad (205)\end{aligned}$$

while for $m > 0$,

$$\begin{aligned}\langle r_n^{(m)}\rangle &= \nu_0^{-1}e^{-\left(m+\frac{1}{2}\right)\beta F}M_m \qquad (206) \\ &= \nu_0^{-1}e^{-\left(m+\frac{1}{2}\right)\beta F}\frac{e^{\frac{1}{2}\beta^2\sigma^2}e^{\delta_3}}{\sqrt{4\alpha_0\alpha_3\sigma^4}} \exp\left(\frac{\gamma_3^2}{4\alpha_3}\right). \qquad (207)\end{aligned}$$

With these results it is found that

$$\langle r\rangle = \sum_{m=0}^{\infty}\langle r_n^{(m)}\rangle = \nu_0^{-1}\langle e^{\Gamma}\rangle^2\langle R\rangle$$

where

$$\langle R\rangle = e^{-\frac{1}{2}\beta F}\frac{e^{\delta_1}}{\sqrt{4\alpha_0\alpha_1\sigma^4}}\exp\left(\frac{\gamma_1^2}{4\alpha_1}\right) + \frac{e^{\frac{1}{2}\beta^2\sigma^2}e^{\delta_1}}{\sqrt{4\alpha_0\alpha_1\sigma^4}}\exp\left(\frac{\gamma_3^2}{4\alpha_1}\right)\sum_{m=1}^{\infty}e^{-\left(m+\frac{1}{2}\right)\beta F} \tag{208}$$

which reduces to

$$\langle R\rangle = \frac{e^{-\frac{1}{2}\beta F}}{\sqrt{4\alpha_0\sigma^4}}\left(\frac{e^{\delta_1}}{\sqrt{\alpha_1}}\exp\left(\frac{\gamma_1^2}{4\alpha_1}\right) + \frac{e^{-\beta F}}{1-e^{-\beta F}}\frac{e^{\delta_3}}{\sqrt{\alpha_3}}\exp\left(\frac{\gamma_3^2}{4\alpha_3}\right)\right) \tag{209}$$

in which the parameters appearing in this expression can be located as described following Eqs.(183) and (204). Thus for the PGDM the mobility can be written as

$$\mu = \frac{e\nu_0 a^2}{F}\frac{1}{\langle R\rangle}\exp\left(-\frac{\Sigma^2}{2}\right) = \frac{\mu_0\mu_1}{F\langle R\rangle}$$

where

$$\mu_0 = \frac{J^2e^{-2\gamma a}}{\hbar}\sqrt{\frac{\pi}{2E_B}}\exp\left(-\frac{\Sigma^2}{2}\right)$$

is field and temperature independent and

$$\mu_1 = \sqrt{\beta}e^{-\frac{1}{2}\beta E_B}.$$

Figure 2.7 shows predictions for the scaled mobility μ/μ_0 of this 1D version of the PGDM, as a function of the square rootof the electric field, expressed in terms of the quantity $F/\sigma = eEa/\sigma$, for a system in which the energetic disorder parameter has a value $\sigma = 0.1\,\text{eV}$ and $E_B = 0.3\,\text{eV}$, which is typical of those measured in MDPs. Curves are shown for several different temperatures, ranging from 250 K to 325 K. The field dependence of the mobility of this one-dimensional version of the PCDM

shows curvature similar to that seen in the 1D GDM calculations (Figure 2.1). The data displays Poole-Frenkel type behavior for higher fields, but flattens at lower fields. Qualitatively, the main difference between the 1D versions of the GDM and the PGDM calculations are that, for the GDM curves for different temperatures are almost parallel, while the curves for the PGDM for different temperatures (Figure 2.7) seem to converge towards a certain fixed point at high field.

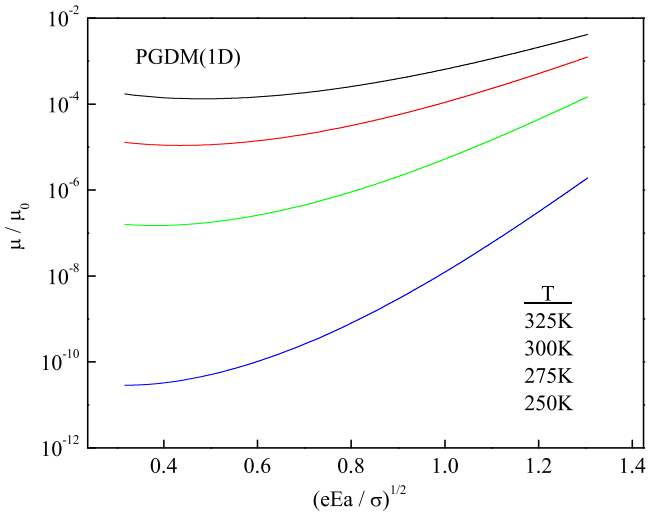

Figure 2.7. Normalized mobility of the PGDM as a function of $\sqrt{eEa/\sigma}$ with $E_B = 0.3\,\mathrm{eV}$, $\sigma = 0.1\,\mathrm{eV}$ and $\Sigma = 0$ for different temperatures as indicated.

As in the 1D version of the previous models, the mobility decreases exponentially with the square of the magnitude of the geometrical disorder parameter Σ, and therefore exhibits similar scaling behavior (Figure 2.8).

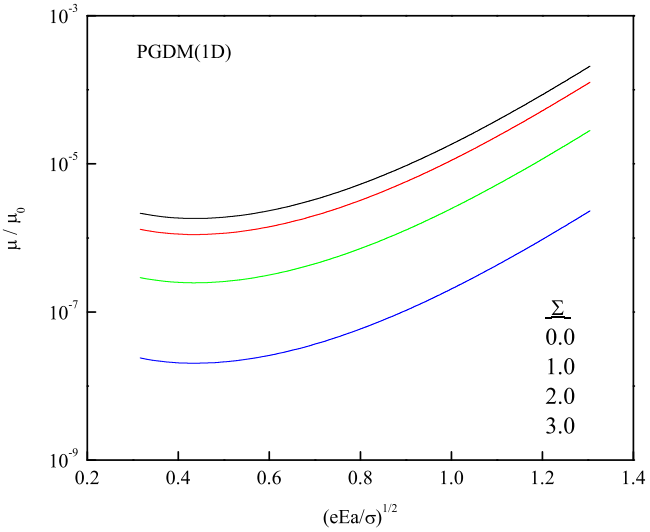

Figure 2.8. Normalized mobility of the PGDM as a function of $\sqrt{eEa/\sigma}$ with $\sigma =$ 0.1 eV and T=300 K for different Σ as indicated.

3. NUMERICAL APPROACH FOR 3D SYSTEMS

In this section the numerical method that is employed in sections 4 and 5 to compute the mobility for the three-dimensional versions of the disorder-based models is briefly described. Unlike the situation that obtains in 1D, where the constant current at each point in the chain provides a conserved quantity that allows for an exact analytical solution, the transport equations have no exact solution for three-dimensional systems. Thus, it is necessary to perform numerical calculations.

The earliest numerical disorder-based model calculations reported in the MDP literature employed Monte Carlo simulations [17, 23], which are conceptually easy to implement and can be performed for an arbitrarily large disordered system. In a Monte Carlo simulation, an extended realization of the disordered system is set-up in the computer, and the microscopic transition rates are then used to follow a charge carrier as it executes a field-biased random walk through the virtual array of transport sites. In such an approach one needs to execute many realizations of the random walk to obtain acceptable statistics and to assure that the distribution of local environments characteristic of the disordered medium is appropriately sampled.

An alternative method, used in the work that follows, is to compute the mobility by solving the master equation (9) that governs the evolution of the site probabilities $P_n(t)$ themselves. This approach has the advantage that it automatically incorporates all possible random walks that occur in the disordered system. This approach to solving the master equation and using that solution to determine the mobility is described below.

For each model, the longitudinal component of the mobility $\mu = \langle v_x \rangle / E$ is numerically computed for each value of the electric field $\vec{E} = E\hat{x}$ from the corresponding component of the steady-state drift velocity $\langle \vec{v} \rangle$. The latter is obtained

from the steady-state solution to the master equation

$$\frac{dP_{\vec{n}}}{dt} = \sum_{\vec{m}} \left[W_{\vec{n},\vec{m}} P_{\vec{m}}\left(t\right) - W_{\vec{m},\vec{n}} P_{\vec{n}}\left(t\right) \right] \equiv \sum_{\vec{m}} H_{\vec{n},\vec{m}} P_{\vec{m}}\left(t\right), \tag{210}$$

in which $\vec{n} = (n_x, n_y, n_z)$ is a vector lattice index having integer components of the lattice point at $\vec{\rho}_{\vec{n}} = \vec{n}a$, $P_{\vec{n}}\left(t\right)$ is the probability that the carrier is at lattice site $\vec{n}$ at time t and $W_{\vec{n},\vec{m}}$ is the hopping rate from site $\vec{m}$ to site $\vec{n}$ that depends on the separation distance and the energy difference between the sites involved in the transition. For a given initial condition $P_{\vec{n}}\left(0\right)$ the carrier's mean position $\langle \vec{\rho}\left(t\right) \rangle$ and velocity $\langle \vec{v}\left(t\right) \rangle$ are computed as

$$\begin{aligned} \langle \vec{\rho}\left(t\right) \rangle &= \sum_{\vec{n}} \rho_{\vec{n}} P_{\vec{n}}\left(t\right), \\ \langle \vec{v}\left(t\right) \rangle &= \frac{d}{dt} \langle \vec{\rho}\left(t\right) \rangle = \sum_{\vec{n},\vec{m}} \rho_{\vec{n}} H_{\vec{n},\vec{m}} P_{\vec{m}}\left(t\right). \end{aligned}$$

The steady-state drift velocity

$$\langle \vec{v} \rangle = \lim_{t\to\infty} \langle \vec{v}\left(t\right) \rangle = \sum_{\vec{n},\vec{m}} \rho_{\vec{n}} H_{\vec{n},\vec{m}} p^{(s)}_{\vec{m}} \tag{211}$$

can be computed from the steady-state probabilities

$$p^{(s)}_{\vec{m}} = \lim_{t\to\infty} P_{\vec{m}}\left(t\right) \tag{212}$$

which satisfy the linear set of equations

$$\sum_{\vec{m}} H_{\vec{n},\vec{m}} p^{(s)}_{\vec{m}}\left(t\right) = 0 \tag{213}$$

obtained by setting $dP_{\vec{n}}/dt = 0$ in (210). For the computations presented here, Eqs. (213) were solved for a cubic lattice having an edge of length $L = 64$ sites,

containing $N = 64 \times 64 \times 64 \sim 2.6 \times 10^5$ transport sites. Periodic boundary conditions are imposed on the transition rates so that carriers arriving at one face can make transitions to transport sites on the opposite face. In the presence of the field, the steady-state probabilities describe a non-equilibrium condition of constant average current flow along the direction of the applied field.

For calculations of the mobility performed for the GDM, each site of the lattice was independently assigned an energy $\varepsilon_{\vec{m}}$ drawn from a Gaussian distribution of width $\sigma = \langle \varepsilon_{\vec{m}}^2 \rangle^{1/2}$, and a geometric disorder parameter $\Gamma_{\vec{m}}$ drawn from a Gaussian distribution of zero mean and width $\delta\Gamma = \langle (\Gamma_{\vec{m}} - \langle \Gamma_{\vec{m}} \rangle)^2 \rangle^{1/2} = \Sigma/\sqrt{2}$. For each value of the electric field, then, transition rates $W_{\vec{n},\vec{m}}$ were assigned, according to Eq.(8), connecting each site to its 124 nearest neighbors lying within a $5 \times 5 \times 5$ cube centered on that site. With the transition rates determined, Eq. (213) was then solved using a relaxation algorithm.

Although the mobility is not computed in the same way as the original Monte Carlo simulations of Bässler and co-workers [17], the results obtained through the approach described above reproduce well-known results of the GDM. In Figure 3.1 a calculation of the mobility performed using this method (open symbols) as a function of the square root of the electric field is presented. The data in this figure are parametric in the energetic disorder parameter $\hat{\sigma} = \sigma/kT$, and have no geometric disorder ($\Sigma = 0$). In this calculation the values are set as $2\gamma a = 10$, $a = 6\,\text{Å}$, and $T = 290\,\text{K}$, to reproduce the conditions associated with the Monte Carlo simulations performed for the GDM as described in [17] and [23]. For purposes of comparison the corresponding Monte Carlo data have been digitized from Figure 7, on p. 302 of Ref. [23], which appear as filled symbols in the figure. Agreement of the two different approaches for computing the mobility is excellent, and serves as a validation of both.

Figure 3.2 displays results obtained with the same value of the parameters γ, a, and T, evaluated using this method (open symbols) for one fixed value of the energetic

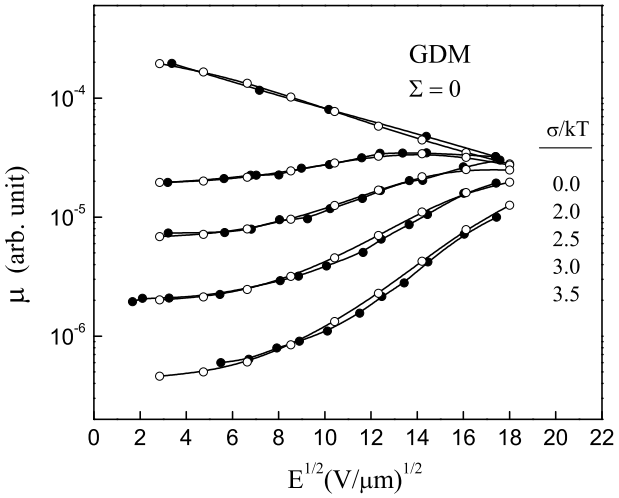

Figure 3.1. GDM Mobility as a function of $\sqrt{E}$ calculated using the method of the current method (open symbols) and the Monte Carlo method (filled symbols), for systems with no geometric disorder, and energetic disorder parameters $\hat{\sigma} = \sigma/kT$ as indicated.

disorder parameter $\hat{\sigma} = 3$, and with values of the geometric disorder parameter Σ as indicated. In this figure, filled circles indicate data digitized from Figure 9, on p. 303 of Ref. [23]. Here the overall agreement with previous work is also quite good, except at the highest value of Σ. The source of the discrepancy is not completely understood, but the convergence of our numerical solution to the master equation has been thoroughly checked, and additional calculations have been performed for several different disordered realizations of the lattice. The statistical error bars generated by entirely different realizations of the lattice, included for the data set with the highest value of Σ, are generally smaller than the data points themselves, except at the lowest value of the field, where the effects of fluctuations are most pronounced.

In implementing the various correlated disorder models, a similar procedure was used to that described above for the GDM, except that (i) either Miller-Abrahams

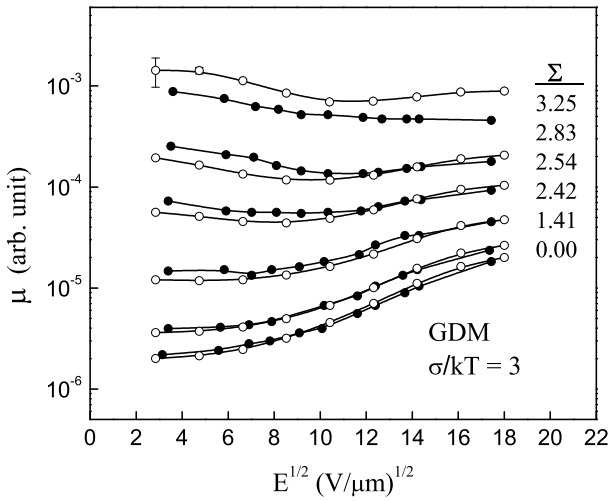

Figure 3.2. GDM Mobility as a function of $\sqrt{E}$ calculated using the method of the current method (open symbols) and Monte Carlo method (filled symbols), for systems with energetic disorder parameter $\hat{\sigma} = \sigma/kT = 3$ and geometric disorder parameter Σ as indicated.

rates (8) or polaronic rates (7) are used as is appropriate to each model, and (ii) the random lattice site energies $\varepsilon_{\vec{n}}$ were computed using a method that leads to a *correlated* Gaussian site energy distribution.

As with the GDM, the Gaussian distribution associated with the *single site* distribution function can be characterized by a standard deviation

$$\sigma = \langle \varepsilon_{\vec{n}}^2 \rangle^{1/2}$$

that is the same for all sites. In the original GDM, the site energies are independent, and described by an energy auto-correlation function of the form

$$\langle \varepsilon_{\vec{n}} \varepsilon_{\vec{m}} \rangle = \sigma^2 \delta_{\vec{n},\vec{m}}.$$

In the CDMs presented here, the energy auto-correlation function

$$\langle \varepsilon_{\vec{n}} \varepsilon_{\vec{m}} \rangle = \sigma^2 a / \left(|\rho_{\vec{n}} - \rho_{\vec{m}}| + a \right)$$

falls off as the first inverse power of the distance, as is appropriate for a medium in which the site energies arise from charge dipole interactions.

Thus, the numerical method employed here needs to produce individual realizations of a discrete Gaussian potential energy field $\varepsilon_{\vec{n}}$ of zero mean having specified (translationally invariant) correlations $C_{\vec{m}} \equiv \langle \varepsilon_{\vec{n}} \varepsilon_{\vec{n}+\vec{m}} \rangle$, defined on an integer lattice with $\vec{n} = (n_1, n_2, n_3)$, and $n_i = 1, 2, \ldots, L$. To accomplish this, for each realization it first generates what ends up being the Fourier transform

$$u_{\vec{k}} = \frac{1}{\sqrt{N}} \sum_{\vec{n}} \varepsilon_{\vec{n}} \, e^{-i\vec{k}\cdot\vec{n}} \tag{214}$$

of the desired energy field. Here the discrete complex field $u_{\vec{k}}$ is defined on the set Ω of N wave-vectors $\vec{k} = (k_1, k_2, k_3)$ in the 1st Brillouin zone of the associated reciprocal lattice, with $k_i = 2\pi m_i / L$ and $m_i \in \{-M, -M+1, \cdots, M-1\}$, and $M = L/2$. It is constructed as follows: for each wave-vector $\vec{k}$ with positive z component, a complex value $u_{\vec{k}} = \eta_{\vec{k}} e^{i\phi_{\vec{k}}}$ for the random field at wave-vector $\vec{k}$ is numerically determined in two steps. In the first step the real quantity $\eta_{\vec{k}}$ is independently chosen from a Gaussian distribution

$$P_{\vec{k}}(\eta) = \frac{1}{\sqrt{2\pi\sigma_{\vec{k}}^2}} \, e^{-\eta^2 / 2\sigma_{\vec{k}}^2} \tag{215}$$

having zero mean and a $\vec{k}$-dependent variance

$$\sigma_{\vec{k}}^2 = \frac{1}{\sqrt{N}} \sum_{\vec{n}} C_{\vec{n}} \, e^{-i\vec{k}\cdot\vec{n}} = \frac{1}{\sqrt{N}} \sum_{\vec{n}} \langle \varepsilon_{\vec{m}} \varepsilon_{\vec{m}+\vec{n}} \rangle \, e^{-i\vec{k}\cdot\vec{n}} \tag{216}$$

that is the Fourier transform of the desired correlation function. In the second step an independent random phase $\phi_{\vec{k}}$ is chosen uniformly in the interval $[0, 2\pi]$. For the value u_0 of the field at $\vec{k} = 0$, the phase ϕ_0 is set equal to zero. The values of $u_{\vec{k}}$ for wave-vectors $\vec{k}$ with negative z component are then assigned according to the relation $u_{\vec{k}} = u^*_{-\vec{k}}$. When averaged over many realizations, the moments of the complex fields thus constructed satisfy the relations

$$\langle u_{\vec{k}} \rangle = \langle \eta_{\vec{k}} \rangle \langle e^{i\phi_{\vec{k}}} \rangle = 0 \tag{217}$$

and

$$\langle u^*_{\vec{k}} u_{\vec{k}'} \rangle = \langle |u_{\vec{k}}|^2 \rangle \delta_{\vec{k}',\vec{k}} + \langle u^*_{\vec{k}} u^*_{\vec{k}} \rangle \delta_{\vec{k}',-\vec{k}} = \sigma^2_{\vec{k}} \delta_{\vec{k}',\vec{k}}, \tag{218}$$

where the average $\langle \hat{u}^*_{\vec{k}} \hat{u}^*_{\vec{k}} \rangle = \langle |\eta_{\vec{k}}|^2 \rangle \langle e^{2i\phi_{\vec{k}}} \rangle$ vanishes with $\phi_{\vec{k}}$ chosen randomly on $[0, 2\pi]$.

With the $u_{\vec{k}}$ chosen as described above, the values $\varepsilon_{\vec{n}}$ of the energy field of interest are obtained as the inverse Fourier transform

$$\varepsilon_{\vec{n}} = \frac{1}{\sqrt{N}} \sum_{\vec{k} \in \Omega} u_{\vec{k}} \, e^{i\vec{k}\cdot\vec{n}} \tag{219}$$

of the discrete complex field $u_{\vec{k}}$. As required, the final energies are real, i.e.,

$$\begin{aligned} \varepsilon^*_{\vec{n}} &= \frac{1}{\sqrt{N}} \sum_{\vec{k}} u^*_{\vec{k}} \, e^{-i\vec{k}\cdot\vec{n}} = \frac{1}{\sqrt{N}} \sum_{\vec{k}} u_{-\vec{k}} \, e^{-i\vec{k}\cdot\vec{n}} \\ &= \frac{1}{\sqrt{N}} \sum_{\vec{k}} u_{\vec{k}} \, e^{i\vec{k}\cdot\vec{n}} = \varepsilon_{\vec{n}} \end{aligned}$$

where the summation index has been relabeled , with $\vec{k} \to -\vec{k}$, and use made of the fact that $\hat{u}_{-\vec{k}} = \hat{u}^*_{\vec{k}}$. Furthermore, being a sum of Gaussian variables, the values of the real discrete field $\varepsilon_{\vec{n}}$ are themselves Gaussian distributed random variables that

obey the relations

$$\begin{aligned}
\langle \varepsilon_{\vec{n}} \rangle &= \frac{1}{\sqrt{N}} \sum_{\vec{k}} \langle u_{\vec{k}} \rangle \; e^{i\vec{k}\cdot\vec{n}} = 0 \\
\langle \varepsilon_{\vec{n}} \varepsilon_{\vec{n}'} \rangle &= \langle \varepsilon^*_{\vec{n}} \varepsilon_{\vec{n}'} \rangle = \frac{1}{\sqrt{N}} \sum_{\vec{k},\vec{k}'} \langle u^*_{\vec{k}} u_{\vec{k}'} \rangle \; e^{-i\vec{k}\cdot\vec{n}} e^{i\vec{k}'\cdot\vec{n}'} \\
&= \frac{1}{\sqrt{N}} \sum_{\vec{k},\vec{k}'} \sigma^2_{\vec{k}} \; \delta_{\vec{k},\vec{k}'} e^{-i\vec{k}\cdot\vec{n}} e^{i\vec{k}'\cdot\vec{n}'} \\
&= \frac{1}{\sqrt{N}} \sum_{\vec{k}} \sigma^2_{\vec{k}} \; e^{-i\vec{k}\cdot(\vec{n}-\vec{n}')} = C_{\vec{n}-\vec{n}'}.
\end{aligned}$$

The numerical implementation employed here, therefore (i) chooses

$$C_{\vec{n}-\vec{m}} = \langle \varepsilon_{\vec{n}} \varepsilon_{\vec{m}} \rangle = \frac{\sigma^2 a}{(|\rho_{\vec{n}} - \rho_{\vec{m}}| + a)} = \frac{\sigma^2}{(|\vec{n} - \vec{m}| + 1)} \tag{220}$$

equal to the desired auto-correlation function, (ii) numerically computes via fast Fourier transforms the variance

$$\sigma^2_{\vec{k}} = \frac{1}{\sqrt{N}} \sum_{\vec{n}} C_{\vec{n}} \; e^{i\vec{k}\cdot\vec{n}}, \tag{221}$$

(iii) constructs a random energy field u_k as outlined above, and (iv) performs another fast (inverse) Fourier transform, as in (219), to obtain the discrete energy field $\varepsilon_{\vec{n}}$ required.

The method used here to generate a correlated Gaussian random potential is different than that employed in some other CDMs [11], in which each site of the lattice is actually populated with a randomly oriented electric dipole moment, with the energy at a given site computed from the interaction between a charge at that site and all the electric dipoles in the medium. In these other implementations, which are in some sense more closely aligned with the underlying materials physics, the energy distribution is only approximately Gaussian, unlike the formulation provided here,

in which the discrete energy landscape is algorithmically constructed to be a true (correlated) Gaussian random field. In the next two sections results using this numerical method will be compared with the experimental data for 30% DEH:PC.

4. COMPARISON OF 3D DISORDER MODELS WITH 30% DEH:PC

In this section numerical calculations performed using the disorder based models described in the Introduction are compared to hole mobilities measured in 30% DEH:PC, as reported by Mack, et al. [19]. To aid in this comparison, the mobility data have been numerically digitized from Figure 4 of Ref. [19], and included in plots along with each of the numerical calculations.

It is customary to determine the mean separation between dopant molecules in MDP through the relation

$$a = \rho^{-1/3} = \left(\frac{M}{cA\rho_M} \right)^{1/3} \tag{222}$$

where ρ is the number density of dopant molecules, M the molecular weight of the DEH dopant (1.12 g/mol), ρ_m the mass density (1.12 g/cm^3), A is Avogadro's constant (6×10^{23} /mol), and $c = 0.3$ is the fractional weight concentration of DEH in the sample [19]. Using these values gives a separation distance $a = 11.94\,\text{Å}$ for 30% DEH:PC.

In Ref. [22], Schein and Borsenberger deduce from the exponential dependence of the mobility in this material on the interdopant separation distance the value $\gamma = 0.5\,\text{Å}^{-1}$ for the overlap parameter required to compute transition rates. In all numerical calculations presented below, these specific values of a and γ are used, and the values of the electric field E and the temperature T are taken from the values reported for the experimental measurements.

The predictions of the disorder models along with mobility data digitized from Ref. [19] are shown at temperatures ranging from $T = 201\,\text{K}$ up to $T = 336\,\text{K}$, as indicated, and at fields covering a range from $4\,\text{V}/\mu\text{m}$ to $144\,\text{V}/\mu\text{m}$. For all the figures, the experimental data of Mack, et al. is represented by filled symbols, accompa-

nied by dashed straight lines indicating linear fits displaying the Poole-Frenkel law. The theoretical predictions are represented by open symbols, approximated by solid smooth curves to guide the eye. To produce the theoretical data, the parameters (ν_0, σ, Σ) were varied for the GDM and CGDM, and the parameters $(J_0, E_B, \sigma, \Sigma)$ for the PCDM and PCDM-Σ in order to obtain the best visual fit to the experimental data.

4.1. THE GAUSSIAN DISORDER MODEL

To obtain optimized fits of the GDM with the experimental data of Mack, et al. [19], the study began with a comparison that assumed no geometrical disorder, i.e., the value of the parameter Σ was set to zero, and the parameters σ and ν_0 were changed in an initial attempt to get the best visual fit to the experimental data. A representative set of data obtained by starting with an initial value of $\sigma = 0.1\,\text{eV}$, and increasing the energetic disorder is displayed in Figure 4.1. Qualitatively one sees that while the numerical predictions of the GDM appear to have a Poole-Frenkel-like straightness at high fields, a characteristic flattening and a decrease of the slope emerges at intermediate-to-low fields. From this sequence of plots, one also sees that increasing the energetic disorder parameter in this model tends to increase the slope, as well as the rate at which the data *spread* as a function of temperature. Clearly this spread of the theoretical curves is insufficient at $\sigma = 0.1\,\text{eV}$. While it approximately covers the right range at $\sigma = 0.13\,\text{eV}$, the increase of the slope at the lowest temperatures causes it to deviate from the corresponding data. At $\sigma = 0.122\,\text{eV}$ it is possible to fit the slope of the data at high fields either at high temperature (black curves with red open symbols) by adjusting ν_0, which simply scales the data up or down, or (using a different value of ν_0) to fit it at low temperature (red curves with black open symbols) , but it is not possible to fit both simultaneously. Focusing on this agreement with the slope at the extremes, however, the value of

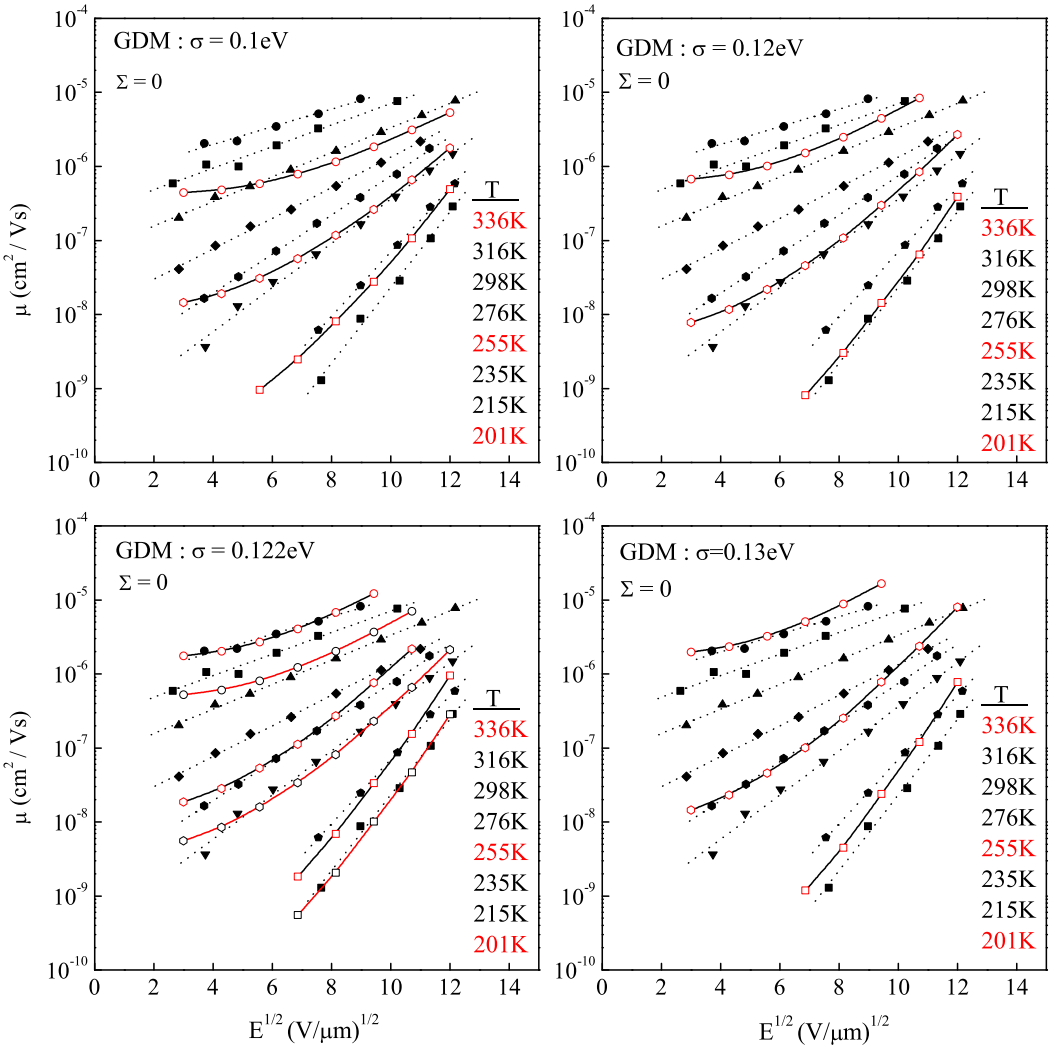

Figure 4.1. Numerical predictions of the GDM for 30% DEH:PC with $\Sigma = 0$.

$\sigma = 0.122\,\text{eV}$ was then fixed while the geometric disorder parameter Σ was increased from zero.

Representative data showing the change in the mobility with increasing geometrical disorder are shown in Figure 4.2. Increasing the geometrical disorder parameter Σ appears to increase the spread of the data, but it also increases the curvature. At a value $\Sigma = 2.5$ it obtains the correct spread, and at high fields the agreement with the slope at both high and low temperatures remains reasonable. Increasing Σ

beyond this level creates significant curvature that causes it to increasingly deviate from the experimental data.

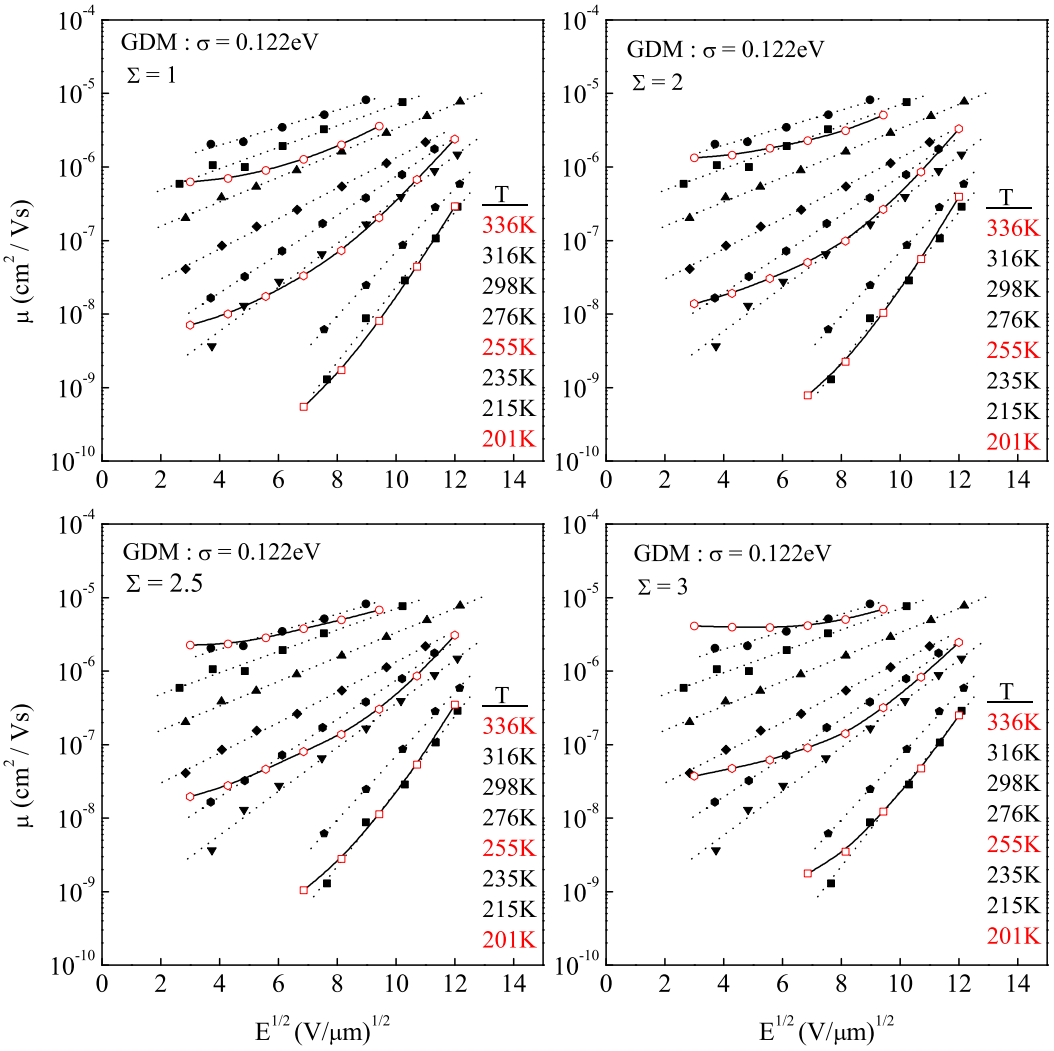

Figure 4.2. Numerical predictions of the GDM for 30% DEH:PC with $\sigma = 0.122\,\text{eV}$.

Thus, visually the most satisfying fit for the GDM, shown in Figure 4.3, is obtained with the specific parameter values $\sigma = 0.122\,\text{eV}$, $\Sigma = 2.5$ and $\nu_0 = 6 \times 10^{14}\,s^{-1}$. For these values of the parameters, the mobility predicted by the GDM at very high fields agrees reasonably well with the measured time-of-flight mobility,

particularly the slope of $\ln \mu$ with $\sqrt{E}$. As the field decreases below about $64\,\mathrm{V}/\mu\mathrm{m}$ (where $\sqrt{E} \sim 8\sqrt{\mathrm{V}/\mu\mathrm{m}}$), however, the GDM mobility flattens out, and significantly deviates from a Poole-Frenkel law, similar to the behavior seen in the 1D calculation (Figure 2.1). Thus, at least at low fields, where theoretical studies have shown the enhanced importance of spatial correlations, the GDM fails to describe experimental data for this material.

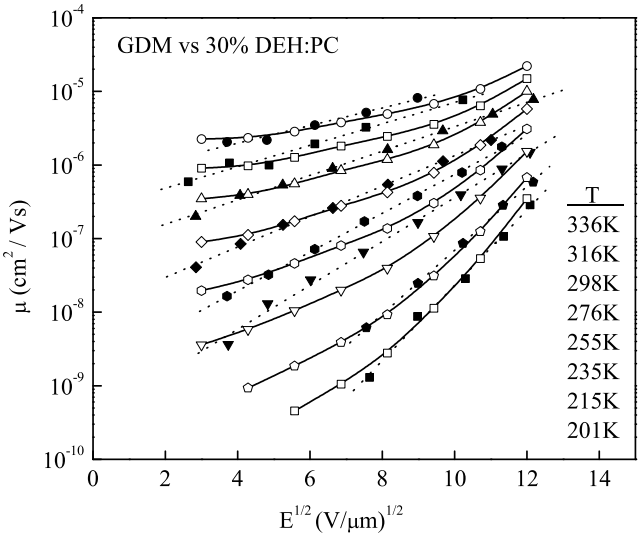

Figure 4.3. GDM mobility as a function of the $\sqrt{E}$ calculated with parameters $\nu_0 = 6 \times 10^{14}\,\mathrm{s}^{-1}$, $\sigma = 0.122$ eV, and $\Sigma = 2.5$, chosen to match the measured mobility of 30% DEH:PC.

4.2. THE CORRELATED GAUSSIAN DISORDER MODEL

In this section the experimental data of Ref. [19] are again presented, but now in conjunction with mobility calculations performed using the correlated Gaussian disorder model (CGDM), which uses Miller-Abrahams rates, as in the GDM, but incorporates a correlated energy landscape.

For this model the parameters (ν_0, σ, Σ) were varied in order to obtain an optimal fit of the data over the entire range of temperatures and electric fields. Filled symbols and dashed straight lines again show the experimental results, with open symbols and solid curves showing predictions of the CGDM.

The calculations were again started assuming no geometrical disorder, and systematically the energetic disorder was increased, as shown in Figure 4.4. Here the effect of the correlated energy landscape, is seen to reduce the systematic curvature at low fields seen in the GDM. The numerical predictions of the CGDM with $\sigma = 0.1\,\mathrm{eV}$ fit well the experimental data at $T = 336\,\mathrm{K}$, but fail to capture the entire spread that occurs with decreasing temperature. As before, increasing σ increases the spread of the data, but also changes the slope significantly in a way that causes it to deviate from the experimental data. For $\sigma = 0.126\,\mathrm{eV}$, the slope of the data can be made to fit the high temperature curve, or the low temperature curve, but it cannot capture the entire spread in data.

As with the GDM, keeping σ fixed at $0.126\,\mathrm{eV}$, the geometric disorder parameter Σ was increased from zero in an attempt to optimize agreement with the experimental data, as shown in Figure 4.5. Again, increasing Σ increased the spread of the data, but it also introduced significant curvature, which becomes all the more noticeable in this model as it emerges from what were previously rather straight Poole-Frenkel like curves. Thus fitting the data using the CGDM involves a tradeoff between getting the right slope, the right spread in the data, and avoiding excess curvature. The fit in Figure 4.6, produced with parameter values $\sigma = 0.126\,\mathrm{eV}$, $\Sigma = 3.4$ and $\nu_0 = 6 \times 10^{12} s^{-1}$ is shown in Figure 4.6 captures the spread and the approximate average slope of the data, but has considerable curvature. The geometric disorder parameter Σ that optimizes the data for the CGDM is the same as the one obtained with the GDM, while the value of σ has increased by about 4% over the GDM value, and the attempt frequency ν_0 has decreased by two orders of magnitude. This change

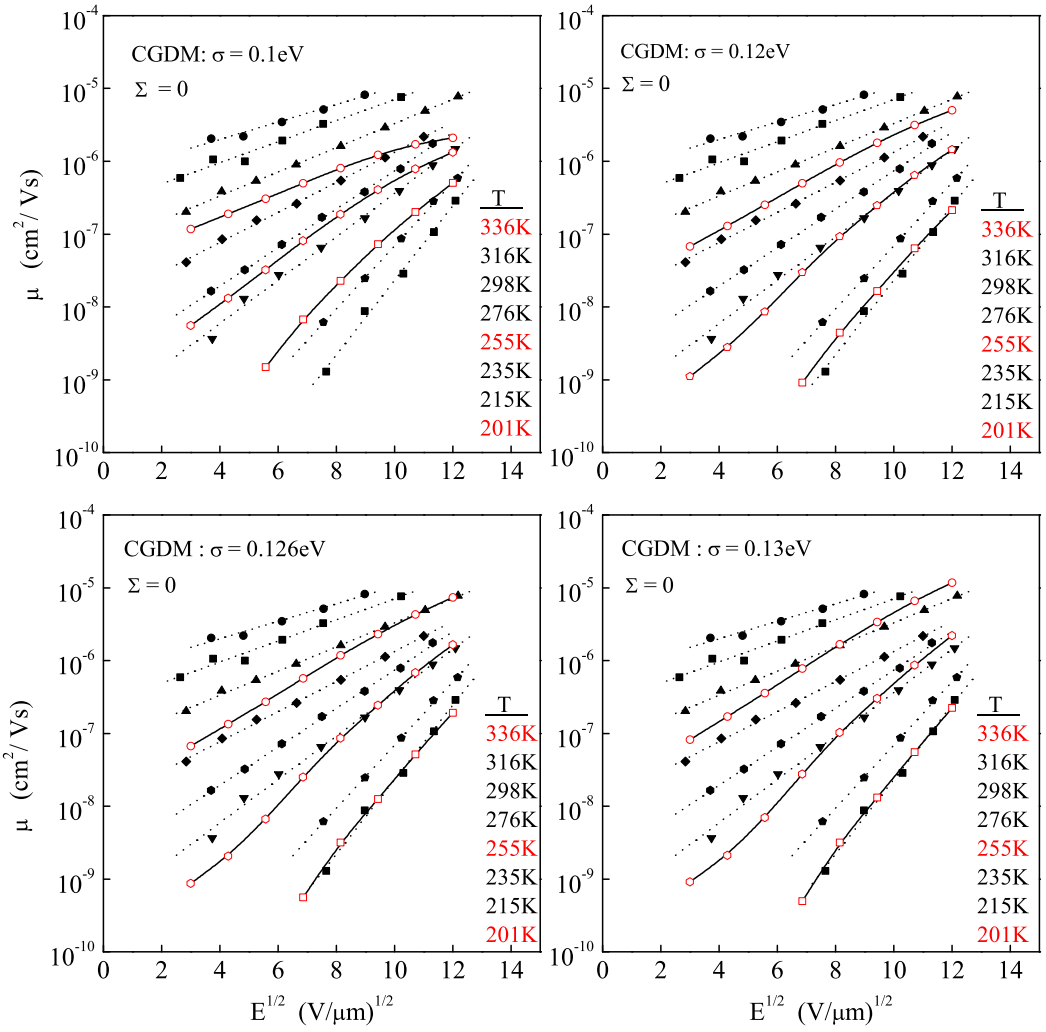

Figure 4.4. Numerical predictions of the CGDM for 30% DEH:PC with $\Sigma = 0$.

is understandable. For the same set of parameters, a material with correlated disorder will locally have a less strongly disordered energy landscape than with uncorrelated disorder. The local decrease in disorder tends to increase the mobility, and decrease the Poole-Frenkel slope. To obtain the correct spread of mobility over the range of temperatures represented, and to obtain the best qualitative fit to the data, it then becomes necessary to increase σ, and decrease the attempt frequency. Note, however, that the large value of the geometric disorder parameter required to fit the data

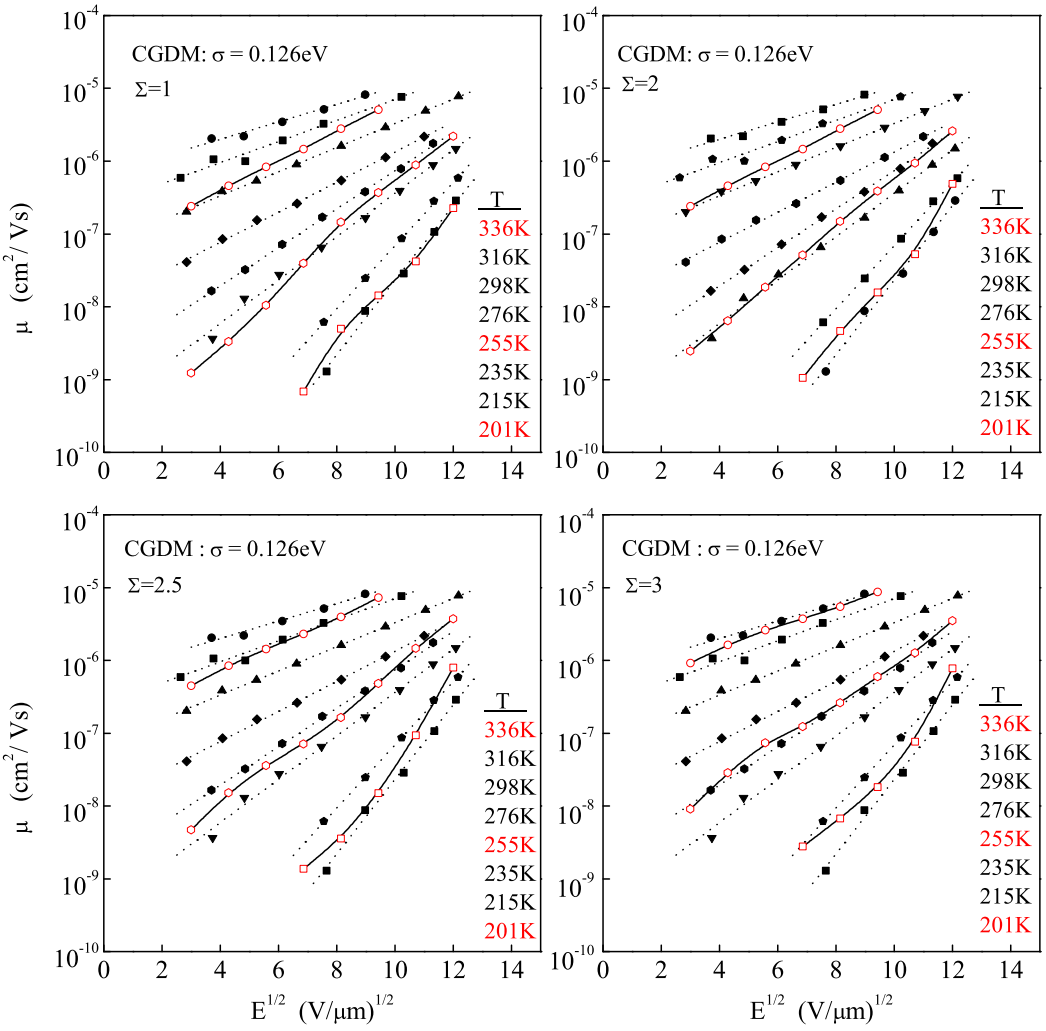

Figure 4.5. Numerical predictions of the CGDM for 30% DEH:PC with $\sigma = 0.126\,\text{eV}$.

over the entire range of temperatures and fields introduces significant curvature, i.e., deviations from ideal Poole-Frenkel behavior, in the field dependence of the CGDM. Earlier versions [11], of the correlated disorder model using Miller-Abrahams rates either did not include geometric disorder, or did not include it in the same way as the GDM. While this curvature is suppressed when the geometric disorder parameter is reduced to zero, it then becomes impossible to achieve the spread observed in the mobility data with increasing temperature, or to simultaneously approximate the ob-

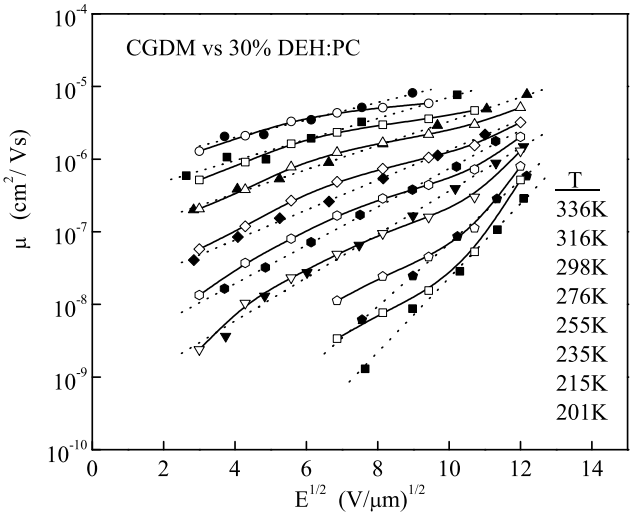

Figure 4.6. CGDM mobility as a function of $\sqrt{E}$ calculated with parameters $\nu_0 = 6 \times 10^{12}$ s^{-1}, $\sigma = 0.126$ eV, and $\Sigma = 3.4$, chosen to match the measured mobility of 30% DEH:PC.

served Poole-Frenkel slope at both low and high temperatures. Thus, whether spatial correlations were included or not, it does not appear possible with Miller-Abraham rates to obtain an entirely convincing simultaneous fit to both the temperature and the field dependence of the measured mobility.

4.3. THE POLARON CORRELATED DISORDER MODEL

In this regard, the correlated disorder theories that incorporate polaron hopping rates do a much better job. In this section the same experimental data (filled symbols) is compared with with predictions of the mobility obtained using the PCDM, with no geometric disorder (i.e. $\Sigma = 0$), and with the parameters (J_0, σ, E_B) varied to obtain an optimal fit of the entire data set. Open symbols and solid straight lines now represent predictions of the PCDM.

As stated earlier, two basic parameters σ and E_B were varied to get the best fit. The parameter J_0 acts simply as a scaling parameter similar to the role played by ν_0 in the GDM and the CGDM. So for the PCDM the fit is optimized by varying the parameters (σ and E_B) one at a time keeping the other one constant. Initially fixing σ at the value 0.1 eV, the polaron binding energy E_B was changed to understand the effect of changes in this parameter, as shown in Figure 4.7.

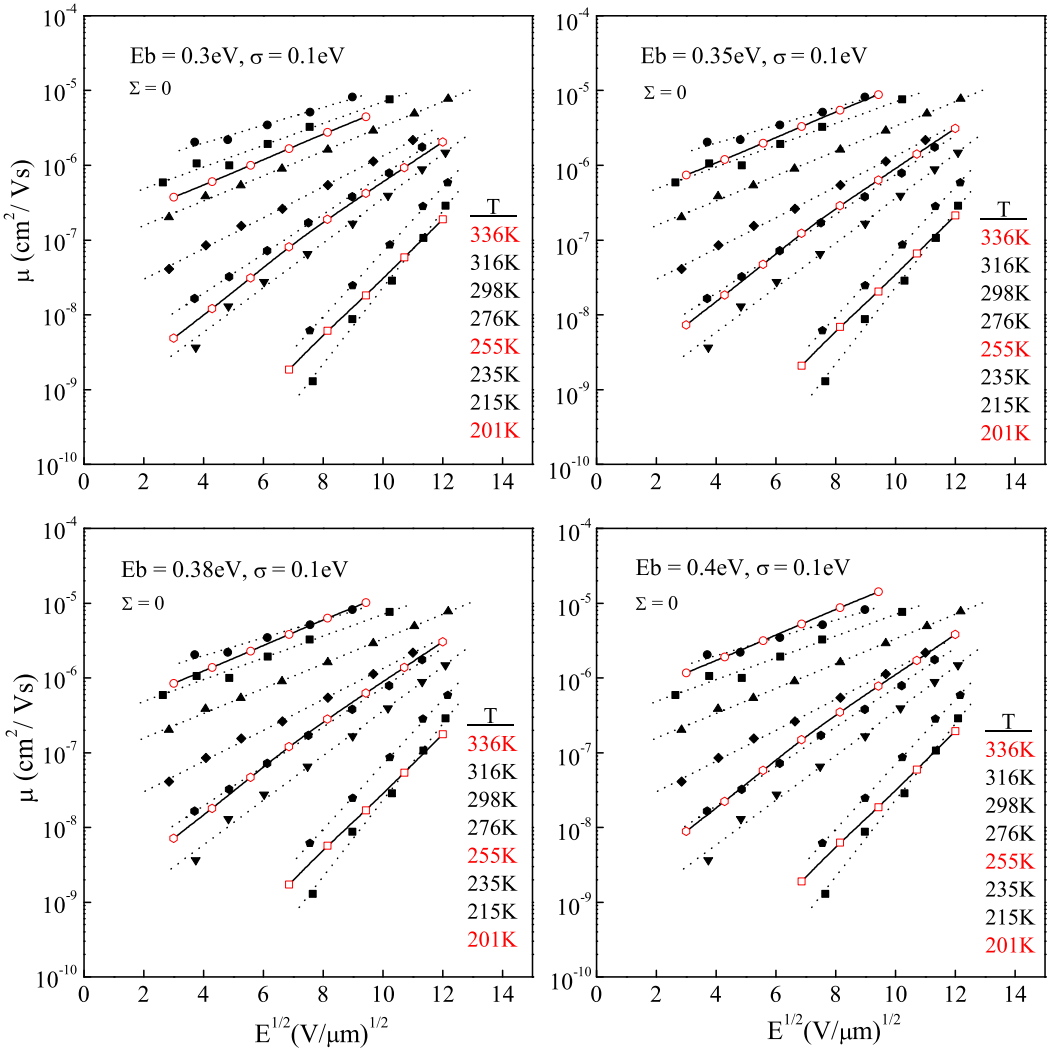

Figure 4.7. Numerical predictions of the PCDM with different E_B for 30% DEH:PC.

With $E_B = 0.3$ eV the spread is clearly insufficient, but it increases with increasing E_B. At $E_B = 0.35$ eV the data can capture the spread with temperature, but at $E_B = 0.38$ eV the slopes fit much better for all data sets. Qualitatively, agreement with the Poole-Frenkel field dependence over the entire range of fields is much better than with the GDM or the CGDM.

The effect of different σ fixing $E_B = 0.38$ eV were next studied as shown in Figure 4.8.

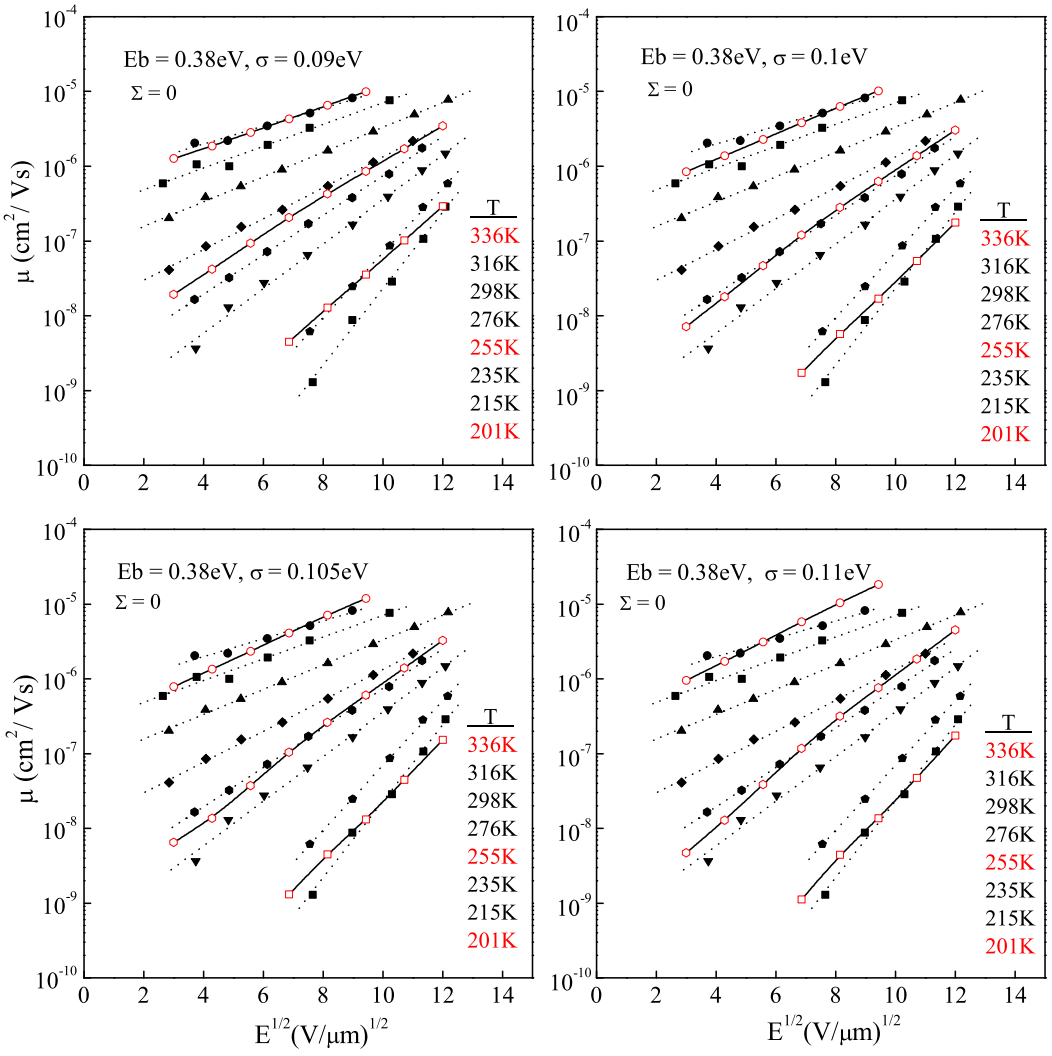

Figure 4.8. Numerical predictions of the PCDM with different σ for 30% DEH:PC.

Figure 4.9 shows the results of the mobility for different combinations of E_B and σ.

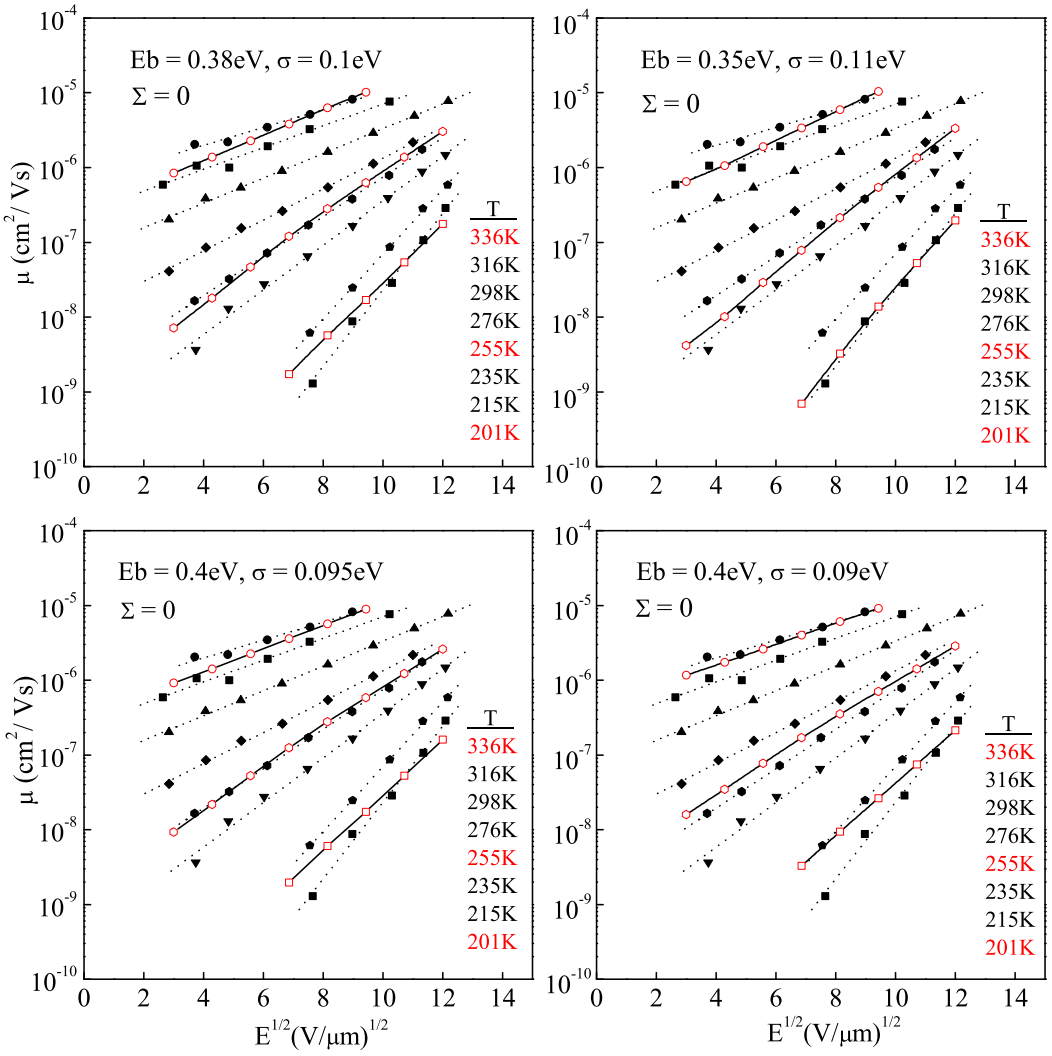

Figure 4.9. Numerical predictions of the PCDM with different combinations of E_B and σ for 30% DEH:PC.

The best overall fit for the PCDM, shown in Figure 4.10, was produced with parameter values $J_0 = 0.8$ eV, $\sigma = 0.100$ eV, and $E_B = 0.38$ eV . For this value of J_0, the matrix element connecting two dopant molecules separated by a minimal

separation of $\rho = 6$ Å is $J_0 e^{-\gamma\rho} = 0.034\,\text{eV}$. At the larger average inter-dopant separation $a = 11.94$ Å it reduces to $J_0 e^{-\gamma a} = 0.002\,\text{eV}$. Although, as can be seen from the

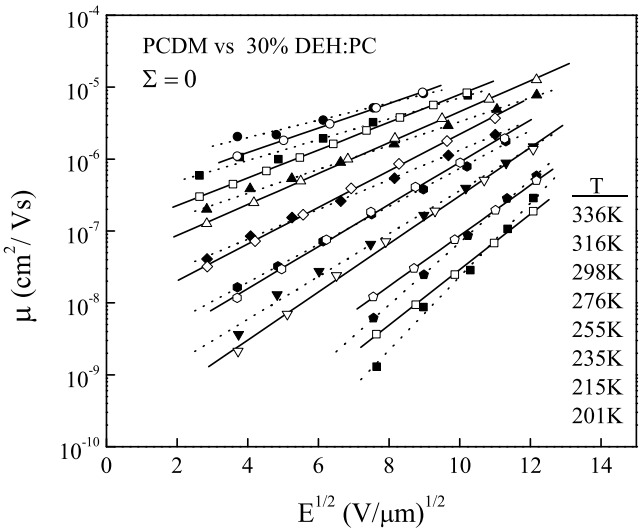

Figure 4.10. PCDM mobility as a function of $\sqrt{E}$ calculated with parameters $J_0 = 0.8\,\text{eV}$, $\sigma = 0.1$ eV, and $E_B = 0.38$ eV chosen to match the measured mobility of 30% DEH:PC.

figure, an appropriate spread of the data is obtained, it is not possible in this model to keep this spread and simultaneously match precisely the Poole-Frenkel slope of the data at both high and low temperatures. Thus in Figure 4.10, the slope of the computed mobility at high temperatures is a little steeper than that observed in the experimental data, while at low temperatures it is a little too shallow. While it is possible to change the parameters so that the Poole-Frenkel *slopes* agree with the data at both high and low temperature, this then produces a significant change in the spread of the data with temperature, so that although the numerical results can

be made to agree with the data at (say) low temperature, they will then miss the high temperature data by a considerable margin.

4.4. THE POLARON CORRELATED DISORDER MODEL WITH GEOMETRIC DISORDER

As seen in Figure 4.7, the numerical data for the PCDM with no geometric disorder captures the spread of the experimental data with temperature, with $\sigma = 0.1\,\text{eV}$, $E_B = 0.35\,\text{eV}$, but it fails to follow the slope seen in the experimental data at high and low temperatures. In Figure 4.11, results computed for the PCDM-Σ are presented, which include a spatially correlated energy landscape, polaron hopping rates, and non-vanishing geometric disorder. The numerical results in Figure 4.11 (open symbols), were computed with the parameters $\sigma = 0.1\,\text{eV}$, $E_B = 0.35\,\text{eV}$ and with various values of the spatial disorder parameter Σ to observe the effects of increasing geometrical disorder on the PCDM. From the figure it is clear that the slope becomes steeper with increasing Σ, while the spread changes as well.

After considerable exploration of the parameter space in this region, the best fit was obtained with the parameters $J_0 = 0.27\,\text{eV}$, $\sigma = 0.1$ eV, $E_B = 0.35$ eV, and $\Sigma = 2.0$, as shown in Figure 4.12. For this value of J_0, the matrix element connecting two dopant molecules separated by a minimal separation $\rho = 6\,\text{Å}$ is $J_0 e^{-\gamma\rho} = 134\,\text{meV}$. At the larger average separation $a = 11.94\,\text{Å}$, it reduces to $J_0 e^{-\gamma a} = 0.69\,\text{meV}$. Thus, by introducing geometric disorder it is possible to make the variation of the computed mobility with temperature and electric field convincingly match the experimental data. The single set of solid lines in this figure has been chosen to simultaneously pass as close as possible to the computed and experimentally measured mobility.

In both the mobility computed for the PCDM-Σ model and in the experimental data small deviations from Poole-Frenkel behavior occur at the lowest temperatures

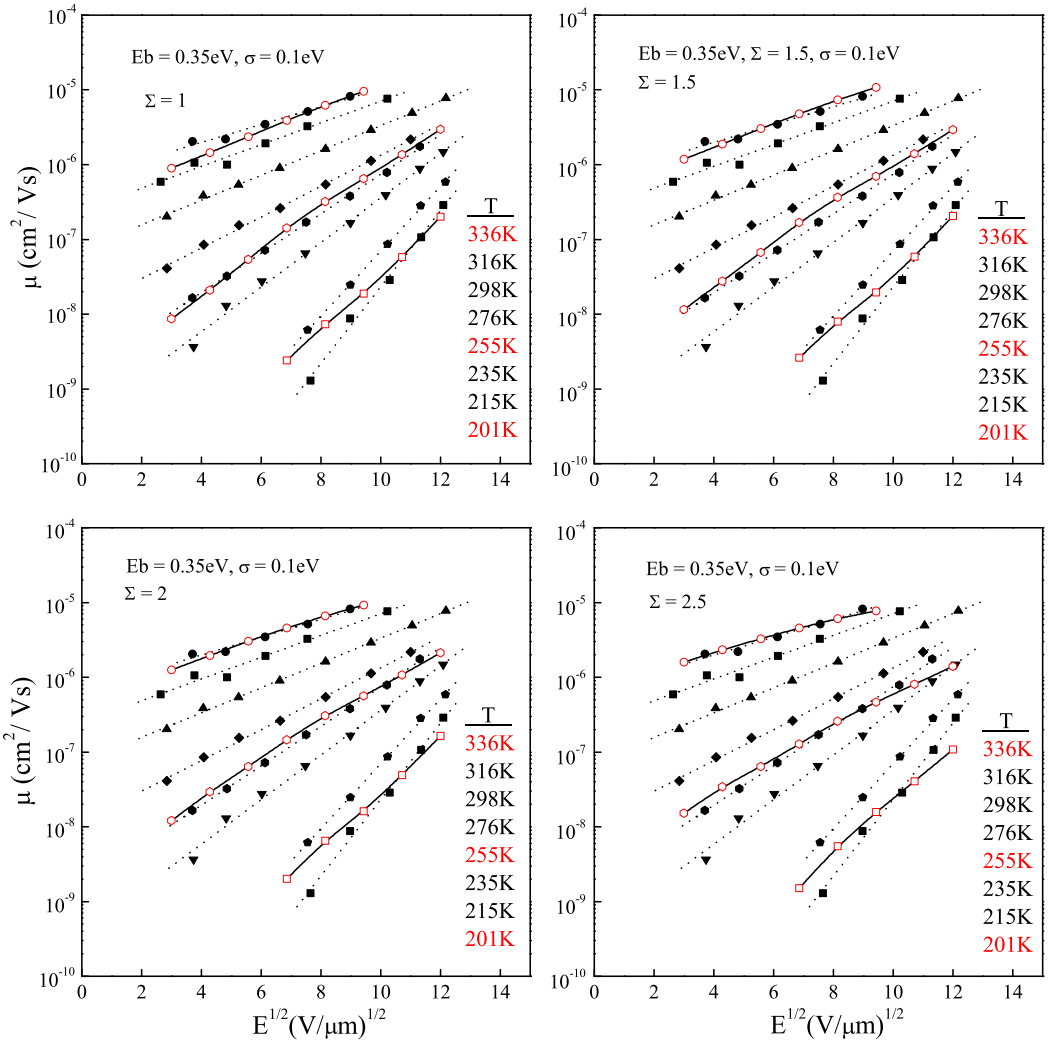

Figure 4.11. Numerical predictions of the PCDM-Σ for 30% DEH:PC.

and lowest electric fields, a regime where traps (or low energy regions of the sample) are known to alter the field and temperature dependence.

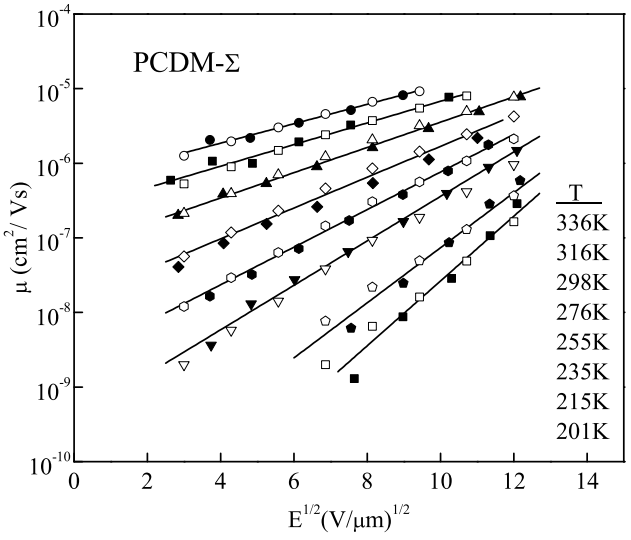

Figure 4.12. PCDM-Σ mobility as a function of $\sqrt{E}$ calculated with parameters $J_0 = 0.27$ eV, $\sigma = 0.1$ eV, $E_B = 0.35$ eV, and $\Sigma = 2.0$ chosen to match the measured mobility of 30% DEH:PC.

4.5. THE UNCORRELATED POLARON GAUSSIAN DISORDER MODEL (PGDM)

As a final model, and coming as somewhat of a surprise, in this section results are presented for the polaron version of the original Gaussian disorder model, referred to here as the PGDM, which uses polaron rates as in the PCDM but has transport taking place on an uncorrelated energy landscape. As mentioned in the introduction, attempts to explain the lack of agreement of the original GDM led to the deep understanding of the spatial correlations that take place in a dipolar disordered potential energy landscape. These correlations are an essential feature of the landscape, and are important for a proper description of the disordered medium. As seen, at low levels of geometric disorder, they provide a robust mechanism for producing Poole-Frenkel

type mobility over the entire range of electric field strengths probed in experiment. While there exist some purely model calculations (e.g., Gart-stein and Conwell [55], on uncorrelated disordered systems which employed polaronic or Marcus rates, a polaronic version of the original GDM does not seem to have been systematically studied in the MDP transport literature.

The 1D calculations on the PGDM presented in section 2, as shown in Figure 2.7 suggest that it shares many of the same failings as the GDM itself, i.e., a characteristic flattening of the mobility at low fields that causes deviations from desired Poole-Frenkel form. Indeed the predictions of the 1D version of the PGDM actually look very similar, qualitatively, to the results of the 3D calculations presented in Figure 4.3.

To study the PDGDM, numerical results were produced for a set of initial starting parameters with $\sigma = 0.1$ eV and $E_B = 0.3$ eV, in the range which produced reasonable results for the correlated version of the theory. To our surprise, the resulting curves, shown in the first panel of Figure 4.13 showed surprisingly good Poole-Frenkel field dependence except at very low fields, where a small amount of GDM like curvature appeared. It appears that, unlike what happens in 1D, with only nearest neighbor rates, the use of polaronic rates in a 3D system, even in an uncorrelated Gaussian energy landscape, can go a large way to suppressing the non-Poole-Frenkel deviations that arise with the use of Miller-Abrahams rates.

Although the numerical results for the initial set of parameters chosen was reasonably close to the experimental data, the values of σ and E_B were varied in attempt to find the best overall fit to the data, as shown in the remaining panels of Figure 4.13, leaving the geometric disorder parameter Σ set equal to zero.

In the end, the best simultaneous fit to the data at all temperatures, shown in Figure 4.14, was obtained with the initial values of the parameters chosen. For this fit, the optimal value for the strength J_0 of the overlap integral was $J_0 = 0.8$ eV.

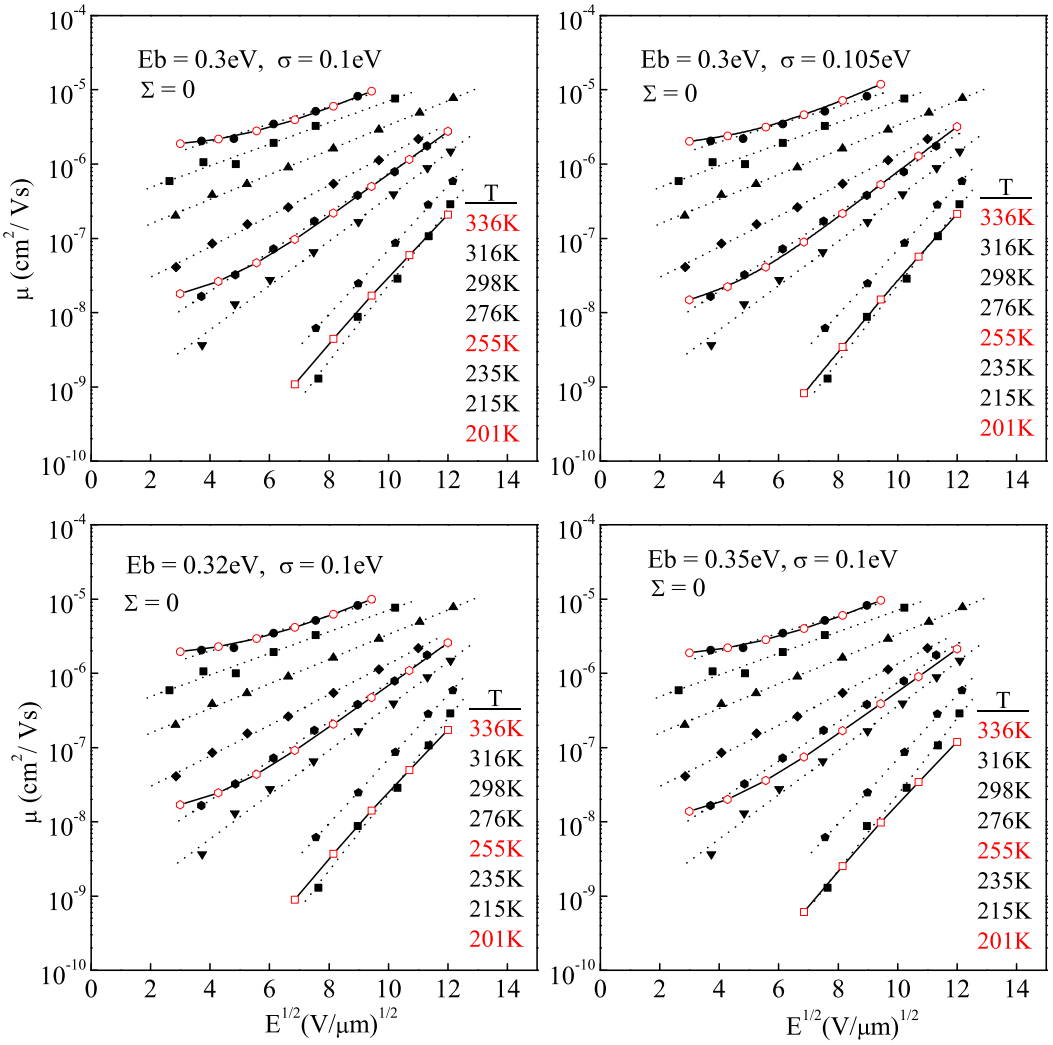

Figure 4.13. Numerical predictions of the PGDM for 30% DEH:PC with different parameters.

Although the numerical results retain a small, distinctly noticeable overall curvature, they track both the spread with temperature, and the average slope at high and low temperatures very well, except at low fields.

Table 4.1 summarizes the values of the parameters obtained in fitting the five different disorder theories to the experimental data for 30% DEH:PC.

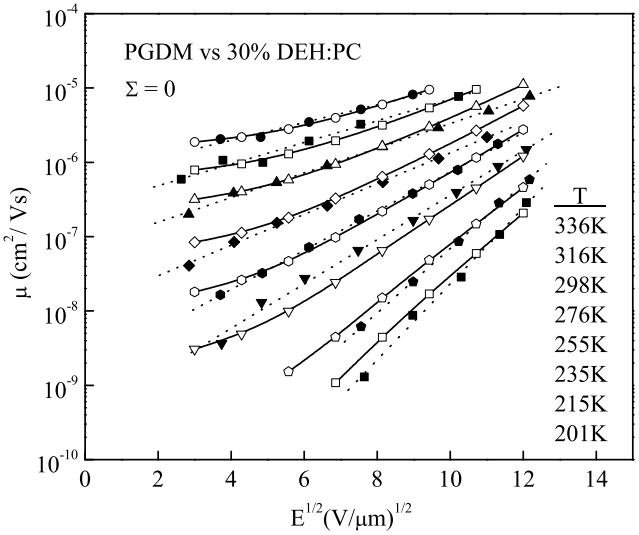

Figure 4.14. PGDM mobility as a function of $\sqrt{E}$ calculated with parameters $J_0 = 0.8\,\mathrm{eV}$, $\sigma = 0.1\,\mathrm{eV}$, $E_B = 0.3\,\mathrm{eV}$, and $\Sigma = 0$ chosen to match the measured mobility of 30% DEH:PC.

Table 4.1. Parameters determined by fitting the five disorder based theories indicated to the experimental mobility data for 30% DEH:PC.

Theory	ν_0 [s^{-1}]	σ[meV]	Σ	J_0 [eV]	E_B [meV]
GDM	6×10^{14}	122	2.5	-	-
CGDM	6×10^{12}	126	3.4	-	-
PCDM	-	100	-	0.80	380
PCDM-Σ	-	98	2.0	0.27	350
PGDM	-	100	-	0.80	300

5. A DILUTED LATTICE GAS MODEL OF SPATIAL DISORDER

In the original GDM of Bässler and coworkers [17] spatial disorder is treated through Gaussian fluctuations Γ_{nm} in the wave function overlap parameters of relative width Σ. As suggested in Figure 5.1 this heuristic treatment is intended to at least partially mimic fluctuations due to random intersite distances as well as molecular orientations.

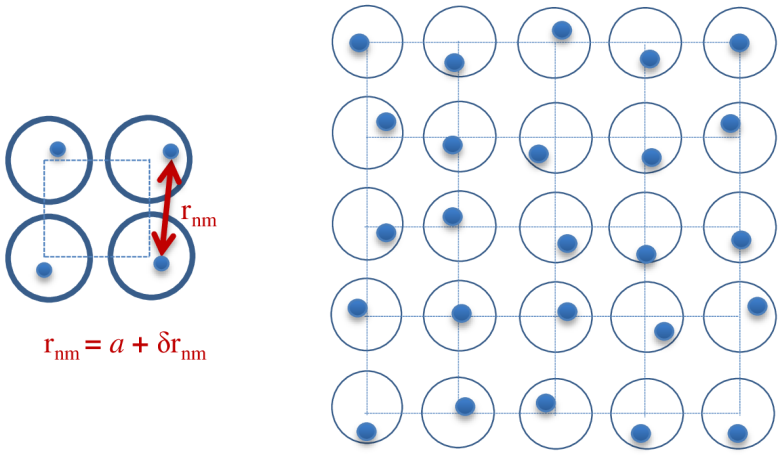

Figure 5.1. Gaussian distribution of geometrical disorder.

In reality, of course, dopant molecules are randomly distributed throughout a molecularly doped polymer, and fluctuations in nearest neighbor distances are not accurately described by a Gaussian distribution. As a consequence, a more realistic treatment of spatial disorder has been proposed that preserves the numerical advantages of working on a lattice, by treating the spatial distribution of dopant molecules as a *randomly-diluted lattice gas*.

In this model, as depicted in Figure 5.2 the dopant molecules randomly occupy the sites of a cubic lattice in some fractional concentration c, with the lattice spacing

$$a_0 = c^{1/3}a$$

adjusted to keep the number density $\rho = a^{-3}$ of transport sites constant and the same as it is in the experimental system of interest. At $c = 1$, in which 100% of the

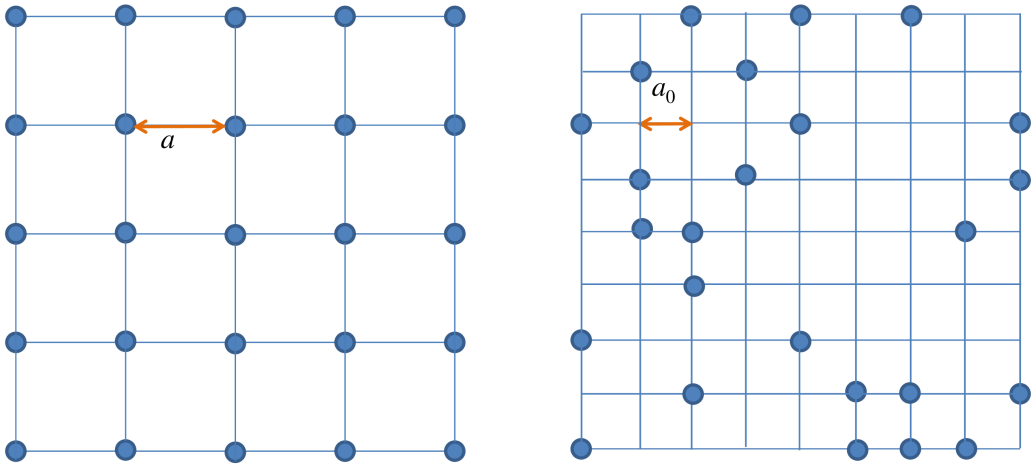

Figure 5.2. Distribution of transport sites on a filled lattice and with a partially filled lattice.

lattice sites are occupied by transport sites, the system is completely ordered. As c decreases, fluctuations in the nearest-neighbor distances develop, and at very small concentrations, as the mean separation between sites becomes large compared to the lattice spacing, the spatial distribution of sites approaches a completely random spatial distribution. Thus, in this treatment of spatial disorder, the parameter measuring the strength of the disorder is the quantity $q = 1 - c$, rather than the disorder parameter Σ that appears in the GDM. In this section some model calculations intended to

compare and contrast these two different models of geometrical or positional disorder as they apply to the PCDM, which produced the best fit to the experimental data on 30% DEH:PC, are presented.

As seen in the last section, in the models which include Gaussian geometrical disorder, the effect of increasing the strength of the geometrical disorder parameter Σ is to increase the spread in the data with temperature. In the GDM and CGDM, it also was observed to introduce significant curvature which enhanced deviations from the desired Poole-Frenkel behavior.

Numerical calculations on the original PCDM omitted the geometrical disorder parameter Σ and the numerical results for that model display convincingly robust Poole-Frenkel like behavior. The small amount of geometric disorder needed to optimize this model, in PCDM-Σ, did not have as dramatic an effect as it did in the GDM and the CGDM, but with increasing values of Σ, significant curvature actually does emerge in the same way.

The effect of increasing Gaussian geometric disorder in the PCDM-Σ is exhibited in Figure 5.3 which shows the mobility plotted as a function of the square root of the electric field E for increasing values of Σ.

In Figure 5.3 it can also be seen that the effect of this kind of Gaussian geometrical disorder on PCDM-Σ is generally to increase the mobility, an effect that was also observed in the original GDM (see, e.g., Figure 3.2). This effect is seen more clearly in Figure 5.4, in which the mobility is plotted for several different electric fields as a function of increasing amounts of Gaussian geometrical disorder.

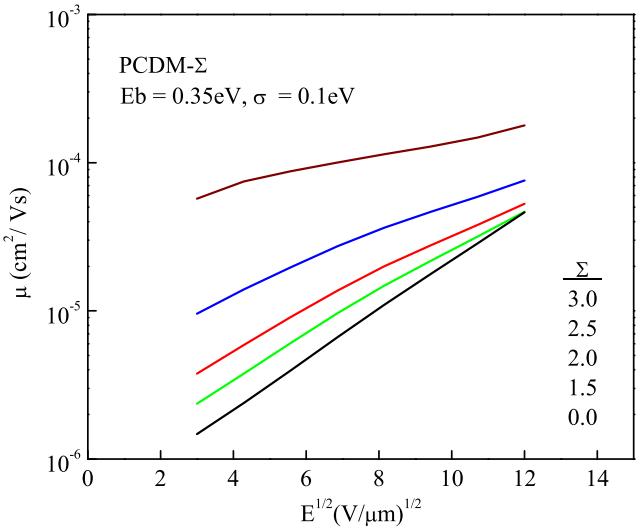

Figure 5.3. PCDM-Σ mobility as a function of $\sqrt{E}$ calculated with different Σ.

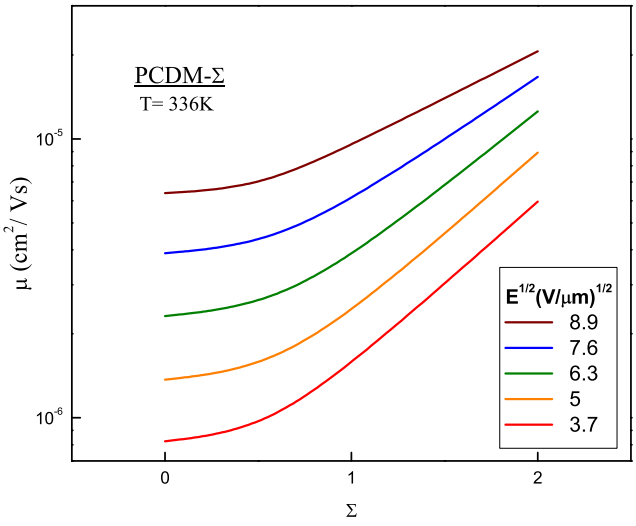

Figure 5.4. PCDM-Σ mobility as a function of Σ calculated for different electric fields.

This increase in the mobility with disorder is highly counter-intuitive, since in most physical situations increased disorder leads to degraded transport properties. One of the interesting questions, therefore, is whether this increase in mobility with increased disorder is peculiar to the heuristic treatment of the Gaussian model, or whether it arises in the more intuitively understood lattice gas model.

As a preliminary study, a series of calculations for the PCDM-c were produced with values of c from 0.1 to 1.0, with increments $\Delta c = 0.1$, with the other parameters taking values that optimized agreement of the PCDM-Σ model with the experimental data on 30% DEH:PC. Figure 5.5 shows the mobility as a function of the square root of the electric field produced for different values of c, as indicated, at a temperature of $T = 336K$, the highest temperature at which there is experimental data for this material.

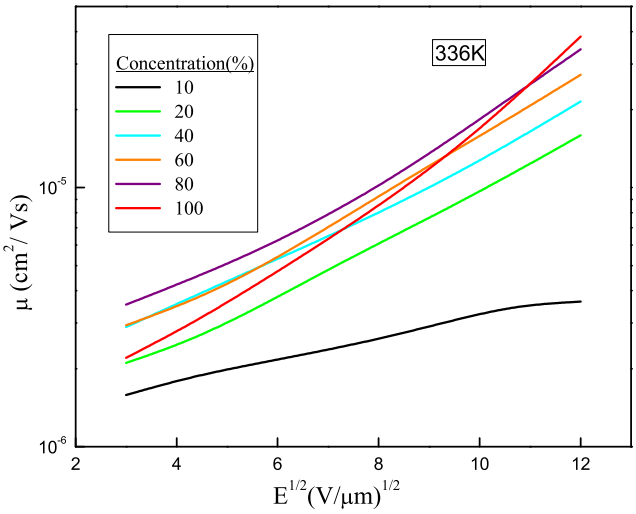

Figure 5.5. PCDM-c mobility as a function of the square root of the electric field calculated with different fractional concentrations c.

These data show that this kind of positional disorder in the system can effect the mobility in a significant way. In particular, it shows that for a small increase of disorder, as c decreases from 100% to 70%, for example, there is at low fields an overall initial increase of the mobility, while at large fields there is an initial decrease, indicating a marked change in the corresponding Poole-Frenkel slope. Initially, for small amounts of disorder, the curves tend to develop curvature, indicating deviations from Poole-Frenkel behavior, although it is not nearly as pronounced as with the Gaussian model of geometric disorder. This curvature tends to straighten out, returning to a more convincing Poole-Frenkel form at moderate and large amounts of disorder (c in the range of 10% to 40%, with the disorder strength $q = 1 - c$ varying from 60% to 90%).

In addition, it is clear that the initial increase at low fields is followed by a non-monotonic decrease, which becomes very apparent in the strongly disordered system with $c = 10\%$. The non-monotonic dependence on the strength of the disorder can be seen more clearly in Figure 5.6, which shows the mobility as a function of the disorder strength $1 - c$, for different values of the applied electric field as indicated. The general trend is for a mild increase in the mobility with increasing disorder (a milder version of what occurs in the Gaussian model), followed by a flat region for intermediate disorder, and then by a more marked decrease in the mobility for large amounts of disorder.

A few general conclusions can be drawn from these model calculations. First, the increase of mobility with disorder generally seen in the Gaussian model is not entirely an artifact: to the extent that the Gaussian model is intended to incorporate the effects of positional disorder, initial increases in disorder will tend to increase the mobility at low fields. In the lattice gas model, though, this increase occurs immediately, where as Figure 5.3 shows that in the Gaussian model, there is little increase in mobility initially, until a threshold is reached. In the lattice gas model,

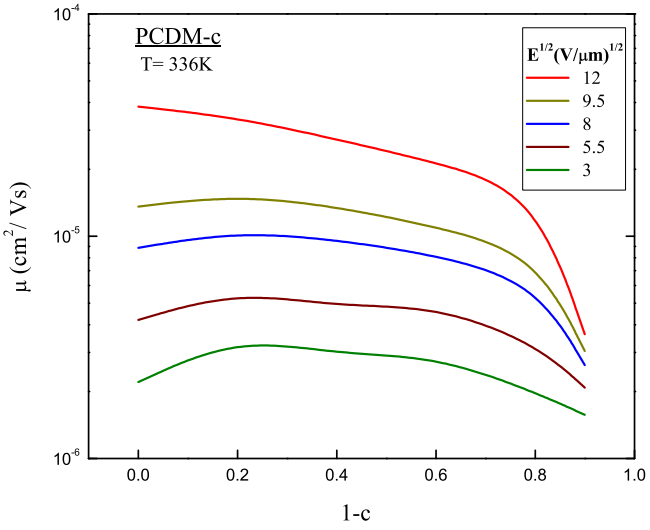

Figure 5.6. PCDM-c mobility as a function of fractional concentration c calculated for different electric fields.

the noticeable initial increase ends rather soon, and then flattens, with the mobility becoming insensitive to the disorder strength at intermediate levels of disorder, and then decreasing ultimately for large amounts of disorder, unlike the strong increase exhibited by the Gaussian model at large values of Σ. It appears that both models predict a decrease in the slope of the data as a function of the square root of the applied field with large amounts of disorder. In the Gaussian model this is accompanied by significant increased curvature, while in the lattice gas model the initial curvature introduced at lower levels of disorder has straightened back into reasonable Poole-Frenkel behavior.

After this initial theoretical exploration of the difference between these models of geometric disorder, calculations were undertaken for this model of the sort presented for the previous models in section 5. A preliminary set of sample calculations for different values of c is presented in Figure 5.7.

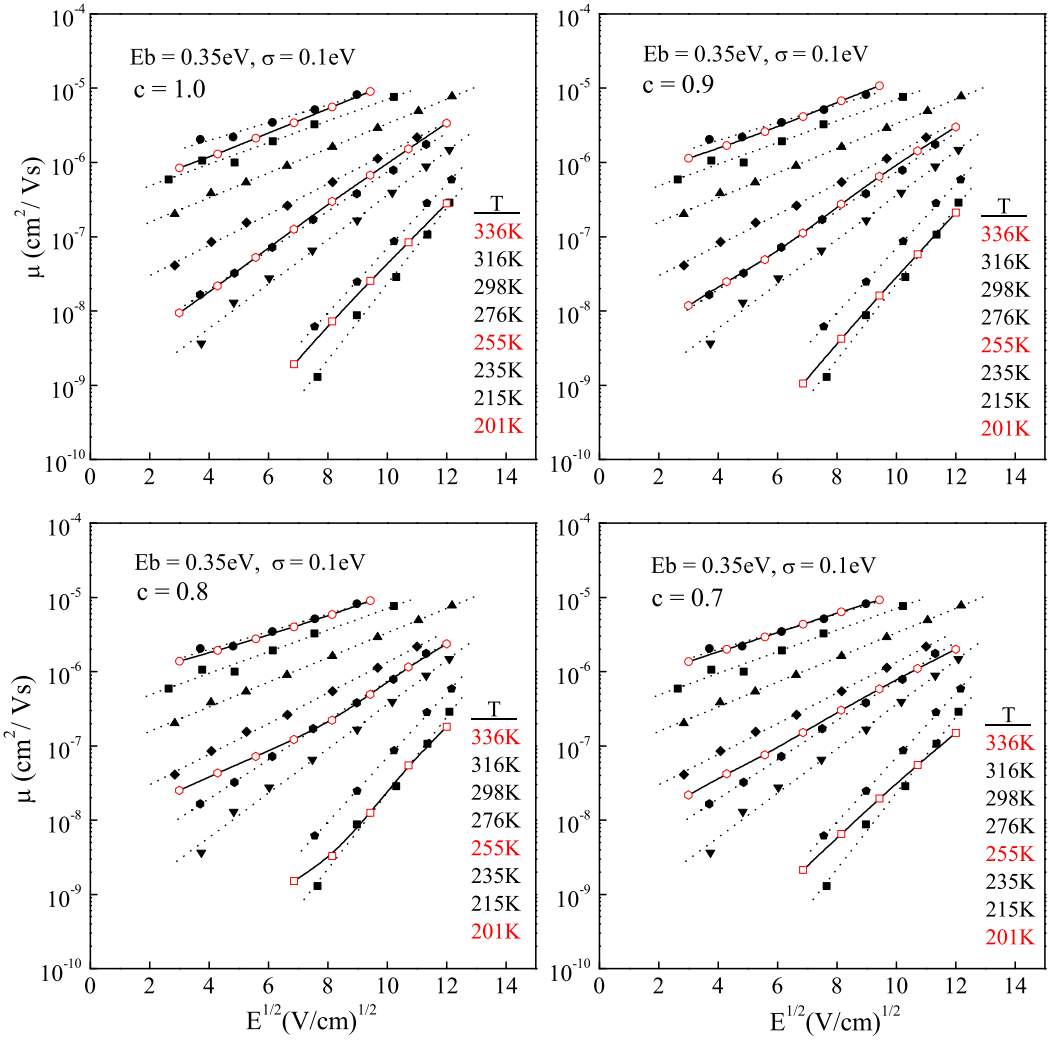

Figure 5.7. PCDM-c mobility as a function of $\sqrt{E}$ calculated for different fractional concentrations c

The best fit, shown in Figure 5.8 was obtained with $c = 0.9$, $\sigma = 0.1$ eV, $E_B = 0.35$ eV and $J_0 = 0.63$ eV.

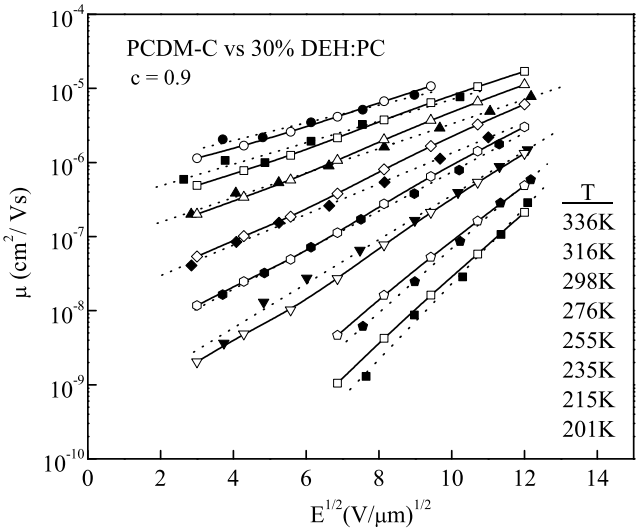

Figure 5.8. PCDM-c mobility as a function of $\sqrt{E}$ calculated for fractional concentration c=0.9 with the parameters $\sigma = 0.1$ eV, $E_B = 0.35$ eV and $J_0 = 0.63$ eV.

6. CONCLUSIONS

In this dissertation, a series of analytical and numerical calculations were presented for disorder based models that have been developed to explain the temperature and electric field dependence of photo-injected charge transport in molecularly-doped polymers. The purpose of these calculations was two-fold.

First, they were performed in an attempt to understand how the behavior of different disorder models depend on the microscopic parameters that define them. To this end a series of new analytical calculations were presented for 1D versions of the disorder based models, in which transport occurs via nearest-neighbor hopping rates. These calculations support the general notion that models that include spatial correlations (of the kind known to be an important ingredient in systems with dipolar disorder) do a better job of describing the Poole-Frenkle field dependence that is an almost universal feature of charge transport in these materials than models that do not. The two uncorrelated models for which these calculations were carried out, the original Gaussian disorder model (GDM) that used Miller-Abrahams rates, and a polaronic variation of it (PGDM) both show a flattening of the slope of the mobility *vs* the square root of the field at intermediate to low fields that is not seen in experiment. Of the correlated models, the 1D version of the correlated Gaussian disorder model (CGDM) which uses Miller-Abrahams rates did the best job of maintaining a convincing Poole-Frenkel mobility, with the polaronic version appearing to approach a maximum at high fields, an effect that is suspected to arise from the functional form of the polaron or Marcus hopping rate. All 1D models studied analytically exhibited a mobility that exponentially decreases with increasing spatial disorder Σ, in sharp contrast to previously obtained numerical results on the 3D version of the GDM.

The second main goal of the calculations in this dissertation was to provide what is believed to be the first systematic comparisons of the predictions of disorder based models with actual experimental data, which due to the numerical difficulties of the models involved has not been attempted until now. No attempt was made to fit the predictions of the 1D calculations to experiment, because it is generally understood that 1D models show much greater exponential dependence on field and temperature than 3D models, due to the fact that in 1D a carrier is forced to go over every hill and valley in the potential energy landscape, while in real 3D systems, it can detour around energetic mountains and thus avoid energetically difficult climbs that it is forced to make in 1D.

Thus, the series of numerical 3D calculations presented in section 4 was performed. Interestingly, the 3D calculations show that even the qualitative intuition developed from studies of 1D nearest-neighbor models does not directly extended to more realistic 3D systems.

The three dimensional version of the uncorrelated GDM, with Miller-Abrahams rates, using parameters chosen to best represent the experimentally measured mobility of the 30% DEH:PC comes the closest to being well represented by its 1D counterpart, showing the same characteristic flattening at low fields in 3D as it does in 1D, a feature which thus prevents it from even qualitatively describing the experimental data at all electric fields.

Numerical calculations on the 3D version of the CGDM, with Miller-Abrahams rates and a correlated energy landscape exhibit a robust Poole-Frenkel behavior at low levels of Gaussian geometric disorder, like its 1D counterpart, but with small amounts of geometric disorder it is impossible to simultaneously capture the spread of the data with temperature, and the Poole-Frenkel slopes at high and low temperatures. To capture the spread of the data with temperature it is necessary to increase the geometric disorder significantly. But this model shows an unexplained sensitivity to

the spatial disorder parameter Σ , in that it develops strong curvature, and significant deviations from the experimentally observed Poole-Frenkel behavior at the levels of Σ needed.

The correlated disorder models (PCDM and PCDM-Σ) that use small polaron rates and a correlated potential energy landscape also show a robust Poole-Frenkel field dependence at low levels of spatial disorder. Moreover, with this model it is also possible to capture the spread of the data with temperature using no spatial disorder. These fits are not perfect, however, in the sense that it was not possible to, at the same time, obtain precise agreement with the Poole-Frenkel slopes at both high and low temperatures. Adding a moderate amount of Gaussian geometrical disorder allows those features to be captured as well, and with polaronic rates the numerical results seem more stable to the incorporation of geometrical disorder. The most convincing fit was thus obtained using the PCDM-Σ with appropriately chosen parameters.

Calculations on the uncorrelated, and largely unstudied PGDM, which assumes an uncorrelated energy landscape and polaronic rates also show surprisingly good agreement with data at all but the lowest fields, where a small amount of the flattening observed in the GDM still arises. How this Poole-Frenkel behavior over such an extended range occurs is, at the moment, not well understood. It is tempting to speculate that the exponentially quadratic term in the polaronic hopping rates (7) strongly suppress the hopping rate to nearest-neighbors differing widely in energy (which can occur in an uncorrelated energy landscape), forcing the particle to undergo hops to sites further away, but closer in energy. This sort of variable-range hopping mechanism clearly has the effect of making the sites to which transitions actually occur closer together in energy than they otherwise might have been, similar to what happens in the presence of correlations. This effect was clearly not seen in the 1D calculations, because that calculation restricted hops to nearest neighbors, so that a

variable range hopping is automatically precluded. This surprising result is clearly an area for further investigation.

Finally, in section 5 of this dissertation, numerical calculations have been presented on a 3D version of the polaron correlated disorder model in which spatial or positional disorder was treated using a randomly diluted lattice gas model, allowing for real, rather than heuristic, variations in the positions of the transport sites with increasing disorder. These results showed both similarities and differences with the Gaussian geometric disorder models implemented previously. Calculations for this model are currently underway in attempt to fit the experimental data on 30% DEH:PC of the sort presented in section 4, and will be presented in a separate publication.

This section closes with a discussion of recent comments in the literature which point to a number of puzzles that have arisen in meta-analyses of existing experimental data on molecularly-doped polymers.

In particular, it is noted that renewed attempts have recently been made to understand how the empirical parameter σ extracted from experimental measurements using the different *empirical formulae* provided by disorder-based models, depend upon the concentrations, dipole moments, and other properties of the molecular constituents that make up an MDP [66]. A surprising conclusion from a study by Schein and Tyutnev [66] is that the empirically determined parameter σ_e that characterizes the temperature dependence of the zero-field mobility $\mu_0(T) = \lim_{E\to 0}\mu(E,T)$ through the GDM-inspired formula $\mu_0(T) \propto \exp\left[-\left(2\sigma_e/3kT\right)^2\right]$, is largely *independent* of dopant concentration in a very large class of materials, in apparent contradiction to any reasonable disorder based explanation. Indeed, the authors of Ref. [66] have even made the suggestion that activation energies in molecularly-doped polymers are entirely of intramolecular origin.

In a rebuttal to this suggestion [64], Novikov and Vannikov have pointed out that real sources of energetic disorder affect the overall temperature dependence of the zero field mobility $\mu_0(T)$ differently from the way they affect the temperature dependence of the coefficient multiplying $\sqrt{E}$ in the logarithm of the mobility (the so-called Poole-Frenkel factor $\beta_0 = \partial \ln \mu / \partial \sqrt{E}$). Indeed, different kinds of disorder (e.g., static and induced electric multipole contributions having different spatial correlations) can influence these terms in different ways. Research on correlated disorder models reveals that the Poole-Frenkel factor should depend only on those components of disorder having the longest range spatial correlations, while $\mu_0(T)$ is sensitive to all contributions to the energetic disorder [12].

In addition to the points raised in [64], it is noted here that the empirical fitting formulae associated with the different disorder models each characterize the numerical results of those models only for certain fixed values of basic parameters such as the lattice spacing a, and the overlap parameter γ. In most cases it appears that the temperature T has been kept fixed while only the strength of the disorder was changed to produce results parametric in $\hat{\sigma} = \sigma/kT$. Application of such formulae to the analysis of real experimental data can thus involve an essential extrapolation to parameter regimes usually not verified through direct numerical calculations. This presents an additional source of uncertainty in meta-analyses such as that in [66], which explicitly assume that the empirical formula used to extract disorder parameters directly and faithfully represents the predictions of the underlying disorder model itself. It has been noted that the GDM analysis performed in the previous section provides an opportunity to directly test this assumption for an experimentally relevant range of parameters.

Thus, e.g., in Figure 6.1 a comparison is presented of the empirical formula (10), often incorrectly cited as representing the predictions of the GDM, with mobilities computed for that model using the parameters $\sigma = 0.122\,\mathrm{eV}$, and $\Sigma = 2.5$

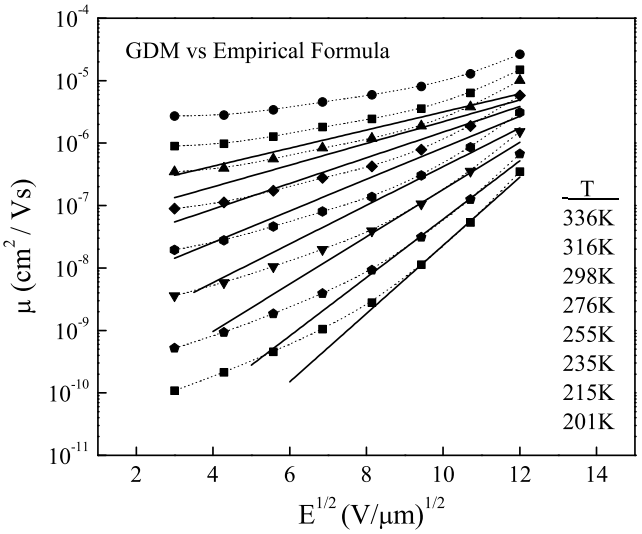

Figure 6.1. Predictions of the empirical formula (10) compared to the mobility of the GDM with parameters $\sigma = 0.122\,\mathrm{eV}$ and $\Sigma = 2.5$ chosen to fit the GDM to 30% DEH:PC.

that best fit the measured mobility of 30% DEH:PC. In this figure, the results of the empirical formula, computed with the same value of σ and $\hat{\Sigma} = \Sigma$ as in the numerical calculation of the mobility for the GDM, appear as solid straight lines. In Figure 6.2 a comparison of the predictions of the empirical formula with the measured mobility for 30% DEH:PC is shown.

Although there is reasonably good agreement at the lowest values of temperature, these comparisons clearly show that for this set of disorder parameters the empirical formula (10) fails to reproduce, even qualitatively, the *combined* temperature and field dependence of the Gaussian disorder model (even at high fields), or of the experimental data. Although one could employ the usual methods of the disorder formalism [23], which uses Eq. 10 to extract empirical disorder parameters, these parameter values would obviously have no direct relation to those that define the GDM.

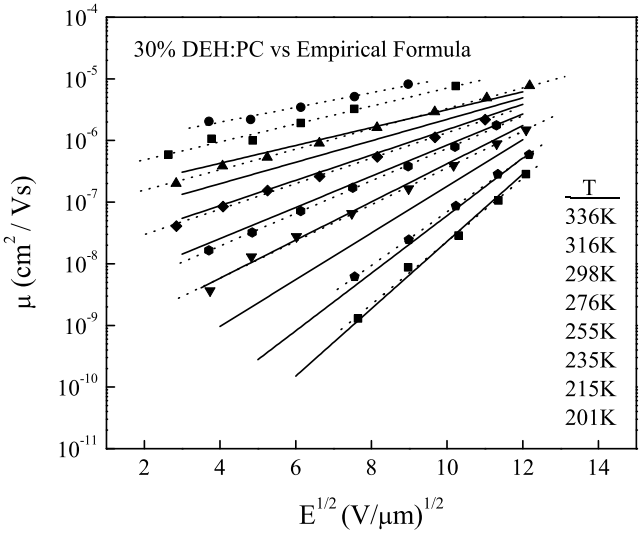

Figure 6.2. Predictions of the empirical formula (10) compared to the mobility of 30% DEH:PC, with parameters $\sigma = 0.122\,\mathrm{eV}$ and $\Sigma = 2.5$ chosen to fit the GDM to 30% DEH:PC.

It is not entirely clear why Eq. 10 does such a poor job of reproducing the results of the GDM itself. The discrepancy may stem from the fact that the formula was constructed from the outset to reproduce the temperature dependence of the *zero-field mobility*, i.e., as extrapolated from the values of the mobility at large fields, where $\ln \mu$ is approximately linear in $\sqrt{E}$. Indeed, a rough visual extrapolation of the predictions of the curves representing the GDM in Figure 6.1 at high fields, back to the point where the linear portions would intersect the vertical axis, shows that they would do so at a point fairly well predicted by a similar extrapolation made with the straight lines representing Eq. 10. Clearly, however, this forced agreement with the extrapolated mobility at zero field ends up producing a qualitatively incorrect description of the variation with temperature of the high-field Poole-Frenkel regime.

Due to these uncertainties, in the numerical calculations presented in this dissertation the use of empirical fitting formula of this type have been avoided entirely

in favor of an approach which utilizes a direct comparisons of disorder-based theories with experimental data on one of the most well-studied MDPs, 30% DEH:PC. It is clear from these results that theories with polaronic models with correlated disorder provide better agreement with the observed Poole-Frenkel field dependence of the mobility than those which make alternative choices for one or both of these features. Indeed, of the correlated disorder models, only those theories that incorporate small polaron rates come closest to simultaneously reproducing the field and temperature dependence of the measured mobility, while retaining a convincing Poole-Frenkel behavior. In the two uncorrelated models, only those which use polaron rates do a reasonable job of characterizing the experimental data over a sufficiently convincing range of electric fields and temperatures.

In conclusion, it is hoped that an analysis of existing data for this material, and others, at different concentrations, using the approach adopted in this dissertation, in which a direct comparison with experimental data is employed, will help to provide a convincing resolution to the apparent, but possibly artificial, puzzles that have recently appeared in the molecularly-doped polymer transport literature.

BIBLIOGRAPHY

[1] D. M. Pai. *J. Chem. Phys.*, 52:2285, 1970.

[2] W. D. Gill. *J. Appl. Phys.*, 43:2285, 1972.

[3] J. Hirsch. *J. Phys. C*, 12:321, 1979.

[4] H. Baessler, G. Schonherr, M. Abkwitz, and D. M. Pai. *Phys. Rev. B*, 26:3105, 1982.

[5] M. Stolka, J. F. Yanus, and D. M. Pai. *J. Phys. Chem.*, 88:4704, 1984.

[6] M. Abkowitz and M. Stolka. *Phil. Mag. Lett.*, 58:239, 1988.

[7] L. B. Schein, A. Peled, and D. Glatz. *J. Appl. Phys.*, 66:686, 1989.

[8] L. B. Schein. *Mol. Cryst. Liq. Cryst.*, 183:41, 1990.

[9] M. Abkowitz, H. Baessler, and M. Stolka. *Phil. Mag. B*, 63:201, 1991.

[10] P.E Parris, V.M. Kenkre, and D.H. Dunlap. *Phys. Rev. Lett.*, 87:126601, 2001.

[11] S.V. Novikov, D. H. Dunlap, V. M. Kenkre, P. E. Parris, and A. V. Vannikov. *Phys. Rev. Lett.*, 20:4472, 1998.

[12] P.E. Parris, D.H. Dunlap, and V.M. Kenkre. *Phys. Stat. Solidi. b*, 47:218, 2000.

[13] H. Baessler. *Phys. Stat. Sol. (b)*, 107:9, 1981.

[14] H. Baessler. *J. Mod. Phys. B*, 8:847, 1994.

[15] G. Pfister and H. Scher. *Adv. Phys.*, 27:747, 1978.

[16] D.H. Dunlap, V.M. Kenkre, and P.E. Parris. *J. Imaging Sci. Technol.*, 43:437, 1999.

[17] H. Baessler. *phys. stat. sol. (b)*, 175:15, 1993.

[18] D.H. Dunlap, P.E. Parris, and V.M. Kenkre. *Phys. Rev.Lett.*, 77:542, 1996.

[19] J. X. Mack, L.B. Schein, and A. Peled. Hole mobilities in hydrazone-polycarbonate dispersions. *Phys. Rev. B*, 39:7500, 1989.

[20] D.H. Dunlap, L.B. Schein, and A. Tyutnev. *J. Chem. Phys. C*, 114:9076, 2010.

[21] L.B.Schein. *Philos Mag. B*, 65:795, 1992.

[22] L.B. Schein and P.M. Borsenberger. *Chem. Phys.*, 177:773, 1993.

[23] P. M. Borsenberger and S. Weiss. *Organic Photoreceptors for Xerograph.* CRC Press, 1998.

[24] C.W. Tang. *Appl. Phys. Lett.*, 48:183, 1986.

[25] J.H. Burroughes, C.A. Jones, and R.H. Friend. *Nature*, 335:137, 1988.

[26] D. M. Pai. *J. Non-Cryst. Solids*, 59 & 60:1255, 1983.

[27] D. M. Pai and A. R. Melnyk. *Proc. SPIE*, 617:82, 1986.

[28] A. R. Melnyk and D. M. Pai. *Proc. SPIE*, 1253:141, 1990.

[29] M. Stolka and J. Mort. *Kirk-Othmer Encylopedia of Chemical Technology.* John Wiley and Sons, New York, 1994.

[30] D. M. Pai and B. E. Springett. *Rev. Mod. Phys.*, 65:163, 1993.

[31] K. Y. Law. *Chem. Rev.*, 93:449, 1993.

[32] D. M. Pai. *Frontiers of Polymer Research.* Plenum Press, New York, 1991.

[33] R. H. Jordan, L. J. Rothberg, A. Dodabalapur, and R. E. Slusher. *Appl. Phys. Lett.*, 280:1997, 1996.

[34] A. B. Walker, A. Kambili, and S. J. Martin. *J. Phys.: Condens. Matter*, 14:9825, 2000.

[35] D. P. West, M. D. Rahn, C. Im, and H. Baessler. *Chem. Phys. Lett.*, 326:407, 2000.

[36] J. Kalinowski, P. DiMarco, M. Cocchi, V. Fattori, N. Camaioni, and J. Duff. *Appl. Phys. Lett.*, 68:2317, 1996.

[37] J. Kido, G. Harada, and K. Nagai. *Chem. Lett.*, 44:161, 1996.

[38] C. Tanase, E. J Meijer, P. W. Blom, and D. M. de Leeuw. *Phys. Rev.Lett.*, 91:216601, 2003.

[39] J. H. Burroughes, C. A. Jones, and R. H Friend. *Nature*, 335:137, 1988.

[40] A. Tsumura, H. Koezuka, and T. Ando. *Synth. Met.*, 25:11, 1988.

[41] H. Inada, Y. Yonemoto, T. Wakimoto, K. Imai, and Y. Shirota. *Mol. Cryst. Liq. Cryst.*, 280:331, 1996.

[42] A. R. Brown, D. M. Deleeuw, E. J Lous, and E. E. Havinga. *Synth. Met.*, 66:257, 1994.

[43] Y. Y. Lin, D. J. Gundlach, S. F Nelson, and T. N. Jackson. *IEEE Trans. Electron Devices*, 44:1325, 1997.

[44] P. W. M Blom, V. D. Mihailetchi, L. J. A. Koster, and D. E. Markov. *Adv. Mater.*, 19:1551, 2007.

[45] E. Bundgaard and F. C. Krebs. *Solar Energy Materials & Solar Cells*, 91:954, 2007.

[46] M. Pope and C.E. Swenberg. *Electronic Processes in Organic Crystals and Polymers*. Oxford University Press,USA, 1999.

[47] Charles Kittel. *Introduction to Solid State Physics*. Wiley, 1953.

[48] J. Ziman. *Electrons and phonons: The theory of transport phenomena in solids*. Oxford University Press,USA, 1960.

[49] P. Drude. *Annalen der Physik*, 306:566, 1900.

[50] M. A. Lampert and P. Mark. *Current Injection in Solids*. Academic Press, New York, 1970.

[51] J.R. Haynes and W. Shockley. *Phys. Rev.*, 81:835, 1951.

[52] J. Frenkel. *Phys. Rev.*, 54:647, 1938.

[53] G. Pfister. *Phys. Rev. B*, 16:3676, 1977.

[54] V. Novikov and A.V. Vannikov. *J. Phys. Chem.*, 99:14573, 1995.

[55] Y. Gartstein and E. Conwell. *Chem. Phys. Lett.*, 245:351, 1995.

[56] A. Miller and E. Abrahams. *Phys. Rev.*, 120:745, 1960.

[57] N.G. VanKampen. *Stochastic Processes in Physics and Chemistry*. North Holland, 2007.

[58] N.E. Gruhn, D.A. da Silva, T.G. Bill, M. Malagoli, V. Coropceanu, A. Kahn, and J.L. Bredas. *J. Am. Chem. Soc.*, 124:7918, 2002.

[59] J. L. Bredas, D. Beljonne, V. Coropceanu, and J. Cornil. *Chem. Rev.*, 104:4971–5003, 2004.

[60] T. Holstein. *Ann. Phys. N.Y.*, 8:325,343, 1978.

[61] D. Emin. *Adv. Phys.*, 24:305, 1978.

[62] R. A. Marcus. *J. Chem. Phys.*, 24:966, 1956.

[63] S.V. Novikov and A.P. Tyutnev. *J. Chem. Phys.*, 138:104120, 2013.

[64] S.V. Novikov and A.V. Vannikov. *J. Chem. Phys. C*, 113:2532, 2009.

[65] B. Derrida. *J. Stat. Phys.*, 31:433, 1983.

[66] L.B. Schein and A. Tyutnev. *J. Chem. Phys. C*, 112:7295, 2008.

VITA

Amrita Roy Chowdhury was born near Kolkata, West Bengal, India. She did her schooling in Kolkata. She obtained her B-Tech(2006) and M-Tech(2008) degree in Applied Electronics & Instrumentation Engineering from West Bengal University of Technology, India.

Amrita started her studies towards a Ph.D. in Physics in 2008 at Missouri University of Science and Technology. In 2009, she joined the group of Dr. Paul E. Parris to work on her research project, which is focused on the transport properties of charge carriers in molecularly doped polymers. Results of this project are presented in this dissertation and will appear in a publication entitled *"Hopping Transport in 30% DEH:PC"* in the near future. She received her M.S. in Physics in December 2013 and Ph.D. in Physics in December 2015 from Missouri University of Science & Technology.